INVESTIGATION OF WETTED PARTICLE COLLISIONS THEORETICALLY AND EXPERIMENTALLY USING A PENDULUM APPARATUS

By

Carly Michelle Donahue

B.S., Berry College, 2006

A dissertation submitted to the

Faculty of the Graduate School of the

University of Colorado in partial fulfillment

of the requirement for the degree of

Doctor of Philosophy

Department of Physics

2011

This dissertation entitled:

Investigation Of Wetted
Particle Collisions Theoretically and
Experimentally Using A Pendulum Apparatus

Written by Carly Michelle Donahue

Has been approved for the Department of Physics

_____
Christine M. Hrenya

_____
Paul D. Beale

_____
Robert H. Davis

_____
Michael A. Dubson

_____
Matthew A. Glaser

September 2011

The final copy of this thesis has been examined by the signatories, and we find that both the content and the form meet acceptable presentation standards of scholarly work in the above mentioned discipline

Donahue, Carly Michelle (Ph.D., Physics)
Investigation of Wetted Particle Collisions Theoretically and Experimentally using a Pendulum Apparatus
Dissertation Directed by Professor Christine M. Hrenya

The addition of a small amount of liquid to a granular system can dramatically change the flow dynamics including the flowability, tensile strength, and segregation. Such liquid-coated particles coated are common in nature (e.g. avalanches, pollen capture) and in industry (e.g. granulation, particle filtration). Despite their ubiquity, predicting macro-scale (bulk) flows of liquid-coated particles is still elusive. A micro-scale (particle-level) investigation of the interactions of few wetted particles will lead to the identification of the dominant physical mechanisms which feeds into the understanding and modeling of bulk flows of wetted systems.

Previous micro-scale studies of wetted particles have included experimental and theoretical efforts to study particle-wall collisions (both oblique and head-on) and particle-particle collisions (head-on only). Before using such micro-scale models to describe macro-scale flows, more general cases need to be first considered such as collisions between more than two particles and the rotational motion of agglomerates. The goal of this work is to address these two issues through a combination of experiments using a pendulum apparatus and theory.

To investigate collisions between more than two particles, this work focuses on the normal (head-on) collision of three spheres. The foundation for such work is provided by first investigating analogous dry (non-wetted) systems. Experimental results are compared to soft-sphere models, which simultaneously account for all collisions, and a hard-sphere model, which treats the three-body collision as a series of two-body

collisions. While the soft-sphere models generally predicts the post-collisional velocities better, the hard-sphere model exhibits a good comparison overall.

In the wetted three-particle collisions, the pendulum apparatus is coined Stokes's cradle for the Stokes flow in the liquid gap between the particles. In two-body collisions, only two outcomes exist, namely stick and bounce. But in three-particle collisions, four possible geometrical outcomes exist and using the model as a guide, all four outcomes are experimentally observed. Furthermore, this combination of experiments and theory led to the identification of the dominant physical mechanisms. First, due to the large pressures in the liquid gap, the fluid may undergo a glass transition at which point the particles reverse direction. Additionally, previous theories neglect the viscous resistance of the fluid as the particles move away from one another, since cavitation was assumed to occur. However, three-body experiments show definitively that the outbound resistance cannot be neglected.

To investigate how rotational motion influences agglomeration, oblique collisions between two particles are performed. Whereas in normal collisions particles rebound only due to solid deformation, so-called centrifugal forces in oblique collisions produce a new outcome in which the particles initially form a rotating agglomerate, and then de-agglomerate at a later time. Furthermore, capillary forces play an essential role in oblique collisions even when the capillary number (viscous over capillary forces) is high. This recognition leads to the introduction of a dimensionless number, the centrifugal number (centrifugal over capillary forces), which together with the previously established Stokes number characterizes the regime map of outcomes for two-particle collisions.

DEDICATION

To My Mom and Dad

Acknowledgements

My years in graduate school would not have been possible without the support and encouragement of remarkable people. I have been very fortunate to be part of a wonderful research group. I would like to thank Christine Hrenya, for her trust, patience, and dedication. Not only is Christine a wonderful advisor, but she and her husband have also provided me with many great conversations and many great meals. I owe a great deal of gratitude to the undergraduate students that worked with me in the lab including Ken Nakagawa, Alia Zelinskaya, and Will Brewer. I just hope that they learned as much from me as I did working with them. Gustavo Joseph continues to be an invaluable resource, as well as a source of hours of entertaining stories. The office would have been lonely without Jia-wei Chew, with whom I had many discussions on just about everything. I would also like to thank our collaborator, Rob Davis, my physics advisor, Paul Beale, and the rest of my dissertation committee for their ongoing support and fruitful discussions.

I have been fortunate to have great friends outside the lab including Allison Churnside, Adam Light, Erinn Looney-Triggs, Nora Matell, Sharon Olsen, Leigh Palmer, Evan Salim, Michelle Stallions, and Matt Swallows. I was fortunate to meet Brenda Remy at the beginning of my career, as she has been a great listener and a great friend. Stephanie Malone and I had a wonderful time running APP, and I could not ask for someone better to work with on that endeavor.

My decision to go to graduate school would have never happened without the encouragement of a few key people. I would like to thank fellow classmate Frank Petruzielo. I had a number of great professors at Berry College who took a personal

interest in my education including Martin Cipollini, Eric McDowell, Ron Taylor, Todd Timberlake, Charles Lane, and Paul Wallace. I cannot describe how fortunate I was to have the opportunity to work with Philip Metzger at Kennedy Space Center. His energy and curiosity is contagious, and I would not be where I am without him. I will also never forget Bob Youngquist and the rest of the Physics Lab at KSC.

Finally, I have the best family in the world. I am happy to now call Michael Martin my husband and welcome him into my family, and I am fortunate that he has such a great family welcoming me. In addition to my husband being patient, kind, and loving, he is always giving me confidence in my work. My family members are not only creative and fun, but also incredibly loving and generous. I would like to thank my B'baum and B'daddy for always being my cheerleaders. My sister, Janna, has always made me feel that my life was an unwritten book and I could do whatever I wanted. Finally, I would like to thank my parents. Again and again, my parents have shown that they would do anything for me and hopefully one day I can do the same for them.

Table of Contents

List of Tables

List of Figures

1. INTRODUCTION

1.1. Motivation

In our daily lives, we come into contact with granular materials frequently. Beans for the morning cup of coffee, snow, and even pollutants in the air are granular in form. Furthermore, particulates are widespread throughout industry including foodstuffs [1], pharmaceuticals [2], mining [3], and construction [4]. They make up approximately one-half of all products and nearly three-quarters of the raw materials in the U.S. [5]. In nature, granular materials are found in many sizes (10^{-6} m – 10^{5} m) and many locations (e.g., beach, mountaintops, space), and are composed of a variety of materials (e.g., ice, soil).

Although granular materials are common, a poor predictive understanding has led to significant practical challenges. Landslides and other forms of ground failure (e.g. liquefaction) are the most expensive natural hazard [6]. In industry, uniform mixing is difficult to achieve, since particulates segregate based on parameters such as size and density, and the current theoretical understanding of the mixing process is not sufficient for equipment design [7, 8]. Scaling-up processes continues to be an ongoing challenge, and consequently many factories operate significantly under desired efficiency levels [9]. In the pharmaceutical industry, the lack of fundamental understanding of granular materials leads to empirical designs of equipment and product as well as an incentive not

to change, which leads to further delays of patient treatment [10]. Furthermore, the inability to model granular materials leads to challenges when designing equipment for use on the moon, where an empirical approach is not sufficient [11]. Granular materials remain difficult to describe using a fundamental, continuum approach because the interactions between particles are dissipative in nature (unlike the molecular counterparts), and there exists a lack of separation of scales between grain sizes and flow size [12].

To add to the already complex nature of granular materials (e.g., friction, inelasticity, polydispersity), particles experience cohesion when an attractive force exists between the particles. Cohesion may arise due to a variety of sources including electrostatic forces, van der Waals forces, magnetic forces, and liquid bridges. Even a small amount of cohesion between particles can cause large changes on the properties of the bulk material. Cohesion can affect flowability [13, 14], angle of repose of a granular heap [15-17], and the tensile strength [18, 19]. Under the right circumstances, adding cohesion during mixing can enhance or mitigate species segregation [20, 21]. Furthermore, the packing fraction of cohesive grains decreases with the magnitude of the cohesive force [22, 23].

Of the sources of cohesion listed above, the focus of this work is on liquid bridges. Particles are referred to as 'wetted' when a thin layer of liquid covers the particles either completely or partially, as opposed to immersed (or suspended) particles, so that a liquid bridge between two particles may form. Figure 1.1 shows a schematic of an immersed particle, a fully-coated wetted particle, and two particles partially covered with liquid connected by a liquid bridge. Such wetted particles are found throughout nature in sand castles, pollen, landslides, avalanches, and interstellar dust among others. In industry,

wetted particles are relevant to particle filtration, coagulation, agglomeration, slurry transport, spray coating, drying, and pneumatic transport. Wet granulation, a process of creating agglomerates, is widely used in chemical and pharmaceutical industries for more control over uniformity, density, compatibility as well as increased flowability [24].

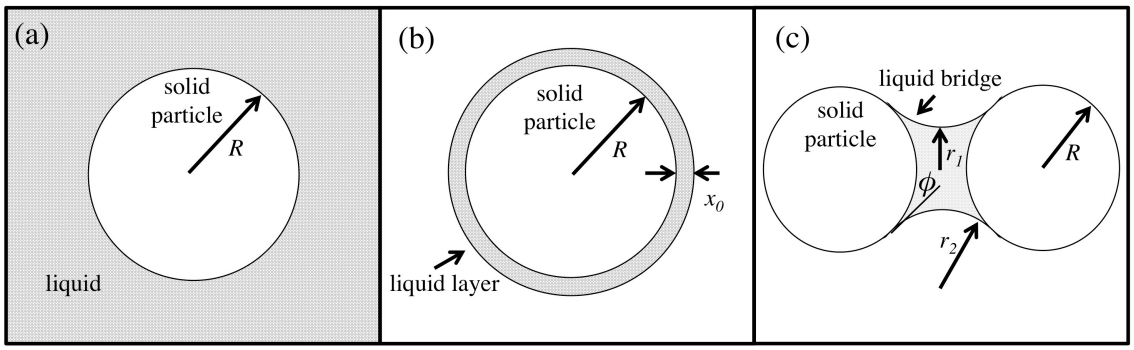

Figure 1.1 Schematic of (a) an immersed particle, (b) a wetted particle, and (c) two particles connected by a liquid bridge.

1.2. Forces Relevant to the Interaction of Wetted Particulates

When two wetted particles interact, the forces acting on each particle can be characterized as either static or dynamic. The static forces include capillary forces, while the dynamic forces include lubrication and solid mechanical forces. The determine the relative influence of viscous to capillary forces, the capillary number for wetted particles is

$$Ca = 3a\mu v_n/\sigma x_0 . \tag{1.1}$$

Here, $a = R_1R_2/(R_1+R_2)$ is the reduced radius where R is the radius of two spherical particles, μ is the liquid viscosity, v_n is the normal component of the relative velocity between the spheres, x_0 is the oil thickness, and σ is the surface tension. For small

capillary numbers (Ca < 0.01) capillary forces dominate, whereas at large capillary numbers (Ca > 100) viscous forces dominate [25].

1.2.1. Static Forces arising from Liquid Bridge

The (static) capillary force is composed of three contributions: (i) the buoyancy force due to the partial immersion of each particle, (ii) the force due to the reduced hydrostatic pressure in the bridge, and (iii) the axial component of the surface tension at the liquid-gas interface. However, for particles less than 1 mm, buoyancy can be neglected as well as the influence gravity has on the shape of the liquid bridge [26, 27]. The surface tension force acts on the interface between the liquid and gas phases and depends on the wetting angle, φ, the angle between the surface of the liquid and the solid at the contact point (Figure 1.1c). The contribution to the capillary force due to the surface tension pulls the particles together and is given by

$$F_{st} = 2\pi r_1 \sigma \tag{1.2}$$

where r_1 is the radius of the circular neck cross-section (Figure 1.1c). Typically, the force is calculated at the solid-liquid-gas contact line; however, it can also be calculated at any plane away from this line. For the case of perfectly wetted spheres, $\varphi = 0$, the curvature of the bridge is not sensitive to the solid-liquid-gas contact line [28]. Therefore, the surface tension between two particles connected only by a liquid bridge with $\varphi = 0$, (Figure 1.1c) is approximately the same as for two fully coated spheres in contact. The hydrostatic pressure forces that arise from the pressure deficiency in the liquid bridge can pull together or push apart the particles depending on the values of the principle radii, r_1 and r_2, and is given by

$$F_{hp} = -\pi r_1^2 \Delta P \tag{1.3}$$

where ΔP is the reduced hydrostatic pressure. This equation requires the solution of Laplace-Young equation

$$\Delta P = \sigma (1/r_1 + 1/r_2) \tag{1.4}$$

where r_2 is the principle radius of curvature (Figure 1.1c). Neglecting buoyancy, Fisher [29] and Adams and Perchard [30] have solved analytically for the capillary force (F_{st} + F_{hp}) between two spheres assuming that the principle radii of curvature are constant. Such derivations have been shown to agree well with experimental measurements within 10% [29-31]. Additionally, the Laplace-Young equation has also been solved numerically to express the capillary force (F_{st} + F_{hp}) as a function of the bridge volume and separation distance instead of the principle radii [32].

As the particles separate, when they reach a critical distance the liquid bridge connecting the particles ruptures. Lian *et al.* [31] proposed the following empirical relationship for the rupture distance between two spheres

$$x_{rd} = (1+0.5\varphi)V^{1/3} \tag{1.5}$$

Previous experimental results of Mason and Clark [33] agree well with this equation. More recent experiments of the rupture distance by Fairbrother and Simons [34] who used 50 μm-diameter spheres were within 10% of the distances predicted from this equation.

1.2.2. Dynamic Forces arising from Liquid Bridge

Whereas capillary forces cause cohesion by pulling the two particles together, (dynamic) viscous forces cause 'cohesion' by a loss of the energy associated with particle motion to the fluid (i.e. viscous losses). To determine if the fluid in the gap between the particles is laminar, the Reynolds number (ratio of fluid inertia to the viscous force), *Re*, is evaluated. For two wetted particles

$$Re = \rho v_n x_0 / \mu \tag{1.6}$$

where ρ is the liquid density. In this work, viscous forces dominate, so the focus is on low *Re* (Stokes) flow.

Before considering the viscous forces on wetted particles (which will be discussed in later chapters), it is helpful to first introduce the low-*Re* solution for an *immersed* particle. Specifically, the viscous force on a sphere immersed in a liquid and approaching a wall or approaching another sphere is

$$F_{L,n} = -\frac{6\pi\mu a^2 v_n}{x}, \tag{1.7}$$

where x is the separation distance of the surfaces [35, 36]. This expression is only valid for $x << a$. As the gap closes and x approaches zero, the lubrication force diverges for nonzero relative velocity. If the particles are assumed to be smooth and rigid, and moving due to inertial and not an applied force, they stop at a finite distance away and do not rebound. Therefore, another physical mechanism, namely the deformation of the solid (as described in Section 1.2.3), needs to be considered for two particles to rebound.

In addition to the normal force experienced by a particle, as a particle moves tangentially to a wall or another particle, the shear stress of the fluid produces a tangential force on the particle. An expression for the tangential force of such an *immersed* particle

sliding without rotating in close proximity ($x << a$) to another particle of the same radius was derived by O'Neill and Majumdar [37] using an asymptotic solution to the equations governing Stokes flow :

$$F_{L,t} = -6\pi\mu a^2 v_t \left(\frac{1}{3} \ln \frac{2a}{x} + 1.2720 \right), \tag{1.8}$$

where v_t is the relative tangential velocity of the centers of the two spheres. For two equal-sized particles without translational motion, but rotating in close contact with the same angular velocity about their centers relative to the fluid, Ω, O'Neill and Majumdar [37] found the tangential force to be

$$F_{L,t} = 6\pi\mu a^2 \Omega \left(\frac{1}{3} \ln \frac{2a}{x} - 0.1583 \right). \tag{1.9}$$

1.2.3. Solid Deformation

As two bodies separated by a liquid gap approach each other, the pressure builds to squeeze the fluid out from between them, which may cause the solid body to deform. Including the effects of this deformation of the particles is important, since otherwise, the two (smooth) particles in Stokes flow would stop at a finite distance and not rebound. A coupling of solid mechanical (elastic) forces and hydrodynamic forces (i.e., elastohydrodynamics) predicts that, for large enough pressures, the energy of deformation is great enough to cause velocity reversal upon its release and transformation to kinetic energy of the particle. Among the earliest research efforts into solid mechanics of dry materials was that of Hertz [38], over a century ago, whose objective was to understand the optical properties of stacked lenses. The theory included non-rigid (deformable)

particles that were both frictionless and perfect elasticity. For perfectly elastic particles engaged in a head-on collision, the coefficient of restitution, namely the ratio of the magnitudes of relative post-collision velocity to the pre-collision velocity, is unity. Following Hertz's work, advances have been made to describe additional complexities of such dry collisions between particles, including their inelasticity. While the coefficient of restitution is often assumed constant for a given material, experimental studies have shown it also to decrease with increasing impact velocity [39]. Recently though, careful measurements have found a non-monotonic behavior of the coefficient of restitution [40], which is attributed to the timescales of the vibrations of the solids being comparable to the collision time.

1.2.4. Pressure-Dependent Viscosity

Oftentimes the viscosity of the liquid is assumed constant, but viscosity depends on the particular conditions. Stokes was the first to consider that the viscosity of a fluid not only depends on temperature, but also on pressure [41]. While the effect of temperature on viscosity is relatively well understood, pressure dependence of viscosity is not, particularly at high pressures. For fixed ambient temperature, the dependence of pressure and viscosity on pressure is given by the Barus law [42]

$$\mu = \mu_0 \exp(Cp), \tag{1.10}$$

where p is the pressure, μ_0 is the viscosity at atmospheric pressure, and C is the pressure-viscosity coefficient, a constant that depends on the liquid. However, this equation underpredicts the viscosity above pressures of 0.5 GPa and additionally it does not predict well the shear stress. A variety of other models have been proposed and are more

appropriate under particular conditions (e.g., high or low pressure, thin or thick film) [42-44]. A short review of the effect of pressure on viscosity and a list of values of C for various lubricants can be found in Gohar [45].

If the pressure is large enough, the liquid may undergo a glass transition, so that it exhibits rigidity similar to an amorphous or glassy solid. While the glass transition depends both on temperature and pressure, Alsaad *et al.* [46] found that under certain conditions at high pressures, the glass transition could be achieved at rather normal temperatures. Furthermore, at the glass transition, the viscous properties of the liquid become elastic so that it behaves in a viscoelastic manner [45].

For the experimental systems under consideration in this work, a consideration of pressure-dependent viscosity is appropriate since the pressure in the liquid gap between particles increases considerably during approach. Indeed, a glass transition may occur, so that the particles rebound.

1.2.5. Cavitation

Just as the large pressures affect the fluid upon approach, as the particles move away from each other, the pressure drops significantly, and becomes smaller than the ambient pressure so that fluid is sucked into the gap between the receding surfaces, which may lead to the formation of cavitation bubbles. Cavitation is typically assumed to occur when the pressure of the fluid drops below a threshold pressure, often the vapor pressure [47, 48]. However, this criterion poses two issues. First, vapor pressure is defined as the equilibrium pressure of the vapor of the liquid at a given temperature in contact with an existing free surface, whereas a cavitation bubble is formed by the rupture of a

homogenous liquid. The stress required for liquid to rupture is measured by the tensile strength of the liquid, not vapor pressure [49]. Second, for the onset of cavitation based on tensile strength rather than vapor pressure, the liquid will cavitate when any one of the three principal stresses exceeds the tensile strength of the liquid, whereas pressure is a measure of the average of the principal stresses. Recently, Joseph [50] developed a rigorous criterion for the inception of cavitation using the tensile strength. Experimental studies of cavitation in the fluid between a particle approaching a wall have confirmed the relationship between the maximum stress in the liquid and the size of the cavitation structures formed [51].

1.3. Previous Work on Wetted Particle Systems

1.3.1. Two-Body Studies (Micro-level)

The foundation of the description for wetted-particle collisions traces to earlier work on *immersed* collisions between two particles. The Stokes number,

$$St = \frac{mv_0}{6\pi\mu a^2}, \tag{1.11}$$

which is a measure of the inertia of colliding particles relative to the viscous force of the surrounding liquid, is the relevant dimensionless number. Here, $m = m_1m_2/(m_1 + m_2)$ is the reduced mass, and v_0 is the impact speed. As mentioned above, low-Reynolds-number (lubrication) theory has established that two smooth, *rigid* particles approaching one another will never touch or rebound, but instead stop at a finite distance as they approach (Equation 1.7). The deformation associated with *non-rigid* particles approaching each other in an immersed in a fluid was first considered by Davis *et al.*

[52]. In their work, a theory was developed which couples the fluid hydrodynamics and the particle (elastic) deformation during the collision; this theory is known as elastohydrodynamics. By allowing for a non-rigid particle, kinetic energy is stored in the deformation and, when it is released, rebound of the particle may be achieved if the stored energy is great enough to overcome the viscous resistance (i.e., if St is large enough). Additionally, the theory indicates that as the viscosity of the fluid increases, the critical Stokes number, St^*, decreases, where St^* is the Stokes number at which there is a transition from no rebound to rebound. Experimental collisions performed by measuring the velocity of a particle immersed in liquid as it bounced off a wall confirm the described theoretical trends [41]. Later work by Barnocky and Davis [53] includes a pressure-dependent viscosity proposed by Chu and Cameron [42] for immersed particles. Barnocky and Davis [53] conclude that, while the inclusion of pressure-dependent viscosity lowers the St^*, it plays a weak role in the outcomes of the collision in their parameter space.

Numerous investigations have also been performed for *wetted* two-body collisions, expanding on the aforementioned works on immersed collisions. Some of the earlier experimental works that consider wetted-particle collisions include Barnocky and Davis [54] and Lundberg and Shen [55], who performed two-body collisions by dropping a dry particle onto a liquid-coated surface. Both works confirm the trend predicted by elastohydrodynamics for immersed collisions, namely a decreasing St^* with increasing viscosity. Using a different approach, Pitois *et al.* [56] measured total force due to lubrication and capillary forces between two spheres as a function of separation distance and relative velocity. Additionally, a number of theories have been developed to predict

agglomeration/de-agglomeration behavior. Ennis *et al.* [57] modeled a two-particle wetted collision without employing elastohydrodynamics but instead by assuming rebound occurred when the two particles reached a finite separation distance. Lian *et al.* [58] presented a slightly simplified model of wetted collisions between two particles based on elastohydrodynamics that agrees well with the theory of Davis *et al.* [52]. In the effort by Davis, Rager, and Good [59], a scaling argument was used to apply the elastohydrodynamic theory developed by Davis *et al.* [52] to two-particle wetted collisions, and they found good agreement with their experiments. Further work by Kantak and Davis [60] presented a complete elastohydrodynamic coupling to describe wetted collisions between two particles; while experiments agreed well with theoretical predictions, the model assumed perfectly elastic spheres even though the nylon particles used in the experiments had a coefficient of restitution approximately equal to 0.7.

1.3.2. Many-Particle Studies (Macro-level)

The bulk behavior of systems containing many wetted particles has been the focus of a number of experimental investigations [15, 61, 62]. A rotating drum has proven to be particularly useful in wetted flow since it can generate continuous grain flow [63-65]. Under the correct circumstances, Li and McCarthy [66] found adding liquid to a granular system increased species segregation in a rotating drum. On the other hand, a small amount of liquid has been found to mitigate segregation between unlike particles poured from a silo [67]. Experimental studies of wetted particles in fluidized beds have attempted to determine the dependence of granule growth rate on material properties such as particle size [68, 69].

To investigate many-particle flows, many researchers have employed discrete element models (DEM), which incorporates microscopic (particle-level) descriptions of the inter-particle forces. A square-well potential used to model general cohesion has proven to be an effective tool in hard-sphere simulations [70]. Since most DEM simulations have focused on fairly dense systems, however, soft-sphere models are routinely used, which contain simplified force laws to model the enduring collisions between particles. In the soft-sphere model treatment, collisions between more than two particles are accounted for simultaneously; however, the computational costs of such modeling is relatively high, which significantly limits the total number of particles that can be simulated. Such soft-sphere models include cohesion due to liquid bridges by using simplified capillary and viscous forces, which typically account only for the normal forces between two particles. The soft-sphere modes have been used to study the collisions of large agglomerates of wetted particles (> 100 particles) [71-73]. Soft-sphere models have also been useful to simulate specific systems such as rotating drums, fluidized beds, and cohesive soil [20, 74, 75]. While many simulations have assumed that each particle is evenly coated, some work has been done on the liquid transfer between colliding particles [76]. On the other hand, in dilute flows collisions have been assumed to be primarily binary, so hard-sphere models have been used, which treat collisions as instantaneous and binary. Such treatment is limited to only the initial phase of agglomeration since hard-sphere models do not describe collisions between more than two particles [77].

While modeling individual grains via DEM is a useful tool for studying bulk behavior of wetted particles, the large computational costs limit the total number of

particles that can be simulated. Even in a laboratory-scale fluidized bed, the number of particles easily exceeds a billion. Therefore, developing a continuum framework is particularly appealing for modeling the large number of particles in industrial and natural settings. Such a continuum framework for describing wetted-particle agglomeration and de-agglomeration takes the form of population balance, which is a rate equation that tracks the change in number of agglomerates of a given size. Hulbert and Katz [78] and Randolph and Larsen [79] introduced the population balance for general particulate systems. Within the population balance description is the coalescence kernel. The coalescence kernel describes the collision frequency and probability of success of agglomeration. Most coalescence kernels that describe wetted-particulate systems have fitted parameters with little physical foundation. Therefore, these kernels are unable to make predictions of the effect of scale-up or changes in the formulation properties [80]. While a number of physical models exist that predict agglomeration versus de-agglomeration of wetted-particle collisions, few have been used to develop a coalescence kernel. One exception to the empirical kernels mentioned above is a physically-based kernel proposed by Liu and Litster [81], which predicts particle coalescence based upon the Stokes number. In addition to the already challenging task of developing a coalescence kernel based on physical agglomeration models, current agglomeration models are based upon two-body collisions, whereas in bulk flows, collisions of more than two bodies regularly occur [82].

1.4. Dissertation Objectives

The focus of this work is to broaden the particle-level research, which provides more insight into the physical mechanisms dictating the dynamics of wetted particles and provides a foundation for simulations wetted particles. While significant research has been performed to study of collisions between two wetted particles, a majority of the experimental and theoretical focus has been between collisions of a particle and a wall.

1.4.1. Normal Collisions between Three Dry Spheres (Chapter 2)

While the focus of this work is on wetted particles, a complete understanding of the corresponding dry collisions is first necessary. Though soft-sphere models are routinely used in DEM simulations of dry granular material, no previous comparison exists between soft-sphere models and collisions between more than two particles. The lack of comparison of soft-sphere models is particularly surprising given that a major advantage of such models is their applicability to collisions involving more than two particles. Therefore, in this chapter the objectives are to

(a) observe what geometrical outcomes (e.g. fully separated, fully agglomerated) exist in three-particle collisions;

(b) evaluate various soft-sphere models to determine their applicability in predicting such collisions; and

(c) evaluate the ability of a hard-sphere model to predict geometrical outcomes and post-collisional velocities of three-particle collisions by modeling the collision as a series of two-body collisions.

1.4.2. Normal (Head-on) Collisions Between Three Wetted Spheres (Chapters 3 – 4)

In wet collisions between two particles, only two outcomes are observed, namely stick and de-agglomerate. However, in a three-particle collision, four geometrical outcomes are possible. The objectives of the work in Chapter 3 are to:

(a) experimentally determine via a 'Stokes cradle' pendulum apparatus whether all four geometrical outcomes are possible in a three-body wetted collision over a considerable parameter space;

(b) identify how changes of experimental parameters influence the observed outcomes; and

(c) identify the predominant physical mechanisms in a three-particle collision.

1.4.3. Oblique Collisions between Two Wetted Particles (Chapters 5 – 6)

Previous experiments of oblique collisions are limited to collisions between a particle and a wall and so, there was no rotation of the agglomerate. The pendulum apparatus described in Chapters 2 – 4 is modified to conduct oblique collisions between two particles. Accordingly, the objectives of these Chapters are to:

(a) identify the predominant physical mechanism in a two-particle oblique collision, particularly how rotation of the agglomerate affects the agglomeration/de-agglomeration of a doublet.

(b) identify how changes of the experimental parameters influence the wet coefficient of restitution and the angle of doublet rotation.

Literature Cited

1. Law, C.L. and A.S. Mujumdar. Drying: Biological Materials. *Encyclopedia of Industrial Biotechnology: Bioprocess, Bioseparation, and Cell Technology*.
2. Prescott, J.K. Powder Handling. *Pharmaceutical Process Scale-Up* **118**, 133, (2001).
3. Wills, B., *Mineral Processing Technology* 1979, Pergamon Press, lnc: New York City.
4. Bonneau, O., C. Vernet, M. Moranville, and P.C. Aitcin. Characterization of the granular packing and percolation threshold of reactive powder concrete. *Cement and concrete research* **30**, 1861-1867, (2000).
5. Nedderman, R.M. Statics and kinematics of granular materials. (Cambridge Univ Pr, 1992).
6. Fleming, R.W., F.A. Taylor, and G. Survey, *Estimating the costs of landslide damage in the United States*. 1980, US Dept. of the Interior, Geological Survey.
7. Ottino, J. and D. Khakhar. Mixing and segregation of granular materials. *Annual review of fluid mechanics* **32**, 55-91, (2000).
8. Bridgwater, J. Mixing of particles and powders: Where next? *Particuology*, (2010).
9. Matsen, J.M. Scale-up of fluidized bed processes: Principle and practice. *Powder Technology* **88**, 237-244, (1996).
10. Muzzio, F.J., T. Shinbrot, and B.J. Glasser. Powder technology in the pharmaceutical industry: the need to catch up fast. *Powder Technology* **124**, 1-7, (2002).
11. Gamsky, J.N. and P.T. Metzger. *The Physical State of Lunar Soil in the Permanently Shadowed Craters of the Moon*. 2010: ASCE.
12. Goldhirsch, I. Rapid granular flows. *Annual review of fluid mechanics* **35**, 267-293, (2003).
13. Weber, M.W., D.K. Hoffman, and C.M. Hrenya. Discrete-particle simulations of cohesive granular flow using a square-well potential. *Granular Matter* **6**, 239-254, (2004).
14. Tomas, J. Fundamentals of cohesive powder consolidation and flow. *Granular Matter* **6**, 75-86, (2004).
15. Nowak, S., A. Samadani, and A. Kudrolli. Maximum angle of stability of a wet granular pile. *Nature Physics* **1**, 50-52, (2005).
16. Forsyth, A., S. Hutton, M. Rhodes, and C. Osborne. Effect of applied interparticle force on the static and dynamic angles of repose of spherical granular material. *Physical Review E* **63**, 31302, (2001).
17. Pont, S., P. Gondret, B. Perrin, and M. Rabaud. Wall effects on granular heap stability. *EPL (Europhysics Letters)* **61**, 492, (2003).
18. Pierrat, P. and H.S. Caram. Tensile strength of wet granula materials. *Powder Technology* **91**, 83-93, (1997).
19. Valverde, J.M., A. Ramos, A. Castellanos, and P. Keith Watson. The tensile strength of cohesive powders and its relationship to consolidation, free volume and cohesivity. *Powder Technology* **97**, 237-245, (1998).

20. McCarthy, J.J. Micro-modeling of cohesive mixing processes. *Powder Technology* **138**, 63-67, (2003).
21. Hutton, S., A. Forsyth, M. Rhodes, and C. Osborne. Effect of interparticle force on mixing and segregation of dry granular materials. *Physical Review E* **70**, 31301, (2004).
22. Forsyth, A., S. Hutton, C. Osborne, and M. Rhodes. Effects of interparticle force on the packing of spherical granular material. *Physical Review Letters* **87**, 244301, (2001).
23. Dong, K., R. Yang, R. Zou, and A. Yu. Role of interparticle forces in the formation of random loose packing. *Physical Review Letters* **96**, 145505, (2006).
24. Faure, A., P. York, and R. Rowe. Process control and scale-up of pharmaceutical wet granulation processes: a review. *European Journal of Pharmaceutics and Biopharmaceutics* **52**, 269-277, (2001).
25. Salcudean, M., P. Darabi, K. Pougatch, and D. Grecov. A novel coalescence model for binary collision of identical wet particles. *Chemical Engineering Science* **64**, 1868-1876, (2009).
26. Princen, H.M. Comments on Effect of Capillary Liquid on Force of Adhesion between Spherical Solid Particles. *Journal of colloid and interface science* **26**, 249-&, (1968).
27. Cross, N.L. and R.G. Picknett. Comment on Paper Effect of Capillary Liquid on Force of Adhesion between Spherical Solid Particles. *Journal of colloid and interface science* **26**, 247-&, (1968).
28. Willett, C.D., M.J. Adams, S.A. Johnson, and J.P.K. Seville. Capillary bridges between two spherical bodies. *Langmuir* **16**, 9396-9405, (2000).
29. Fisher, R.A. On the capillary forces in an ideal soil; Correction of formulae given by W. B. Haines. *Journal of Agricultural Science* **16**, 492-505, (1926).
30. Adams, M. and V. Perchard. The Cohesive Forces Between Particles with Interstitial Liquid. *Proceedings of Powder Technology*, 147, (1985).
31. Lian, G.P., C. Thornton, and M.J. Adams. A Theoretical-Study of the Liquid Bridge Forces between 2 Rigid Spherical Bodies. *Journal of colloid and interface science* **161**, 138-147, (1993).
32. Mikami, T., H. Kamiya, and M. Horio. Numerical simulation of cohesive powder behavior in a fluidized bed. *Chemical Engineering Science* **53**, 1927-1940, (1998).
33. Mason, G. and W.C. Clark. Liquid Bridges between Spheres. *Chemical Engineering Science* **20**, 859, (1965).
34. Fairbrother, R.J. and S.J.R. Simons. Modelling of Binder Induced Agglomeration. *Particle & Particle Systems Characterization* **15**, 16-20, (1998).
35. Cameron, A., *Basic lubrication theory*. 1981, Ellis Horwood, Chichester.
36. Adams, M., B. Briscoe, and L. Pope. Tribology in Particulate Technology. *Adam Hilger*, (1987).
37. O'Neill, M.E. and R. Majumdar. Asymmetrical slow viscous fluid motions caused by the translation or rotation of two spheres. Part I: The determination of exact solutions for any values of the ratio of radii and separation parameters. *Zeitschrift für Angewandte Mathematik und Physik (ZAMP)* **21**, 164-179, (1970).
38. Hertz, H. Ueber die Ber¸hrung fester elastischer Kˆrper. *Journal f¸r die reine und angewandte Mathematik (Crelle's Journal)* **1882**, 156-171, (1882).

39. Goldsmith, W. Impact: the theory and physical behaviour of colliding solids. (Dover Pubns, 2001).
40. King, H., R. White, I. Maxwell, and N. Menon. Inelastic impact of a sphere on a massive plane: Nonmonotonic velocity-dependence of the restitution coefficient. *EPL (Europhysics Letters)* **93**, 14002, (2011).
41. Stokes, G. On the theory of internal friction of fluids in motion, etc. *Cambridge Trans* **8**, 287-305, (1845).
42. Chu, P. and A. Cameron. Pressure viscosity characteristics of lubricating oils. *J. Inst. Petrol* **48**, 147, (1962).
43. Roelands, C.J.A. Correlational aspects of the viscosity-temperature-pressure relationship of lubricating oils. *Druk. VRB, Groningen, Netherland s*, (1966).
44. Allen, C., D. Townsend, and E. Zaretsky. Elastohydrodynamic lubrication of a spinning ball in a nonconforming groove. *J. Lubr. Tech* **92**, 89-96, (1970).
45. Gohar, R. Elastohydrodynamics. (World Scientific Publishing Company, 2001).
46. Alsaad, M., S. Bair, D. Sanborn, and W. Winer. *Glass transitions in lubricants-Its relation to elastohydrodynamic lubrication/EHD*. 1977.
47. Bull, T. The tensile strengths of viscous liquids under dynamic loading. *British Journal of Applied Physics* **7**, 416, (1956).
48. Chang, H.-C. and L.-H. Chen. Growth of a gas bubble in a viscous fluid. *Physics of Fluids* **29**, 3530-3536, (1986).
49. Knapp, R., J. Daily, and F. Hammitt, *Cavitation, 1970*, McGraw-Hill, New York.
50. Joseph, D.D. Cavitation and the state of stress in a flowing liquid. *Journal of Fluid Mechanics* **366**, 367-378, (1998).
51. Marston, J., W. Yong, W. Ng, R.B.H. Tan, and S. Thoroddsen. Cavitation structures formed during the rebound of a sphere from a wetted surface. *Experiments in Fluids*, 1-18, (2010).
52. Davis, R.H., J.M. Serayssol, and E.J. Hinch. The Elastohydrodynamic Collision of 2 Spheres. *Journal of Fluid Mechanics* **163**, 479-497, (1986).
53. Barnocky, G. and R.H. Davis. The Influence of Pressure-Dependent Density and Viscosity on the Elastohydrodynamic Collision and Rebound of 2 Spheres. *Journal of Fluid Mechanics* **209**, 501-519, (1989).
54. Barnocky, G. and R.H. Davis. Elastohydrodynamic Collision and Rebound of Spheres - Experimental-Verification. *Physics of Fluids* **31**, 1324-1329, (1988).
55. Lundberg, J. and H.H. Shen. Collisional Restitution Dependence on Viscosity. *Journal of Engineering Mechanics-Asce* **118**, 979-989, (1992).
56. Pitois, O., P. Moucheront, and X. Chateau. Liquid bridge between two moving spheres: An experimental study of viscosity effects. *Journal of colloid and interface science* **231**, 26-31, (2000).
57. Ennis, B.J., G. Tardos, and R. Pfeffer. A Microlevel-Based Characterization of Granulation Phenomena. *Powder Technology* **65**, 257-272, (1991).
58. Lian, G., M.J. Adams, and C. Thornton. Elastohydrodynamic collisions of solid spheres. *Journal of Fluid Mechanics* **311**, 141-152, (1996).
59. Davis, R.H., D.A. Rager, and B.T. Good. Elastohydrodynamic rebound of spheres from coated surfaces. *Journal of Fluid Mechanics* **468**, 107-119, (2002).
60. Kantak, A.A. and R.H. Davis. Elastohydrodynamic theory for wet oblique collisions. *Powder Technology* **168**, 42-52, (2006).

61. Li, H.M. and J.J. McCarthy. Phase diagrams for cohesive particle mixing and segregation. *Physical Review E* **71**, 21305, (2005).
62. Liu, P.Y., R.Y. Yang, and A.B. Yu. Dynamics of wet particles in rotating drums: Effect of liquid surface tension. *Physics of Fluids* **23**, 13304-9, (2011).
63. Mills, P., J. Seville, P. Knight, and M. Adams. The effect of binder viscosity on particle agglomeration in a low shear mixer/agglomerator. *Powder Technology* **113**, 140-147, (2000).
64. Xu, Q., A.V. Orpe, and A. Kudrolli. Lubrication effects on the flow of wet granular materials. *Physical Review E* **76**, 31302, (2007).
65. Tegzes, P., T. Vicsek, and P. Schiffer. Development of correlations in the dynamics of wet granular avalanches. *Physical Review E* **67**, 51303, (2003).
66. Li, H.M. and J.J. McCarthy. Cohesive particle mixing and segregation under shear. *Powder Technology* **164**, 58-64, (2006).
67. Samadani, A. and A. Kudrolli. Segregation transitions in wet granular matter. *Physical Review Letters* **85**, 5102-5105, (2000).
68. Rajniak, P., F. Stepanek, K. Dhanasekharan, R. Fan, C. Mancinelli, and R. Chern. A combined experimental and computational study of wet granulation in a Wurster fluid bed granulator. *Powder Technology* **189**, 190-201, (2009).
69. Saleh, K., D. Steinmetz, and M. Hemati. Experimental study and modeling of fluidized bed coating and agglomeration. *Powder Technology* **130**, 116-123, (2003).
70. Weber, M.W. and C.M. Hrenya. Square-well model for cohesion in fluidized beds. *Chemical Engineering Science* **61**, 4511-4527, (2006).
71. Talu, I., G.I. Tardos, and M.I. Khan. Computer simulation of wet granulation. *Powder Technology* **110**, 59-75, (2000).
72. Lian, G., C. Thornton, and M. Adams. Discrete particle simulation of agglomerate impact coalescence. *Chemical Engineering Science* **53**, 3381-3391, (1998).
73. Khan, M.I. and G.I. Tardos. Stability of wet agglomerates in granular shear flows. *Journal of Fluid Mechanics* **347**, 347-368, (1997).
74. Jain, K., D.L. Shi, and J.J. McCarthy. Discrete characterization of cohesion in gas-solid flows. *Powder Technology* **146**, 160-167, (2004).
75. Zhang, R. and J. Li. Simulation on mechanical behavior of cohesive soil by Distinct Element Method. *Journal of terramechanics* **43**, 303-316, (2006).
76. Shi, D. and J.J. McCarthy. Numerical simulation of liquid transfer between particles. *Powder Technology* **184**, 64-75, (2008).
77. Kantak, A.A., C.M. Hrenya, and R.H. Davis. Initial rates of aggregation for dilute, granular flows of wet particles. *Physics of Fluids* **21**, 23301, (2009).
78. Hulbert, H. and S. Katz. Chem. *Engng Sci* **19**, 555, (1964).
79. Randolph, A.D. and M.A. Larson. Theory of particulate processes. (Academic Press New York, 1971).
80. Iveson, S.M. Limitations of one-dimensional population balance models of wet granulation processes. *Powder Technology* **124**, 219-229, (2002).
81. X. Liu, L. and J. D. Litster. Population balance modelling of granulation with a physically based coalescence kernel. *Chemical Engineering Science* **57**, 2183-2191, (2002).

82. Litster, J. and B. Ennis. The science and engineering of granulation processes. Vol. 15 (Kluwer Academic Pub, 2004).

2. NEWTON'S CRADLE: NORMAL COLLISIONS BETWEEN THREE DRY SPHERES[1]

2.1. Abstract

Using an apparatus inspired by Newton's cradle, the simultaneous, normal collision between three solid spheres is examined. Namely, an initially touching, motionless pair of 'target' particles (doublet) is impacted on one end by a third 'striker' particle. Measurements of post-collisional velocities and collision durations are obtained via high-speed photography and an electrical circuit, respectively. Contrary to intuition, the expected Newton's cradle outcome of a motionless, touching particle pair at the bottom of the pendulum arc is not observed in either case. Instead, the striker particle reverses its direction and separates from the middle particle after collision. This reversal is not observed, however, if the target particles are separated by a small distance (not in contact) initially, although a separation still occurs between the striker and middle particle after the collision, with both particles traveling in the same direction. For the case of initially touching target particles, contact duration measurements indicate that the striker separates from the three particles before the two target particles separate.

---

[1] Donahue, C.M., C.M. Hrenya, A.P. Zelinskaya, and K.J. Nakagawa. Newton's cradle undone: Experiments and collision models for the normal collision of three solid spheres. *Physics of Fluids* **20**, (2008).

However, when the targets are slightly separated, a three-particle collision is never observed, and the collision is, in fact, a series of two-body collisions. A subsequent implementation of a variety of hard-sphere and soft-sphere collision models indicates that a three-body (soft-sphere) treatment is essential for predicting the velocity reversal, consistent with the experimental findings. Finally, a direct comparison between model predictions and measurements of post-collisional velocities and contact durations provides a gauge of the relative merits of existing collision models for three-body interactions.

2.2. Introduction

The description of granular materials via a discrete-particle approach has become an increasingly popular tool in the field since the pioneering work of Cundall and Strack [1]. Although a more detailed description of particle contacts is possible via theoretical contact mechanics [2], the computational overhead associated with the resulting partial differential equations is prohibitive for many-particle systems. As a result, a variety of simplified collision models, or force laws, have been proposed. These force laws can be incorporated into Newton's second law of motion, and thus only require integration in time, thereby considerably lowering the computational overhead. Generally speaking, two types of collision models are available. Hard-sphere models treat collisions as binary and instantaneous, whereas soft-sphere models allow for enduring collisions between two or more particles. The advantage of the hard-sphere treatments is their relatively low computational requirement (resolving transients of the collisional process is not required so a larger time step is allowed), whereas the advantage of soft-sphere models is their

applicability to dense systems in which multi-particle contacts occur. In the current effort, the focus is on collision models for normal (head-on) contacts; a recent review of tangential force laws is given by Kruggel-Emden *et al.* [3].

A plethora of soft-sphere models have appeared in the literature [4-13]. These models, which take the form of force laws, can generally be broken down into two categories: spring-dashpot treatments and two-spring treatments. The spring-dashpot treatment is used for viscoelastic losses, in which no permanent deformation occurs. The two-spring treatment, on the other hand, utilizes a different spring for the loading and unloading phases of the collision to mimic permanent, plastic deformation. One challenge associated with the use of such soft-sphere models is the specification of model parameters, typically a spring constant(s) and/or dashpot coefficient. Unlike the parameters associated with a hard-sphere model, which are measurable, physical quantities like the restitution coefficient, the spring constant and dashpot coefficient cannot be directly measured. Instead, their values can be chosen to match measurable, integrated collision quantities, like the restitution coefficient and collision duration [14-19].

To date, the predictive ability of soft-sphere collision models has only been evaluated via comparisons with experiments for *two-body* collisions [13, 19, 20], which is somewhat surprising given that a major advantage of such models is their applicability to collisions involving more than two particles. Nonetheless, these studies have revealed interesting differences between the various force laws. In particular, two unrealistic behaviors are observed for several of the models: (i) the restitution coefficient may

increase with impact velocity, contrary to experimental data, and (ii) an unrealistic attractive force may be present at the end of the rebound phase.

Unlike previous efforts, the focus of the current work is on *three-body* collisions. A combination of experiments and modeling is used. Namely, in the first phase of the work, experiments are carried out using an apparatus inspired by Newton's cradle – the desktop toy made up of solid spheres suspended from V-shaped line in which a multi-body collision is prompted via the pulling up and subsequent release of one of the 'end' spheres. High-speed photography is used to capture the pre- and post-collisional velocities of each sphere and a circuit connected to the spheres is used to measure the contact duration. Unlike the typically expected outcome in which the striker (released) and middle particle remain motionless and touching at the bottom of the arc, the measurements reveal a separation of these two particles in which the striker particle actually reverses its direction after collision. Moreover, contact duration measurements reveal that the striker and the middle particles separate before the middle and end particles. However, if the two particles, which are initially motionless at the beginning of the experiment, are separated slightly prior to release of the impacting particle, the velocity reversal is not observed, though the two particles do exhibit a separation while traveling in the same direction. In this instance, it is confirmed through contact duration measurements that a series of two-body collisions occurs.

Previous efforts have been made to study the outcomes of the 'Newton's Cradle'. Herrmann and Seitz [7] observed the separation of the particles through only a Hertz contact law and computer simulations. In the work by Hinch and Saint-Jean [21], a theoretical investigation found that there was a velocity reversal for at least the striker

and possibly more of the particles depending on the number of particles. However, no experimental evidence was presented and only purely elastic particles where chosen. Ceanga and Hurmuzlu [22] introduced the *Impulse Transmission Ratio* as a way to resolve non-uniqueness when using momentum conservation. While they did conduct experiments, they never provided data on a collision between particles of the same mass and material. In this work, the focus is on the three-body nature of the problem.

In the second phase of this work, the experimental data is used to gauge the predictive ability of the various soft-sphere models. Moreover, a simplified description of the collisional process, which is often used to explain the Newton's cradle outcome, is considered. Specifically, a hard-sphere model is utilized in which the three-body collision is approximated as a series of instantaneous, two-body collisions. Overall, the model results are qualitatively consistent with the experimental findings, namely that a three-body (soft-sphere) treatment leads to velocity reversal, whereas a two-body (hard-sphere) treatment does not. Furthermore, both treatments predict the observed separation of all particles after the collisions. With regard to contact duration, the soft-sphere models correctly predict that the striker particle separates from the three-body contact prior to the separation of the two initially motionless particles. Quantitative model-data comparisons are also made, though the emphasis of this work is targeted at the differences between three-body collisions and two-body collisions, rather than providing a critical analysis between existing soft-sphere models.

2.3. Experimental Method

To investigate the post-collisional behavior of a normal (head-on) collision between three solid spheres, a pendulum-based apparatus inspired by Newton's cradle is used. As illustrated in Figure 2.1, each particle is hung from two lines to make a V-shape. The pivot points in each V-shaped pendulum are approximately 33 cm apart and the length of each line is 1 m. The three pendulums are spaced one particle diameter (2.54 cm) apart, so that when not in motion, the particles are touching, but no force occurs between them.

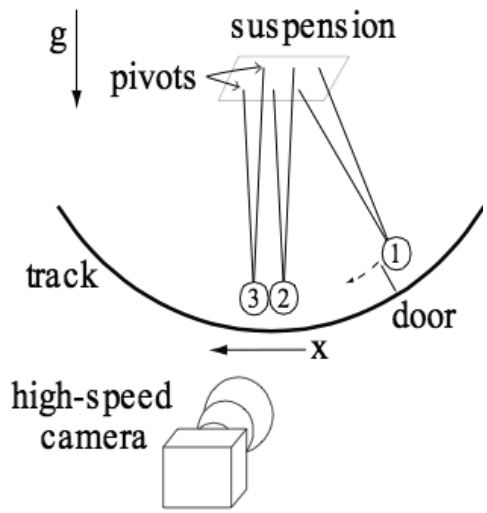

Figure 2.1 Schematic of Newton's cradle experiments

The pendulum line is made of ice fishing line manufactured by Berkley with a spring constant of 1.2 kN/m. The stiff line balances the centripetal force experienced by the striker particle as it travels down the arc, effectively eliminating any vertical motion upon collision with the stationary particles at the bottom of the arc. The line is strung to the particles via a small, metal tube welded on the top of the particles, and all-purpose

glue holds the line and tube together. For a given experiment, all three particles are fabricated from one of two types of materials, chrome steel (AISI 52100) or stainless steel (316 grade). The properties of the chrome steel particles are: Young's modulus E = 2.03×10^{11} N/m^2; Poisson's Ratio $\nu = 0.28$; yield strength $Y = 2.03\times10^{9}$ N/m^2; density ρ = 7830 kg/m^3; radius R = 1.27 cm. The properties of the stainless steel particles are: Young's Modulus E = 1.93×10^{11} N/m^2; Poisson's ratio ν = 0.35; yield strength Y = 3.10×10^{8} N/m^2; density $\rho = 8030$ kg/m^3; radius $R = 1.27$ cm.

The normal, three-body collision is achieved by pulling back along the arc the striker particle, which is then released and allowed to collide with the two motionless, touching particles at the bottom of the arc. As labeled in Figure 2.1, particle 1 refers to the striker particle, particle 2 refers to the middle particle, and particle 3 is the end particle opposite to the striker particle. The striker particle is held by a door attached to a track along the arc. The position of the door can be moved along the track in order to achieve different impacting velocities when released. The door is spring-loaded and is released by a solenoid. Once released, particle 1 collides with particle 2, and particles 2 and 3 travel up the arc. Due to gravity, g, the particles will eventually come back down the arc and collide a second time; however, data is only taken before and after the first three-body collision.

The velocities of each particle before and after collision are measured using a high-speed camera. The camera is manufactured by DVC (model 340M) with a 640×480 pixel resolution. To increase the rate of image collection, unnecessary border pixels are cropped out. Depending on the exact distance of the camera and velocity of the incident

particle, the resulting resolution is approximately 400×50 to 600×150 pixels. To minimize the effect of wide-angle distortion, a Navitar 7000 zoom lens is used so that the camera can be placed approximately 1.5 m away from the pendulum apparatus. It is run at 40MHz and produces a snapshot every 3.1 ms. The series of snapshots are imported into Matlab in order to find the position of each particle center in each frame. The grayscale frames are converted into black-and-white images, with white particles appearing on a black background. The particle edges are then eroded using a pre-existing function in Matlab, namely *imerode*, in order to separate touching particles so they do not appear to be one object in Matlab. The function *regionprops* calculates the centroid of each particle. Five images before and after the collision are used to calculate the pre- and post-collisional velocities, respectively. The frames during collision, however, are not used due to noise resulting from the collision. The velocities are determined by finding the slope of a linear fit of the centroids of the particles versus time for a given set of five images. Based on these velocities, momentum before and after a collision was found to be conserved within ~1%.

In addition to velocity measurements, contact durations associated with the collision are obtained by connecting a circuit to the steel particles such that the circuit is closed when particles are in contact. Figure 2.2 shows the circuit diagram. The circuit utilizes three different resistances such that different voltage obtained from the data acquisition card (DAQ) represents different contacts (i.e., between particles 1 and 2; 2 and 3; 1,2 and 3).

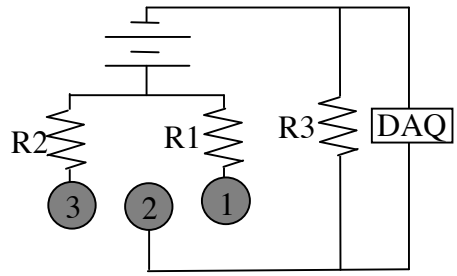

Figure 2.2 Circuit diagram for measuring contact duration

2.4. Collisional Models

2.4.1. Soft-sphere models

The first approach used to simulate the Newton's cradle experiments is the soft-sphere collision model, which accounts for the simultaneous, enduring nature of the collision between the three particles. A variety of models have been proposed in the literature, and those examined here are identical to those investigated by Stevens and Hrenya [19] for the case of two-particle collisions. Namely, the soft-sphere models considered here, along with their abbreviations, are: Hertz, linear spring and dashpot – LSD, Kuwabara and Kono [5] – KK, Lee and Hermann [7] – LH, Walton and Braun [4] with constant restitution coefficient – WBCE, Walton and Braun [4] with variable restitution coefficient – WBVE, and Thornton [10] – T. Note that the Hertz model is

targeted at the idealized case of perfectly elastic particles, and included here for purposes of comparison, as all other models account for inelasticity. Furthermore, the soft-sphere models proposed by Hertzsch *et al.* [9] and Brilliantov *et al.* [11] take the same form as that of Kuwabara and Kono [5], and thus are not listed separately. (Note that all of these models are quasi-static in nature. For the particles examined here, collision durations are larger than estimates of the wave propagation time [21], thereby lending support to the quasistatic treatment.)

Table 2.1 contains the force law for each of soft-sphere collisions models and the associated input parameters. The notation introduced in the table includes: subscripts a and b refer to properties associated with particle a and b, respectively (Figure 2.1); m refers to particle mass (if no subscript is included, equation is valid only for identical spheres with mass m); F_n refers to the (repulsive) normal force experienced by a particle during contact; and ξ refers to particle ''overlap''. The particle overlap is defined as

$$\xi = \max\left(0, R_a + R_b - \left|r_b - r_a\right|\right) \tag{2.1}$$

where r refers to the position of a given particle center. Also listed in Table 2.1 is the regime for which each of the force laws was developed. For further details, the reader is referred to Stevens and Hrenya [19].

A review of the qualitative differences between the various models is presented in Table 2.2. Although the majority of models predict a strictly repulsive interaction, the models of LSD, KK, and LH exhibit an attractive force upon rebound at small x. Although the magnitude of this force is fairly small, its presence is clearly unphysical for the non-cohesive particles under consideration. Another distinguishing feature among

the models is the presence of a force discontinuity at small x for the LSD and LH models. In addition to force predictions, the models also exhibit differences in the qualitative nature of the predicted restitution coefficient and collision duration. Contrary to experimental evidence that the restitution coefficient decreases with an increase in impact velocity, LSD and WBCE predict constant values while LH predicts an increasing value of the restitution coefficient with impact velocity. With regard to collision duration, LSD and WBCE predict constant values as the impact velocity is changed, while the remaining models correctly predict a decrease in collision duration with an increase in impact velocity. Model predictions exemplifying each of the behaviors listed in Table 2.2 are given by Stevens and Hrenya [19].

Table 2.1 Soft-sphere collision models

name	abbre-viation	regime	Inputs	force law
Hertz	--	elastic	$\tilde{k}_n = \frac{4}{3}\sqrt{R_{eff}}\,E_{eff}$ *where* $R_{eff} = R_a R_b / (R_a + R_b)$ $\frac{1}{E_{eff}} = \frac{(1-\nu_a^2)}{E_a} + \frac{(1-\nu_b^2)}{E_b}$	$F_n = \tilde{k}_n \; \xi^{3/2}$
linear-spring/dashpot	LSD	visco-elastic	$k_n,\ \beta_n$	$F_n = k_n \; \xi + \beta_n \; \gamma_{n,crit} \frac{d\xi}{dt}$ *where* $\gamma_{n,\,\mathrm{crit}} = 2\sqrt{m_{eff} k_n}$ $m_{eff} = m_a m_b / (m_a + m_b)$
Kuwabara and Kono[5]	KK	visco-elastic	$\tilde{k}_n,\ \gamma_{n2}$	$F_n = \tilde{k}_n \; \xi^{3/2} + \gamma_{n2} \; \xi^{1/2} \; \frac{d\xi}{dt}$
Lee and Hermann [7]	LH	visco-elastic	$\tilde{k}_n,\ \gamma_{n3}$	$F_n = \tilde{k}_n \; \xi^{3/2} + \gamma_{n3} \; m_{eff} \; V_n$ *where V_n = normal component of the relative velocity*
Walton and Braun/ constant-*e* [4]	WBCE	plastic	$k_L,\ k_U$	$F_{n,loading} = k_L \; \xi$ $F_{n,unloading} = -k_U \; (\xi - \xi_0)$ *where ξ_0 = value of ξ at which unloading force equals zero*
Walton and Braun/ variable-*e* [4]	WBVE	plastic	$k_L,\ S$	$F_{n,loading} = k_L \; \xi$ $F_{n,unloading} = (k_L + S \; F_{\max})(\xi - \xi_0)$ *where F_{max} = maximum force achieved prior to unloading*
Thornton [10]	T	plastic	$\tilde{k}_n,\ p_y$ *where p_y = "cutoff pressure"*	$F_{n,\,elastic\ loading} = \tilde{k}_n \; \xi^{3/2}$ $F_{n,\,plastic\ loading} = F_y + \pi \, p_y R_{eff} \; (\xi - \xi_y)$ $F_{n,\,elastic\ unloading} = \tilde{k}_n \; (\xi - \xi_p)^{3/2}$ *where $F_y = F_{n,\,elastic\ loading}$ at $\xi = \xi_y$* $\xi_y = R_{eff} \left(\frac{\pi \, p_y}{2 E_{eff}} \right)^2$ *ξ_p = value of ξ at which unloading force equals zero*

Table 2.2 Qualitative comparison of soft-sphere models

name	**abbre-viation**	**rebound force at small ξ** *(F vs. ξ)*	**value of force as $\xi \rightarrow 0$** *(F vs. ξ)*	**as V_{imp} increases, *e*…** *(e vs. V_{imp})*	**as V_{imp} increases, τ…** *(e vs. τ)*
expected behavior	--	repulsive	zero	decreases	decreases
Hertz	--	repulsive	zero	constant (e=1)	decreases
linear-spring/dashpot	LSD	attractive	nonzero	constant	constant
Kuwabara and Kono [5]	KK	attractive	zero	decreases	decreases
Lee and Hermann [7]	LH	attractive	nonzero	increases	decreases
Walton and Braun/ constant-*e* [4]	WBCE	repulsive	zero	constant	constant
Walton and Braun/ variable-*e* [4]	WBVE	repulsive	zero	decreases	decreases
Thornton [10]	T	repulsive	zero	decreases	=1 for $V_{imp} < V_{y,T}$ decreases for $V_{imp} > V_{y,T}$

Generally speaking, the soft-sphere models each require two input parameters that do not represent physical, measurable quantities (e.g., spring constant and dashpot coefficient). Based on their experiments involving the collision of two particles, Stevens and Hrenya [19] fitted the input parameters to match the experimental values for restitution coefficient and collision duration at the mid-range of impact velocities examined. Since the three-particle collisions examined here utilize the same solid materials and a similar range of impact velocities as used in the two-particle collisions of Stevens and Hrenya [19], identical values are used for the soft-sphere inputs; see Table 2.3 for specific values. It is worthwhile to note that the force models of Kuwabara and Kono [5] and Lee and Herrmann [7] are defined in terms of the Hertzian spring constant

$\tilde{k}_n$, which depends on the particle properties R, E, and n (Table 2.1). Although $\tilde{k}_n$ is used as a fitting parameter in the KK and LH models as described above, its fitted value is nearly identical to the Hertzian value, as evidenced in Table 2.3. Similarly, the inputs to the Thornton model [10] are based on material properties, though Thornton and coworkers have recognized the sensitivity of the predictions to the value used for the ''cutoff pressure'' (p_y) input [23, 24], and have fitted this value to match measurements of other quantities [25, 26]. Accordingly, the fitted value of p_y obtained by Stevens and Hrenya [19] is used in the current effort.

To obtain model predictions for the post-collisional velocities of all particles using the various soft-sphere models, three identical particles are initially positioned in a line and touching but not overlapping (separated by two particle radii). In order to mimic the Newton's cradle setup (Figure 2.1), particles 2 and 3 are initially motionless, while particle 1 is given a nonzero, impact velocity, V_{imp}, in the direction of particle 2. The position and velocity of each particle is then tracked throughout the collisional process using the force laws given in Table 2.1. Specifically, the repulsive force F_n is determined at any point in time as a function of overlap x, and this force is used in conjunction with Newton's law of motion (no other forces are considered) to move forward in time. An explicit integration scheme is used to solve the initial-value problem. The corresponding time step, which is typically $3\text{x}10^{-8}$ s, is small enough to ensure negligible numerical errors. Once none of the particles remain in contact, the post-collisional velocities of particles 1, 2, and 3, namely V_1, V_2, and V_3, respectively, are recorded.

Table 2.3 Input values for soft-sphere collision models. The units are as follows: $\tilde{k}_n = N/m^{3/2}$, $k_n = N/m$, $k_L = N/m$, $\beta_n = kg/\left(m^2 s^2\right)$, $\gamma_{n2} = kg/\left(m^{1/2} s\right)$, $\gamma_{n3} = 1/s$, $k_U = N/m$, $S = 1/m$, and $p_y = N/m^2$.

name	abbre-viation	stainless steel: input 1	stainless steel: input 2	chrome steel: input 1	chrome steel: input 2
Hertz	--	$\tilde{k}_n = 1.17 \cdot 10^{10}$	--	$\tilde{k}_n = 1.17 \cdot 10^{10}$	--
linear-spring/dashpot	LSD	$k_n = 5.16 \cdot 10^7$	$\beta_n = 4.10 \cdot 10^{-2}$	$k_n = 6.25 \cdot 10^7$	$\beta_n = 4.50 \cdot 10^{-3}$
Kuwabara and Kono [5]	KK	$\tilde{k}_n = 1.21 \cdot 10^{10}$	$\gamma_{n2} = 3.41 \cdot 10^4$	$\tilde{k}_n = 1.28 \cdot 10^{10}$	$\gamma_{n2} = 3.50 \cdot 10^3$
Lee and Hermann [7]	LH	$\tilde{k}_n = 1.21 \cdot 10^{10}$	$\gamma_{n3} = 2.85 \cdot 10^3$	$\tilde{k}_n = 1.28 \cdot 10^{10}$	$\gamma_{n3} = 3.50 \cdot 10^2$
Walton and Braun/ constant-*e* [4]	WBCE	$k_L = 4.54 \cdot 10^7$	$k_U = 5.88 \cdot 10^7$	$k_L = 6.16 \cdot 10^7$	$k_U = 6.33 \cdot 10^7$
Walton and Braun/ variable-*e* [4]	WBVE	$k_L = 4.54 \cdot 10^7$	$S = 1.27 \cdot 10^4$	$k_L = 6.16 \cdot 10^7$	$S = 1.05 \cdot 10^3$
Thornton [10]	T	$p_y = 9.14Y$	--	$p_y = 2.13Y$	--

2.4.2. Hard-sphere models

As an alternative to the soft-sphere collision described in the previous section, the hard-sphere model can also be used to *approximate* the three-body interaction. In particular, although the hard-sphere model is limited to binary interactions, the three-body collision can be approximated as a series of two-body collisions as detailed below. The motivation for examining this simplification is its ability to predict the expected Newton's cradle outcome ($V_1 = V_2 = 0$ and $V_3 = V_{imp}$) for perfectly elastic spheres. More specifically, since the hard-sphere treatment is less computationally extensive than its soft-sphere counterpart, the application of hard-sphere models to collisions involving more than two particles is attractive if model accuracy is not sacrificed.

In mathematical terms, the hard-sphere model for an instantaneous collision between *two* particles derives from the conservation of momentum and a kinetic energy balance. For the simplified case considered here in which particles are identical and the only nonzero component of velocity is the normal component, the collision model takes the form

$$V_a = V_{ao} - \frac{m}{2}(1+e)(V_{ao} - V_{bo}) \tag{2.2}$$

$$V_b = V_{bo} + \frac{m}{2}(1+e)(V_{ao} - V_{bo}) \tag{2.3}$$

where V_{ao} and V_{bo} are the pre-collisional velocities of particles a and b, respectively; V_a and V_b are the corresponding post-collisional velocities; and e is restitution coefficient defined as

$$e = -\frac{V_a - V_b}{V_{ao} - V_{bo}} \ . \tag{2.4}$$

The restitution coefficient is a measure of particle inelasticity, varying between 1 for perfectly elastic particles and 0 for perfectly soft particles. Although e is a function of impact velocity, the values used in the hard-sphere model are assumed constant for purposes of simplicity, as this assumption does not impact the conclusions. In particular, e = 0.88 and 0.99 are used for the stainless and chrome steel systems, respectively, based on the measurements of Stevens and Hrenya [19] in the mid-range of the velocities examined.

To apply the two-particle (hard-sphere) collision model to the three-body collision, a series of two-body collisions is carried out by assuming an infinitesimal spacing between the initially motionless particles (particles 2 and 3 in Figure 2.1). Accordingly, the post-collisional velocities particles 1 and 2 (V_1 and V_2) are first found using Equations 2.2 and 2.3 where $V_{1o} = V_{imp}$ and $V_{2o} = 0$. The post-collisional velocity of particle 2 (V_2) is then used as the pre-collisional velocity when resolving the subsequent collision between particles 2 and 3 ($V_{2o} = V_2$ and $V_{3o} = 0$). Once the outcomes of this first series of collisions is performed, a check is then made as to whether $V_1 < V_2$ and $V_2 < V_3$. Otherwise, a faster particle will catch up to the slower particle and a secondary collision will occur. In all of the (inelastic) cases examined here, $V_1 > V_2$ and $V_2 < V_3$ after the first series collisions, so a secondary collision between particles 1 and 2 is resolved. The outcome of this secondary collision leads to $V_1 < V_2 < V_3$, so no further 'looping' is required.

As alluded to above, it is worthwhile to note that this hard-sphere treatment leads to the expected Newton's cradle outcome in the limiting case of $e = 1$. Namely, the first collision between particles 1 and 2 leads to a perfect exchange of velocity, as does the second collision between particles 2 and 3. Correspondingly, $V_3 = V_{imp}$ while particles 1 and 2 remain motionless at the bottom of the pendulum arc ($V_1 = V_2 = 0$).

2.5. Results and Discussion

In the first phase of the work, experiments are performed to characterize the outcome of the normal, three-body collision. Based on experience with the Newton's

cradle desktop toy (i.e., without the aid of a high-speed camera), the pulling away and subsequent release of the impacting particle (particle 1 in Figure 2.1) is expected to lead to a velocity exchange with the other end particle (particle 3), while particles 1 and 2 remain touching at the bottom of the arc. The experimental results obtained via high-speed imaging, however, indicate that the expected Newton's cradle outcome is not observed. Instead, particles 1 and 2 separate slowly after colliding, as shown in the snapshots and corresponding velocity data of Figure 2.3. The velocities and separation of particles 1 and 2 are quite small relative to that of particle 3, which explains why the desktop toy gives the *appearance* of the traditional Newton's cradle outcome. In fact, high-speed images were also taken of a commercially available Newton's cradle toy composed of five spheres, and the four spheres remaining at the bottom of the arc after collision were also observed to separate slightly. For purposes of notation, the Newton's cradle outcome (particles 1 and 2 in contact after collision) will hereafter be referred to as NC, while the fully separated outcome (no particles in contact after collision) will be referred to as FS.

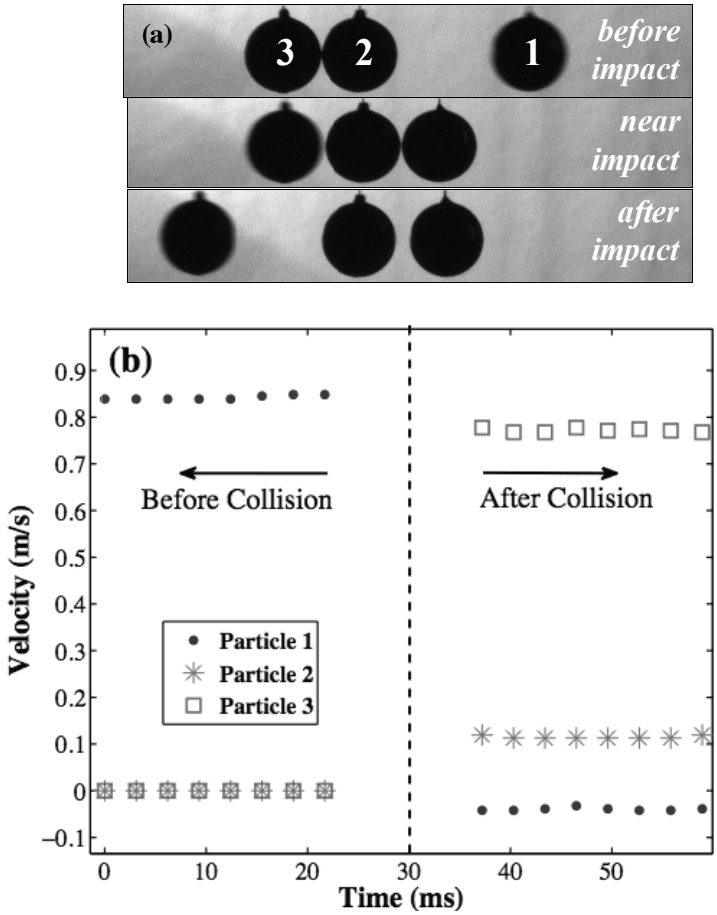

Figure 2.3 Example data from the Newton's cradle: (a) series of snapshots and (b) particle velocities versus time for stainless spheres and V_{imp} = 0.88 m/s.

Perhaps even more surprising than the FS outcome, though, the striker particle (particle 1) reverses its direction (negative velocity) after the collision (Figure 2.1). This behavior is representative of the entire parameter space investigated, as displayed in Figure 2.4. Specifically, Figure 2.4 contains plots of post-collisional velocities of each sphere (V_1, V_2, and V_3) over a range of impact velocities (V_{imp}) for the case of chrome steel (subplot a) and stainless steel (subplot b) particles. For each system, particles 1 and 2 display a slow separation after the collision (FS), with particle 1 reversing its direction and particle 2 continuing in the same direction as the impacting particle. Not surprisingly,

as the impact velocity increases, the post-collisional velocity of each particle also increases in magnitude.

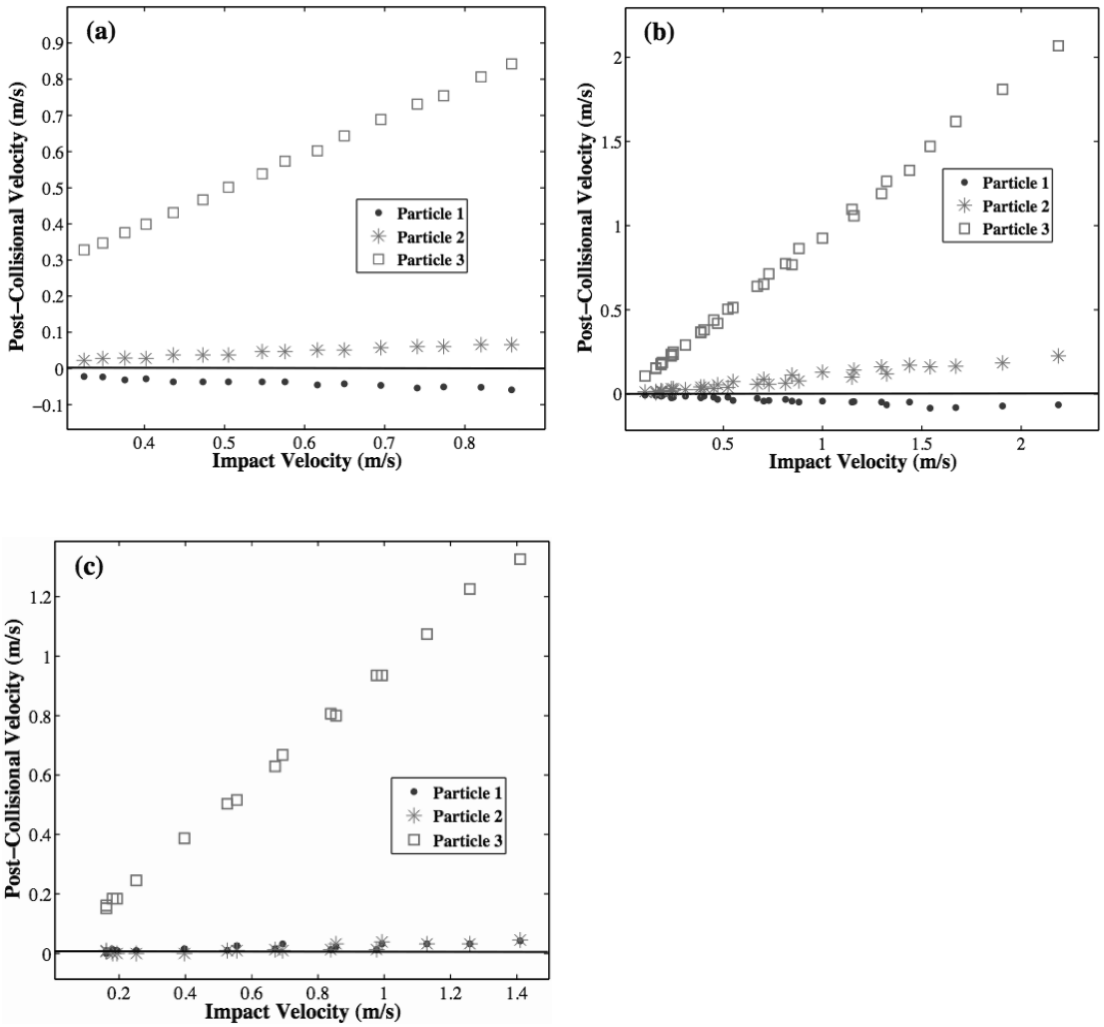

Figure 2.4 Experimental post-collisional velocities (V_1, V_2, V_3) for all particles at various impact velocities (V_{imp}) using (a) touching, chrome steel spheres, (b) touching, stainless steel spheres, and (c) non-touching, stainless steel spheres.

Figure 2.4c is analogous to Figure 2.4b, except that the initial state is different. Specifically, particles 2 and 3 are separated slightly prior to the release of particle 1 instead of being in contact. Hence, the first collision between particles 1 and 2 is a two-

body collision rather than a three-body collision. Furthermore, the contact duration measurements confirm that the subsequent collision is between particles 2 and 3 and does not involve particle 1 (i.e., a three-particle collision does not occur in this sequence). This small change in the initial conditions has a dramatic impact on the outcome, namely the velocity reversal of particle 1 is no longer observed. Although not evident from the resolution of data displayed in Figure 2.4c, a review of the snapshots (not shown) indicates that particles 1 and 2 do separate slightly (FS outcome) despite the absence of a velocity reversal. Thus, the experiments indicate that a three-body collision is associated with the reversal of particle 1, whereas a series of two-body collisions does not lead to such reversal.

In addition to the velocity measurements discussed above, contact duration measurements are also taken for the stainless steel particles. Results obtained when particles 2 and 3 are initially touching are shown in Figure 2.5a. At the time of impact, particles 1, 2 and 3 are in simultaneous contact, whereas in the last part of the collision only particles 2 and 3 are in contact (i.e., particle 1 separates first). Finally, after the collision, no particles are in contact as they all separate. Therefore, the contact duration between particles 1 and 2 (t_{12}) is equal to the duration of 1, 2 and 3 (t_{123}). The total contact duration of particles 2 and 3 (t_{23}) is equal to t_{123} plus the duration of 2 and 3 in the second part of the collision. In the scenario where the target particles are not initially touching as shown in 5b, particles 1 and 2 come in contact and separate, and then particles 2 and 3 come in contact and separate. The contact duration measurement between particles 1, 2 and 3 is zero and so does not appear in Figure 2.5b. Therefore, when the target particles are not touching initially, the collisional sequence is indeed a

series of two-body collisions, and a three-body collision never occurs. Additionally, t_{12} and t_{23} are statistically indistinguishable, which is not surprising since each is a two-body collision with similar impact velocities due to the high coefficient of restitution.

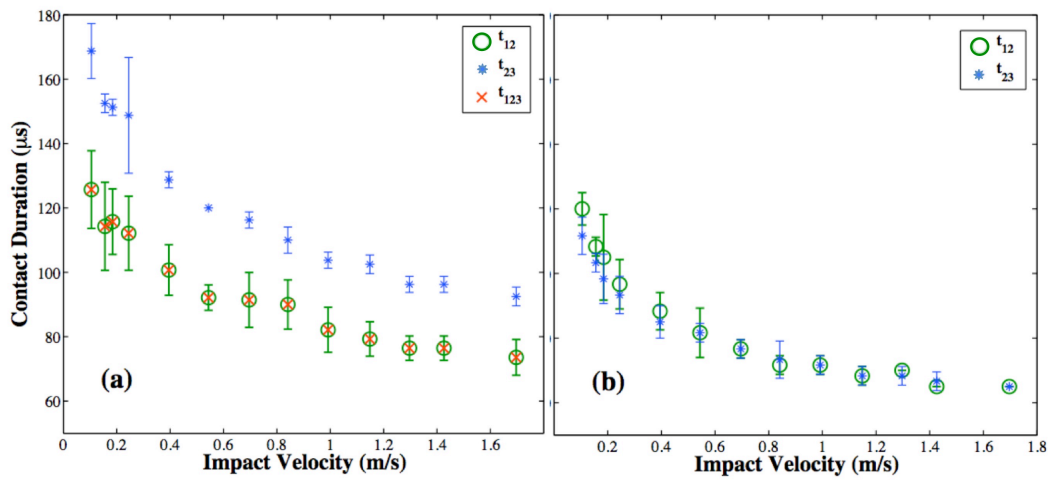

Figure 2.5 Contact duration measurements between particles 1 and 2 (t_{12}), and 2 and 3 (t_{23}) using stainless steel with (a) target particles touching and (b) target particles separated.

In the second phase of the work, predictions from the various collision models are compared to the experimental data. As described in Section 2.3, two approaches are used: (i) treating the interaction as a series of two-body collisions using hard-sphere collision models (Equation 2.2-2.3) and (ii) treating the interaction as a three-body collision using soft-sphere models (Table 2.1). For both approaches, in addition to using model inputs based measured values of e, the ideal case of $e = 1$ is also examined in order to assess the role of inelasticity on the collisional outcome. Figures 2.6-2.8 display the post-collisional velocities V_1, V_2, and V_3, respectively, for both the chrome steel (subplots a) and stainless steel (subplots b) spheres as a function of the impact velocity V_{imp}. The

various model predictions are displayed as lines and the experimental data are shown using data points. Note that circles are used for data collected when particles 2 and 3 are initially in contact, whereas squares are used for data obtained when particles 2 and 3 are initially separated. Recall that for all inelastic cases, the two-body treatment results in a secondary collision between particles 1 and 2 since particle 1 'catches up' to particle 2. It is the velocity resulting from this secondary collision that is reported in the plots for particles 1 (Figure 2.6) and 2 (Figure 2.7) since these final velocities are such that $V_3 > V_2 > V_1$ (i.e., no more 'catching up' will occur).

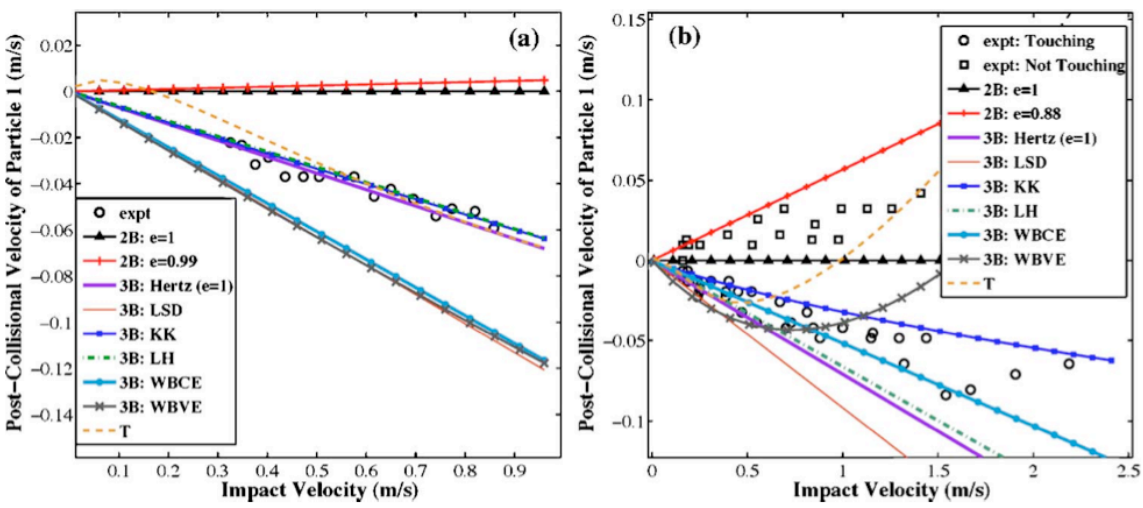

Figure 2.6 Predictions of post-collisional velocity of particle 1 (V_1) at various impact velocities (V_{imp}) using (a) chrome steel and (b) stainless steel spheres.

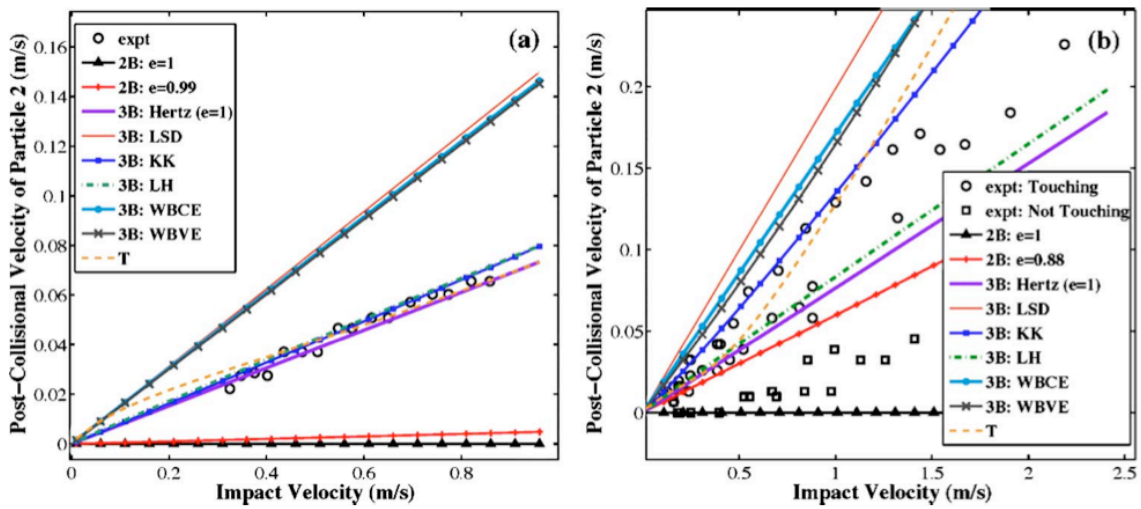

Figure 2.7 Predictions of post-collisional velocity of particle 2 (V_2) at various impact velocities (V_{imp}) using (a) chrome steel and (b) stainless steel spheres.

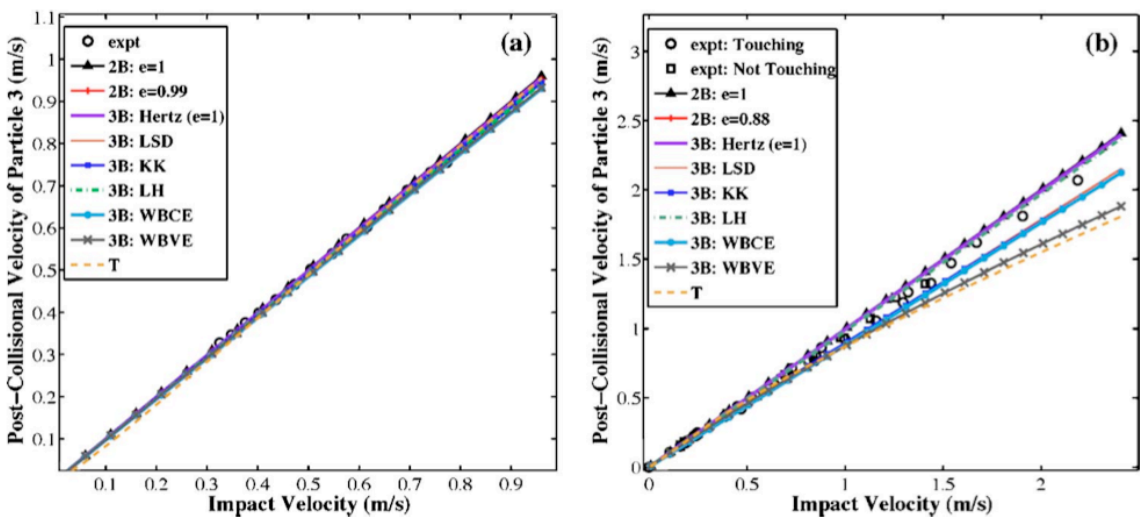

Figure 2.8 Predictions of post-collisional velocity of particle 3 (V_3) at various impact velocities (V_{imp}) using (a) chrome steel and (b) stainless steel spheres.

A cursory glance at Figures 2.6-2.8 indicates that the predictions for V_1 and V_2 (Figures 2.6 and 2.7) vary significantly between the various models, whereas predictions for V_3 (Figure 2.8) do not serve as a differentiator between models. In particular, for the

nearly elastic, chrome particles (Figure 2.8a), differences between all model predictions shown are essentially indistinguishable. More distinction arises for stainless particles (Figure 2.8b), which are slightly more dissipative, though differences are generally fairly small relative to those observed in Figures 2.6 and 2.7. For this reason, the remaining focus is on the data-model comparison for V_1 and V_2.

Perhaps the most interesting observations arising from Figures 2.6-2.7, is a comparison between the two-body and three-body predictions for (i) the collisional outcome (NC or FS) and (ii) the direction of the impacting particle after impact (reversal or otherwise). As evident from the plots, the only treatment that leads to a traditional Newton's cradle (NC) outcome is a two-body approximation for perfectly elastic particles (e = 1). In other words, since both V_1 and V_2 are predicted equal to zero for this case (Figures 2.6 and 2.7, respectively), particles 1 and 2 remain motionless and touching at the bottom of the arc while particle 3 bounces off with velocity V_{imp} since overall momentum is conserved. When e is lowered to realistic values for each of the materials (e = 0.99 for chrome steel and e = 0.88 for stainless steel), however, the fully separated (FS) outcome is observed using the two-body approximation, which is consistent with the experimental data. However, when considering the reversal of particle 1 after collision, the inelastic, two-body approximation is inconsistent with the data for systems in which particles 1 and 2 are initially in contact. Namely, for both chrome and stainless steel particles (Figures 2.6a and 2.6b, respectively), V_1 is predicted to be positive (moving right to left; no velocity reversal occurs) whereas the data indicates that V_1 is negative (moving left to right; a velocity reversal does occur). On the contrary, predictions obtained from models that account for three-body interactions do predict a velocity

reversal, including the Hertz model for perfectly elastic (e = 1) particles. (Note that the T and WBVE models only predict this reversal for a limited range of V_{imp}, whereas other soft-sphere models predict the reversal for all V_{imp}.) However, it is interesting to note that the non-reversal of particle 1 predicted by the two-body approximation is qualitatively consistent with the experimental observations obtained when particles 1 and 2 are not in contact initially. Recall that the contact duration measurements indicate that a series of two-body collisions takes place for this case (i.e., a three-body collision does not occur), and thus the sequence of events in the experiments with separation and the two-body approximation are consistent. Collectively, these comparisons indicate that a two-body approximation (hard-sphere model) is not capable of predicting the velocity reversal observed experimentally for a three-body collision, whereas the three-body treatments (soft-sphere models) do predict the reversal for all models examined.

In addition to the qualitative nature of the predictions discussed above, it is also worthwhile to consider the quantitative ability of the various three-body treatments. As mentioned above, such soft-sphere collision models have previously been evaluated using experimental data obtained from two-body collisions [13, 19, 20], so a direct comparison with data from a three-body collision is warranted. For these purposes, the data in which particles 2 and 3 are initially in contact is the relevant case. For the nearly-elastic chrome steel, the predictions obtained from the Hertz, KK, LH, and T models are in excellent agreement with the experimental data for V_1 and V_2 (Figures 2.6a and 2.7a, respectively), whereas the models of LSD, WBCE and WBVE over-predict the magnitudes of V_1 and V_2. For the more dissipative stainless steel, the comparisons are not as clear-cut due to noise in the data. The V_1 data generally falls between predictions obtained from the KK,

WBCE, and LH models (Figure 2.7b), whereas the V_2 data is typically located between predictions obtained from the KK, LH, and Hertz models (Figure 2.7c).

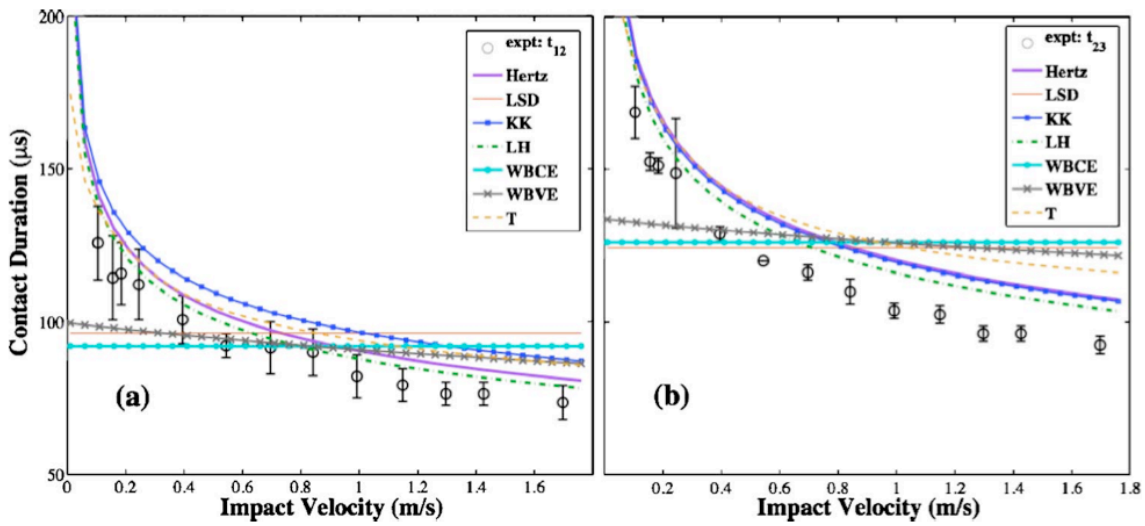

Figure 2.9 Contact durations (*a*) t_{12} and (*b*) t_{23} of stainless steel particles for target particles initially touching at various impact velocities (V_{imp}).

In addition to model-data comparison for post-collisional velocity, comparisons are also carried out for collision durations. Because the hard-sphere models contain an assumption of instantaneous collisions, the comparisons are restricted to soft-sphere models. In particular, for the case in which particles 2 and 3 are initially in contact, the durations associated with contacts between the 1-2 and 2-3 particles are displayed in Figures 2.9a and 2.9b, respectively, as a function of impact velocity. Consistent with the experimental trends, all models indicate that particle 1 separates from the three-particle contact prior to the separation of particles 2 and 3 (i.e., $t_{12} = t_{123} < t_{23}$). Also, the predictions of Hertz, KK, LH, WBVE, and T qualitatively agree with the experimental data for both t_{12} and t_{23} , namely a decrease in contact duration occurs with increasing

impact velocity. The models of LSD and WBCE, however, predict contact durations that are not dependent on impact velocity, contrary to the data. These trends of contact duration versus impact velocity are consistent with those observed by Stevens and Hrenya [19] for two-particle collisions. Finally, from a quantitative perspective, the predictions of Hertz, KK, LH, WBVE, and T generally over predict the experimental data for both t_{12} and t_{23}.

Finally, a sensitivity analysis of model predictions is carried with an eye toward the common practice of making spring constants artificially soft. More specifically, relatively hard particles, such as those investigated here, are characterized by short collision durations, which require the use of short time steps for the numerical integration of Newton's law of motion. To speed up the integration and thus allow for the simulation of more particles for the same CPU cost, spring constants are often made artificially small. The impact of such a treatment on predictions for the normal, three-body collision are carried out here using the KK model, which is chosen due to its relatively accurate performance. For the case of chrome steel, the spring constant is made four orders of magnitude smaller ($\tilde{k}_n = 1.28 \cdot 10^6$ N/m$^{3/2}$) and the dashpot coefficient is adjusted ($\gamma_{n2} = 14.0$ kg m$^{-1/2}$ s^{-1}) to match the experimental value of e obtained for two-body collisions [19]. This choice results in a two-body collision time which is 40 times greater than determined experimentally, as expected since the spring constant is artificially soft. When these inputs are used to model the three-body system, the post-collisional velocities of all particles are the same as those obtained with the original input values, though the duration of the impact is larger as expected.

2.6. Concluding Remarks

In this work, a Newton's cradle setup is used to investigate the simultaneous, normal collision between three solid spheres. Experiments are carried out with the aid of high-speed photography and an electrical circuit. Corresponding predictions of post-collisional velocities and contact durations are obtained from a variety of collision models, including soft-sphere models, which account for three-body interactions and hard-sphere models in which the three-body interaction is approximated as a series of two-body interactions.

According to the typical treatment of this system in introductory physics courses, perfectly elastic particles (e = 1) will lead to a *complete* velocity exchange between particles 1 and 3 ($V_3 = V_{imp}$), thereby illustrating the conservation of momentum. However, the experiments reveal a different outcome, which also satisfies the conservation of momentum. Namely, particles 1 and 2 separate slowly (relative to particle 3) at the bottom of the arc, with particle 1 exhibiting a reversal in its direction after impact. The reversal does not stem from the inelasticity of particles used. Instead, it is traced to three-body nature of the interaction, as all soft-sphere predictions, including the Hertz model for perfectly elastic particles, predict reversal, whereas all hard-sphere treatments do not. This statement is further corroborated by a modification to the experiments in which the particles at the bottom of the arc are separated by a small distance prior to impact instead of being in contact, which leads to a series of two-body collisions rather than a simultaneous three-body collision. For this case, no reversal is observed.

The contact duration measurements also reveal that, for the case of initially touching target particles, the impact is characterized by a simultaneous three-body contact immediately followed by a two-body contact involving the target particles. In other words, the striker particle is the first to separate from the three-body collision, followed by a separation between the target particles, leading to a fully separated final state. The contact-duration predictions obtained by all soft-sphere models under consideration are consistent with this experimental trend.

Also notable is the observation that the conventional Newton's cradle (NC) outcome is only predicted by hard-sphere (two-body) approximation for perfectly elastic spheres. All other model predictions, namely the hard-sphere approximation for inelastic particles and the soft-sphere predictions for both elastic and inelastic particles, result in a fully separated (FS) outcome. The FS outcome is consistent with the data but contrary to conventional wisdom that particles 1 and 2 remain motionless and touching at the bottom of the arc after impact.

From a quantitative perspective, the current results for three-body collisions share some similarities and differences with those obtained previously by Stevens and Hrenya [19] for collisions between 2 particles of the same materials. Namely, for the two-body collisions, the experimental restitution coefficient, which is a function of post-collisional velocities, generally falls between the predictions obtained by the soft-sphere models Kuwabara and Kono [5] and Walton and Braun (variable *e*) [4]. For the three-body collisions examined here, the Kuwabara and Kono [5] model displays the best overall performance in predicting the post-collisional velocities. However, even though the Kuwabara and Kono [5] model closely predicts the contact durations, Lee and Herman

[7] shows the best performance for stainless steel. Hence, some care should be taken when choosing the appropriate soft-sphere model for relatively dense systems characterized by a significant number of multi-body (>2) contacts; a choice based on the predictive ability for two-body contacts may not be appropriate.

It is worthwhile to point out that the materials examined here – stainless steel and chrome steel – are relatively hard. As noted by Stevens and Hrenya [19], the chrome steel may or may not exhibit slight plastic deformation ($V_y \sim V_{imp} < V_{fp}$; V_y is the yield velocity and V_{fp} is the velocity cutoff for the fully plastic indentation regime) and the stainless steel is likely to exhibit some plastic deformation ($V_y < V_{imp} < V_{fp}$). The good model-data match obtained using the Kuwabara and Kono [5] model for both post-collisional velocities and contact durations suggests that both materials are dominated by viscoelastic, rather than plastic, losses. Hence, further experiments are warranted for softer materials in order to assess the predictive ability of soft-sphere models targeted at plastic deformation.

Since the hard-sphere treatment is less computationally expensive than its soft-sphere counterpart, the application of hard-sphere models to collisions involving more than two particles is attractive if model accuracy is not sacrificed. In this work, the hard-sphere models are most notably inaccurate in their predictions of V_1 and V_2, and particularly the velocity reversal observed for particle 1. However, it is interesting to note that the magnitude of V_1 and V_2 are quite small relative to V_3, which is fairly well predicted by both hard-sphere and soft-sphere approaches. Hence, the implication of such inaccuracies on the prediction of macroscopic variables in many-body systems remains unknown and warrants further attention.

Finally, the sensitivity analysis of the Kuwabara and Kono [5] model performed here indicates that an artificial decrease in the spring constant has no negative impact on the prediction of the post-collisional velocities, as long as the dashpot coefficient is adjusted accordingly to match experimental values of the restitution coefficient. Note that this result is not intended to imply that the chosen value of the spring constant is inconsequential. On the contrary, an artificial decrease in the spring constant corresponds to an unrealistic increase in the contact duration [19], which may compromise model accuracy when applied to certain granular [27, 28] and gas-solid systems [29, 30].

Literature Cited

1. Cundall, P.A. and O. Strack. A discrete numerical model for granular assemblies. *Geotechnique* **29**, 47-65, (1979).
2. Johnson, K. Contact mechanics *eq.(7) and*, 294, (1985).
3. Kruggel-Emden, H., S. Wirtz, and V. Scherer. A study on tangential force laws applicable to the discrete element method (DEM) for materials with viscoelastic or plastic behavior. *Chemical Engineering Science* **63**, 1523-1541, (2008).
4. Walton, O.R. and R.L. Braun. Viscosity, granular-temperature, and stress calculations for shearing assemblies of inelastic, frictional disks. *Journal of Rheology* **30**, 949-980, (1986).
5. Kuwabara, G. and K. Kono. Restitution coefficient in a collision between two spheres. *Japanese journal of applied physics* **26**, 1230-1233, (1987).
6. Tsuji, Y., T. Tanaka, and T. Ishida. Lagrangian numerical simulation of plug flow of cohesionless particles in a horizontal pipe. *Powder Technology* **71**, 239-250, (1992).
7. Lee, J. and H.J. Herrmann. Angle of repose and angle of marginal stability: molecular dynamics of granular particles. *Journal of Physics A: Mathematical and General* **26**, 373, (1993).
8. Sadd, M.H., Q. Tai, and A. Shukla. Contact law effects on wave propagation in particulate materials using distinct element modeling. *International journal of non-linear mechanics* **28**, 251-265, (1993).
9. Hertzsch, J.M., F. Spahn, and N.V. Brilliantov. On low-velocity collisions of viscoelastic particles. *Journal de Physique II* **5**, 1725-1738, (1995).
10. Thornton, C. Coefficient of restitution for collinear collisions of elastic-perfectly plastic spheres. *Journal of Applied Mechanics* **64**, 383, (1997).
11. Brilliantov, N.V., F. Spahn, J.M. Hertzsch, and T. Poschel. Model for collisions in granular gases. *Physical Review E* **53**, 5382, (1996).

12. Vu-Quoc, L. and X. Zhang. An elastoplastic contact forceñdisplacement model in the normal direction: displacementñdriven version. *Proceedings of the Royal Society of London. Series A: Mathematical, Physical and Engineering Sciences* **455**, 4013, (1999).
13. Kruggel-Emden, H., E. Simsek, S. Rickelt, S. Wirtz, and V. Scherer. Review and extension of normal force models for the discrete element method. *Powder Technology* **171**, 157-173, (2007).
14. Goldsmith, W. Impact. (Arnold, 1960).
15. Bridges, F.G., A. Hatzes, and D. Lin. Structure, stability and evolution of Saturn's rings. (1984).
16. Foerster, S.F., M.Y. Louge, A.H. Chang, and K. Allia. Measurements of the Collision Properties of Small Spheres. *Physics of Fluids* **6**, 1108-1115, (1994).
17. Labous, L., A.D. Rosato, and R.N. Dave. Measurements of collisional properties of spheres using high-speed video analysis. *Physical Review E* **56**, 5717-5725, (1997).
18. Gorham, D. and A. Kharaz. The measurement of particle rebound characteristics. *Powder Technology* **112**, 193-202, (2000).
19. Hrenya, C.M. and A.B. Stevens. Comparison of soft-sphere models to measurements of collision properties during normal impacts. *Powder Technology* **154**, 99-109, (2005).
20. Dippel, S. and D. Wolf. Force schemes in simulations of granular materials. *Journal de physique I* **6**, 5-20, (1996).
21. Hinch, E. and S. SaintñJean. The fragmentation of a line of balls by an impact. *Proceedings of the Royal Society of London. Series A: Mathematical, Physical and Engineering Sciences* **455**, 3201, (1999).
22. Ceanga, V. and Y. Hurmuzlu. A new look at an old problem: Newton's cradle. *Journal of Applied Mechanics* **68**, 575, (2001).
23. Thornton, C. and Z. Ning. A theoretical model for the stick/bounce behaviour of adhesive, elastic-plastic spheres. *Powder Technology* **99**, 154-162, (1998).
24. Wu, C., L. Li, and C. Thornton. Rebound behaviour of spheres for plastic impacts. *International journal of impact engineering* **28**, 929-946, (2003).
25. Mishra, B. and C. Thornton. An improved contact model for ball mill simulation by the discrete element method. *Advanced Powder Technology* **13**, 25-41, (2002).
26. Sheng, Y., C. Lawrence, B. Briscoe, and C. Thornton. Numerical studies of uniaxial powder compaction process by 3D DEM. *Engineering Computations* **21**, 304-317, (2004).
27. Luding, S., E. ClÈment, A. Blumen, J. Rajchenbach, and J. Duran. Anomalous energy dissipation in molecular-dynamics simulations of grains: The``detachment"effect. *Physical Review E* **50**, 4113-4122, (1994).
28. Ketterhagen, W.R., J.S. Curtis, and C.R. Wassgren. Stress results from two-dimensional granular shear flow simulations using various collision models. *Physical Review E* **71**, 61307, (2005).
29. Weber, M.W. and C.M. Hrenya. Square-well model for cohesion in fluidized beds. *Chemical Engineering Science* **61**, 4511-4527, (2006).
30. Leboreiro Hernandez, J., *Influence of drag laws on segregation and bubbling behavior in gas-fluidized beds*. 2008, University of Colorado at Boulder.

3. STOKES'S CRADLE: NORMAL COLLISIONS BETWEEN THREE WETTED PARTICLES[2]

3.1. Abstract

In this work, a combination of experiments and theory is used to investigate three-body normal collisions between solid particles with a liquid coating. Experiments are carried out using a Stokes's cradle, an apparatus inspired by the Newton's cradle desktop toy except with wetted particles. Unlike previous work on two-body systems, which may either agglomerate or rebound upon collision, four outcomes are possible in three-body systems: fully agglomerated, Newton's cradle (striker and target particle it strikes agglomerate), reverse Newton's cradle (targets agglomerate while striker separates) and fully separated. Post-collisional velocities are measured over a range of parameters. For all experiments, as the impact velocity increases, the progression of outcomes observed is fully agglomerated, reverse Newton's cradle and fully separated. Notably, as the viscosity of the oil increases, experiments reveal a decrease in the critical Stokes number (the Stokes number that demarcates a transition from agglomeration to separation) for both sets of adjacent particles. A scaling theory is developed based on lubrication forces and particle deformation and elasticity. Unlike previous work for two-particle systems, two pieces of physics are found to be critical in the prediction of a regime map that is

---

[2] Donahue, C.M., C.M. Hrenya, R.H. Davis, K.J. Nakagawa, A.P. Zelinskaya, and G.G. Joseph. Stokes' cradle: normal three-body collisions between wetted particles. *Journal of Fluid Mechanics* **650**, 479-504, (2010).

consistent with experiments: (i) an additional resistance upon rebound of the target particles due to the pre-existing liquid bridge between them (which has no counterpart in two-particle collisions), and (ii) the addition of a rebound criterion due to glass transition of the liquid layer at high pressure between colliding particles.

3.2. Introduction

Prior studies of wetted collisions have focused on two-body systems, either between a particle and a wetted wall or between two particles. However, in many-particle flows simultaneous collisions between three or more spheres are common, even for relatively dilute flows. For dilute flows of non-wetted (dry) elastic particles, the probability of a collision involving three or more particles is low since the collisional time is small compared to the time between collisions. In wet flows, however, a contact involving three or more particles occurs whenever a pre-existing agglomerate collides with a particle or another agglomerate.

A key difference between a two-particle collision and a collision of a single particle with a pre-existing agglomerate is the number of possible outcomes. In two-body collisions, only two outcomes are possible, agglomeration or de-agglomeration. In this effort, the focus is on three-body collisions between an incoming striker particle and two initially touching, motionless, target particles (i.e., these particles are initially agglomerated), with all particles arranged in a line to ensure normal collisions. With the addition of this third particle, now four outcomes are possible for wetted systems: fully agglomerated (FA); 'Newton's cradle' (NC), in which the striker and the target particle it

strikes agglomerate while the last target particle is separated, named after the outcome commonly associated with the (dry) desktop toy; 'reverse Newton's cradle' (RNC), in which the striker is separated and the two targets are agglomerated; and fully separated (FS).

To build on previous efforts, the focus of the current effort is on normal (head-on), three-body, wetted collisions, which are investigated using a combination of experiments and theory. The experiments are conducted using an apparatus inspired by the Newton's cradle desktop toy. In this 'wetted' operation, the apparatus is referred to as the 'Stokes's cradle' since the fluid motion in the liquid layer between colliding particles is described by Stokes (low-*Re*) flow. A series of experiments is conducted with variations in fluid viscosity, thickness of the liquid layer, particle material, and impact velocity of the striker particle. Comparisons of observed outcomes to predictions reveal new and interesting physical processes not present in two-body systems. First, for a three-particle collision, excess liquid exists in the bridge connecting the two initially-agglomerated target particles (whereas two-particle collisions do not have a liquid bridge prior to contact). Because the thickness of this bridge is orders of magnitude larger during the rebound phase compared to the initial liquid thickness between target particles, the additional resistance provided by this 'excess' liquid is key to capturing the outcomes observed experimentally. Second, the glass transition of the liquid layer between colliding particles adds more 'bounce', which proves to be essential in predicting the correct outcomes.

3.3. Experimental Setup, Materials and Methods

The apparatus used in this Chapter is the same as in Chapter 2, but with modifications to wet the particles (Figure 3.1). A coating bath directly underneath the target particles is lifted to coat the particles. Two silicon oils with different viscosities are used to coat the particles, namely 12 Pa·s and 5.1 Pa·s at 25 °C, the nominal temperature of the experiments. The oil densities are both 0.97 g/cm^3. Unlike the Newton's cradle, the three pendulums are spaced 2.9 cm apart, which is slightly larger than one particle diameter (2.54 cm). This extra spacing ensures that sufficient space exists for a liquid layer of non-zero thickness (i.e., liquid bridge) between the two motionless target particles at the bottom of the arc; if the pendulums were placed one diameter apart, the surfaces of the two particles would touch.

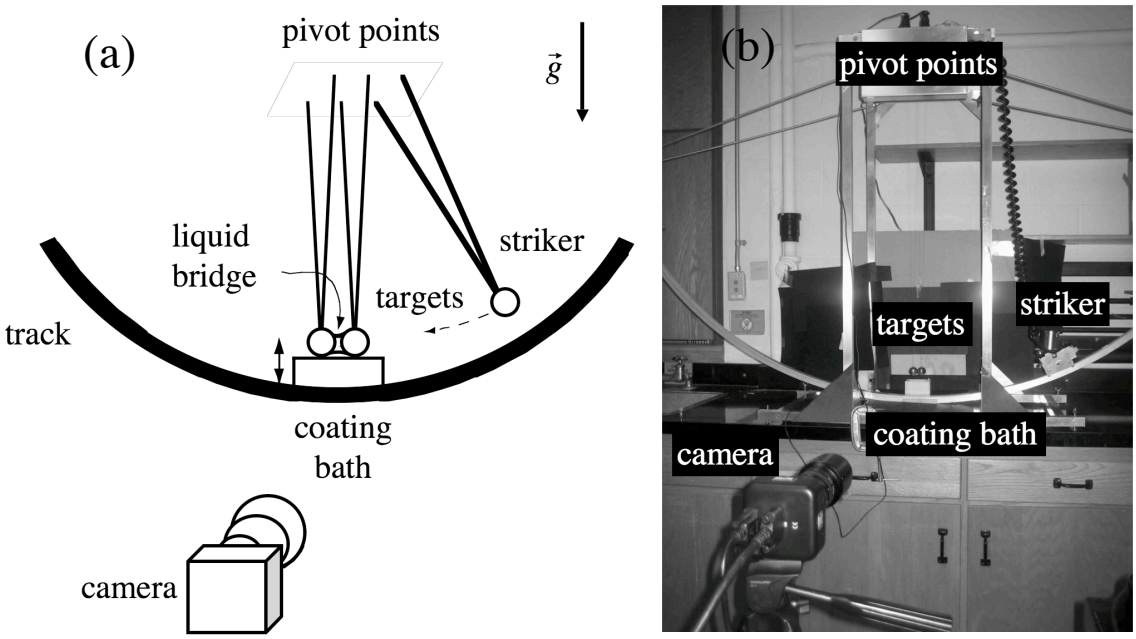

Figure 3.1 (a) Schematic and (b) photograph of Stokes's cradle experimental setup.

Example snapshots taken during the collision process are shown in Figure 3.2. Particle 1 refers to the striker particle, particle 2 refers to the first target particle, and particle 3 is the end target particle opposite the striker particle. Two types of measurements are taken to characterize each series of collisions: (i) the initial thickness of the liquid layers between the two target particles, $x_{0,2\text{-}3}$, and between the striker/target particles, $x_{0,1\text{-}2}$ (Figure 3.3 (b)), and (ii) the pre- and post-collisional velocities of each particle after the first series (right-to-left) of collisions. As detailed below, the former is performed off-line with a high-resolution camera, while the latter is performed with a separate high-speed camera.

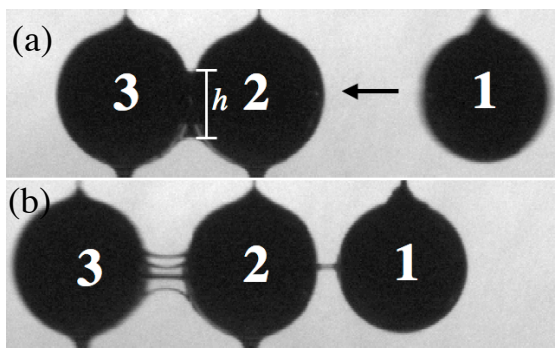

Figure 3.2 Snapshots of a three-particle wetted collision (a) just prior to collision and (b) after the collision using 12 Pa·s oil viscosity and stainless-steel particles (case lμ_ss_tn in Table 3.2).

At the beginning of the liquid-layer measurements, the two target particles are wetted using a coating bath placed underneath the particles, as shown in Figure 3.3a. The coating bath is raised to immerse the particles in silicon oil and is then slowly lowered. The thickness of the layer will vary with time as the silicon oil drips from the particle. Accordingly, the oil thickness is measured over a range of time. Measurements

of the oil thicknesses are made via a high-resolution camera, a Pentax SLR K110D with 6.1 megapixels. To minimize the effect of wide-angle distortion, a zoom lens is used so that the camera can be placed approximately 1.5 m away from the pendulum apparatus. Photographs of the wet particles are taken every 3 seconds during the dripping process. Figure 3.3b is a representative photograph used to calculate the liquid thickness. The lighting, aperture, and shutter speed are set at levels to make the particle, and particularly the edge of the particle, well defined and dark with respect to the background. The particles are almost entirely darker than the background (except for where the flash is reflected), and at the top of each particle the green dots contrast against the red background (though not apparent from the black and white photograph). The dots serve as a reference point for image processing using built-in Matlab functions. Matlab analysis also locates the position of the outermost edge of the particles, which is the initial point of contact during the collision. Furthermore, photographs of the dry particles are also taken prior to their wetting. From these positions in the dry and wet photographs the geometry of the particle positions is sufficiently defined and the thickness of the outer layer, $x_{0,1\text{-}2}$, and the thickness of the inner layer between the particles, $x_{0,2\text{-}3}$, can be calculated (Figure 3.3b). An example of the dependence of the layer thicknesses with time is shown in Figure 3.3c.

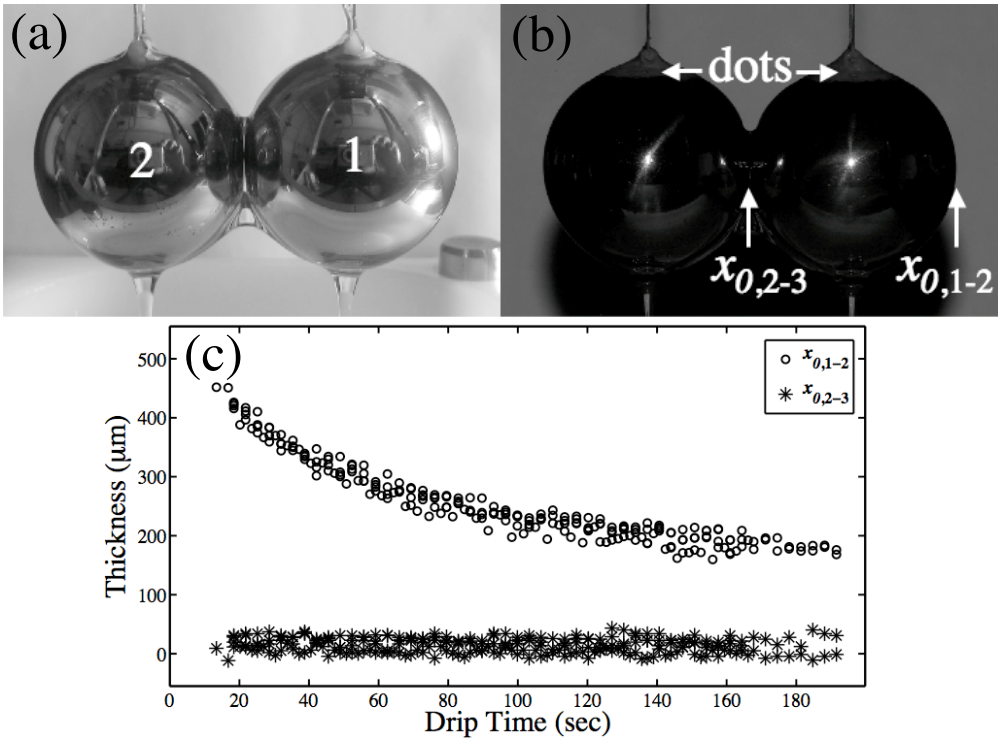

Figure 3.3 (a) Photograph of the target particles during the dripping process and (b) high-contrast snapshot taken with the Pentax high-resolution camera. (c) Plot of the thickness versus time for 5.1 Pa·s oil viscosity and stainless-steel particles.

It is important to note that, when the particles are wetted, the surface tension associated with the liquid bridge pulls the particles together. Therefore, the pendulum arms move a small angle toward one another. Even though this angle is quite small (~0.1°), its influence on the measurement of the oil-layer thicknesses $x_{0,1\text{-}2}$ and $x_{0,2\text{-}3}$ is non-negligible and thus is taken into account when calculating the thicknesses. The error of $x_{0,2\text{-}3}$ measurements is relatively large, considering that a few negative thicknesses are calculated. To verify the measurements of $x_{0,2\text{-}3}$, a small spacer with a known thickness (100 – 315 μm) is placed between the two target particles while they are dry. The thickness of the spacer is calculated using the methods described above and compared to

the known thickness, resulting in an error on the order of 10 μm. Although the error is comparable to the size of $x_{0,2\text{-}3}$, predictions from the model presented later do not qualitatively change when $x_{0,2\text{-}3}$ is set equal to the size of the surface roughness (lower bound of $x_{0,2\text{-}3}$) and when the error of 10 μm has been added to the averaged $x_{0,2\text{-}3}$ (upper bound). Therefore, the error associated with the measurement of $x_{0,2\text{-}3}$ does not change the conclusions of this work.

Once the oil-layer thicknesses are established as described above, the collisional measurements are carried out. Again, the two dry target particles are dipped in the coating bath, and the time at which the collision is carried out is based on the desired oil thickness for that measurement as established previously (for example, using linear fit of the data in Figure 3.3, five seconds before and after the collision time). The striker particle is not coated, but since it is impacting a wet target (particle 2), the collision between the two is wetted – i.e., there is a liquid layer between the particles. The normal, three-body collision is achieved by pulling back along the arc the (dry) striker particle, which is then released and allowed to collide with the two motionless, wetted particles at the bottom of the arc. The striker particle is held by a door attached to a track along the arc. The position of the door can be moved along the track in order to achieve different impacting velocities when released. The door is spring-loaded and is released by a solenoid. Once released, particle 1 collides with particle 2, and particles 2 and 3 travel up the arc. Due to gravity, g, the particles will eventually come back down the arc and collide a second time, etc.; however, data are only taken before and after the first three-body collision, since the liquid-layer thickness for subsequent collisions cannot be determined as accurately as for this first series. Figure 3.4 contains a single snapshot

taken shortly after the collision for two different cases: (a) a smaller impact velocity that leads to a RNC outcome, and (b) a larger impact velocity that leads to a FS state. The corresponding pre- and post-impact velocities are also plotted as functions of time; the details of these measurements are described below.

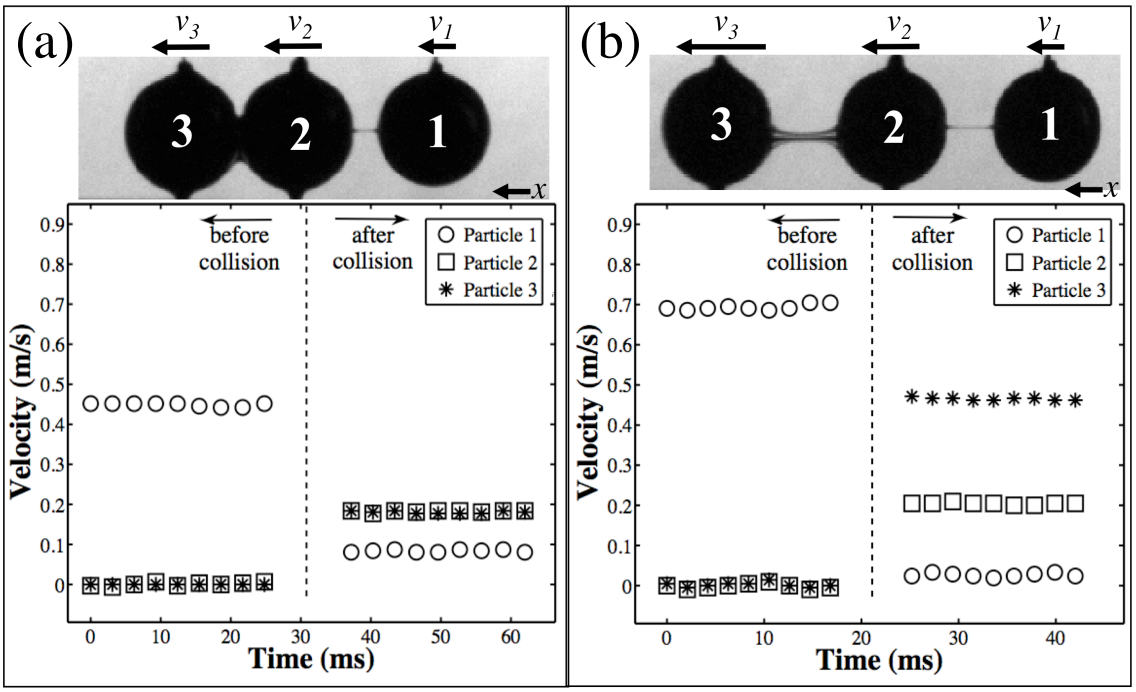

Figure 3.4 Snapshots after collision and corresponding velocity versus time plots for outcomes of (a) RNC and (b) FS using 12 Pa·s oil viscosity and stainless-steel particle material (case lμ_ss_tn in Table 3.2). The initial velocity of particle 1 is from right to left.

The particle positions versus time and, hence, velocities of each particle before and after collision are measured using a high-speed camera. The camera is manufactured by DVC (model 340M) with a 640×480 pixel resolution. To increase the rate of image collection unnecessary border pixels are cropped out. Depending on the exact distance of the camera and velocity of the striker particle, the resulting resolution is approximately

400×50 to 600×150 pixels. Similar to the high-resolution camera, a Navitar 7000 zoom lens is used so that the camera can be placed approximately 1.5 m away from the pendulum apparatus and wide-angle effects are essentially eliminated. The high-speed camera operates at 40MHz and produces a snapshot every 3.1 ms. The series of snapshots is imported into Matlab to find the position of each particle center in each frame. The grayscale frames are converted into black-and-white images, with white particles appearing on a black background. The particle edges are then eroded using a pre-existing function in Matlab, *imerode*, to separate touching particles so they do not appear to be one object in Matlab. The function *regionprops* calculates the centroid of each particle. Five images before and after the collision are used to calculate the pre- and post-collisional velocities, respectively. The frames immediately before and after the collision, however, are not used due to noise resulting from the collision. The velocities are determined by finding the slope of a linear fit of the centroids of the particles versus time for a given set of five images. The error of the velocity measurement is approximately 0.005 m/s. To verify these measurements, collisions between two dry particles were performed and compared to those performed by Stevens and Hrenya [1], in which a different measurement technique was used (light-based gates) to measure pre- and post-collisional velocities. The two methods show excellent agreement.

3.4. Theoretical Development

The ultimate objective for a theory describing three-particle, wetted collisions is twofold: to predict the correct outcomes (FA, RNC, NC, and/or FS) over a range of experimental parameters, and to accurately predict the post-collisional velocity of each

particle. The first objective, which takes the form of a regime map, serves as a good first gauge of the physics incorporated into the theory, while the second objective involves refinement of the important physics identified in the first step. The focus of this work has been on the first objective, since the findings presented below indicate that the physics necessary to predict the outcomes of three-body collisions go beyond that previously reported for two-body collisions. In particular, two physical mechanisms are found to be essential: (i) consideration of the 'excess liquid' from the liquid bridge between the initially-agglomerated, target particles (particles 2 and 3); this excess liquid provides additional resistance as the particles separate after collision, and (ii) consideration of the glass transition (of the oil layer) as a point of rebound due to large lubrication pressures that develop for approaching particles.

To achieve the goal of predicting the correct outcomes, an approximate model is used where a three-body collision is modeled as a series of two-body collisions. First, the striker particle (particle 1 in Figure 3.2) collides with the first target particle (particle 2). Then, the first target collides with the last target particle (particle 3). At this point, particle 1 may 'catch up' with particle 2 and then 2 may strike 3 again, and so on; correspondingly, any subsequent collisions are considered. In each two-particle collision, the collision is assumed to have an initial separation of x_0 and the collision continues until a final separation of x_f is reached or until the relative velocity becomes zero. If the same particles experience any additional collisions, the same initial and final separations are assumed. The justification for using this two-body approximation for purposes of identifying the important underlying physics is twofold: (i) the results of Chapter 2 showed that an analogous approximation predicts well the outcome of three-body

collisions between dry particles, though some quantitative improvement in the prediction of post-collisional velocities is obtained using a three-body treatment, and (ii) in-house, preliminary results for a three-body treatment of wet systems indicate that the more complex treatment leads to modest quantitative changes though does not appreciably change the predicted outcomes (i.e., regime map).

3.4.1. Dimensionless Arguments and Dominant Mechanisms

The first task in the theoretical development is to identify the predominant mechanisms that govern the behavior. Accordingly, the appropriate dimensionless quantities are assessed. The Reynolds number, *Re*, the capillary number, *Ca*, and the particle Stokes number, St_{part}, are calculated for the collisions over the range in the experimental parameter space. As stated in Chapter 1, the relevant dimensionless number for wetted-particle collisions is the Stokes number, $St = mv_0/6\pi\mu a^2$, where $m = m_1m_2/(m_1+m_2)$ is the reduced mass, v_0 is the initial relative velocity, μ is the viscosity, and $a = R_1R_2/(R_1+R_2)$ is the reduced radius where R is the radius of a particle. Here, St_{part} characterizes the particle inertia as it moves through the surrounding air so that the viscosity in *St* is that of the interstitial air. The largest *Re* encountered experimentally is $Re = \rho|v|x/\mu < 0.06$, where ρ is the liquid density, v is the relative velocity of the center of particle masses (i.e. v_1-v_2 or v_2-v_3), and x is the minimum separation distance between the particles. Since the collisions occur with a low *Re*, Stokes flow prevails in the liquid gap. Additionally, the smallest experimental *Ca* (ratio of the viscous force to the capillary force) is $Ca = 3\mu av/\sigma x > 3400$, where σ is the surface tension of the silicon oil

measured to be 2.4 N/m^2. Since the viscous forces dominate, the capillary forces may be neglected. The calculation of *Ca* is based upon the initial relative velocity of the particles. Finally, St_{part} is always much greater than unity; therefore, the surrounding air medium has negligible effect on the collision dynamics.

3.4.2. Dynamics of Two-body Wet Collisions

To describe the Stokes (low-*Re*) flow between spheres dominated by viscous forces, a scaling approach is utilized instead of a formal coupling as carried out by Kantak and Davis [2]. Namely, the hydrodynamic equations for undeformed spheres are solved until a rebound criterion is met, which is based upon a scaling argument. This approximation is used, since the goal here is to obtain qualitative agreement with the regime map rather than refining to achieve quantitative agreement, and a formal coupling between the three bodies introduces considerable complexities (i.e., system of coupled, nonlinear, partial differential equations). The kinematic equations describing the hydrodynamic motion of the two particles during a two-body, wet collision are

$$\frac{dx}{dt} = -v(t) \tag{3.1}$$

and

$$m\frac{dv}{dt} = -F_L(t), \tag{3.2}$$

where $F_L(t)$ is the viscous (lubrication) force resisting the relative motion of the particles in the normal direction. For small deformations and for $x << a$, this force is derived by Kantak and Davis [2] as

$$F_L(t) = \frac{6\pi\mu a^2 v}{x}\left[1 - \frac{x}{x_{\max}}\right]^2, \tag{3.3}$$

where $x_{\max}$ is the maximum thickness of the liquid layer. The expression for the force above is found by integrating the pressure in the gap given by the lubrication equation over only the wetted area of the particle. In previous two-body theories, $x_{\max}$ is assumed equal to the initial separation distance for both the approach and rebound stage, but this is not a good assumption for the three-body collisions considered here, as described below. As the particle significantly penetrates far into the liquid layer ($x << x_{\max}$), the term in the brackets quickly approaches unity and the result for the motion of two immersed spheres moving towards each other is recovered. Using the same assumptions, the absolute pressure in the gap, also derived by Kantak and Davis [2], is

$$p(r,t) = \frac{3\mu a v}{(x + r^2/2a)^2}\left[1 - \left(\frac{x + r^2/2a}{x_{\max}}\right)^2\right] + p_{atm}, \tag{3.4}$$

where r is the distance from the axis connecting the two spheres and p_{atm} is the atmospheric pressure. In this work, the pressure is only tracked in t (of which x is a function); therefore, only the maximum pressure between the particles is considered. Here the maximum pressure occurs at the axis of symmetry ($r = 0$). To solve for the relative velocity and separation distance as functions of time, Equations 3.2 and 3.3 are solved simultaneously using *ode23s* in Matlab, a solver for stiff differential

equations. Note that these equations are used to describe particle motion during the approach phase and rebound phase, if encountered (i.e., if an agglomerate is not formed prior to rebound; agglomeration is detected when the relative velocity is equal to zero during the approach or rebound phase). If the rebound criterion is met upon approach, the particles rebound with the relative velocity reversed and multiplied by the dry restitution coefficient, e_d, to account for the (kinetic) energy dissipation experienced by the particle during deformation. Specifics on the initial conditions and conditions for reversal of relative velocity (i.e., transition from approach to rebound phase) – the rebound criteria – are detailed below.

3.4.3. Effect of Excess Fluid in Liquid Bridge

Upon approach of a given particle pair, the initial separation distance is given by the initial liquid thickness measured using the high-resolution camera described above. The equations above (Equations 3.2 and 3.3) are solved from this point until conditions meet a rebound criterion that will later be described. If the criterion is met, then the particles begin to rebound until they are separated by a final thickness (unless agglomeration occurs beforehand). In previous two-body work [3, 4], the final liquid thickness that the particles encounter upon rebound was assumed equal to the initial (measured) thickness. However, in a three-body collision, the initial target particles (particles 2 and 3 in Figure 3.2) are already in an agglomerated state before the collision. The measured separation distance between particles 2 and 3, $x_{0,2\text{-}3}$ (see Figure 3.3b), characterizes well the 'initial' thickness as the particles are approaching each other, but it does not describe well the final liquid thickness experienced by the particles as they

rebound until they separate. Since particles 2 and 3 are initially agglomerated (i.e., in contact via their common liquid bridge), 'excess' liquid is contained in the bridge (as seen in Figure 3.2a) and serves to fill the widening gap beyond a thickness of $x_{0,2\text{-}3}$ as the particles separate. More specifically, as the particles separate, the excess liquid will flow in the direction of lowest pressure, which occurs along the centerline ($r = 0$). As a result, the excess liquid in the bridge fills the gap between the separating particles, as illustrated by Figure 3.2b. Consequently, the final outbound thickness, $x_{f,2\text{-}3}$, is greater than $x_{0,2\text{-}3}$ and is related to the amount of excess liquid in the bridge.

Since the measurements of the initial thickness between the target particles (particles 2 and 3) are not adequate to describe the rebound phase of the collision, additional steps must be taken to estimate the 'effective' thickness stemming from the excess liquid in the bridge as the particles rebound. The 'effective' thickness is intended to be the separation distance at which the particles escape the resistance of the liquid, and not the rupture distance of the liquid bridge [5-7]. Although a small bridge connecting the particles may be present at distances greater than $x_{f,2\text{-}3}$, a comparison of the liquid bridge in the high-speed video of the collision and the plots of velocity versus time (such as shown in Figure 3.4) indicates that this bridge provides negligible resistance in the final stages prior to rupture since the velocity remains constant while the bridge is still intact. To calculate $x_{f,2\text{-}3}$, the volume of the liquid bridge is divided by the relevant surface area of the particles. In particular, the liquid bridge is approximated as symmetric about the centerline. The shape of the bridge is also approximated to be that of a cylinder (V_{cyl}), minus the volume indented by the spherical shape of the particles (V_{cap}) at the caps of the cylinder. In this way, $x_{excess,2\text{-}3}$ is found by an additional measurement of the height

of the liquid bridge (h in Figure 3.2). The volume of the indented cylinder is then calculated as

$$\begin{aligned} V_{cyl,ind} &= V_{cyl} - 2V_{cap} \\ &= \frac{h^2}{4}\pi\left[2\left(R-\sqrt{R^2-h^2/4}\right)+x_{0,2-3}\right] \\ &-2\left\{\frac{1}{3}\pi\left[3R-\left(R-\sqrt{R^2-h^2/4}\right)\right]\left[\left(R-\sqrt{R^2-h^2/4}\right)\right]^2\right\} \end{aligned} \quad . \tag{3.5}$$

Assuming that the liquid will be evenly dispersed over the caps as the particles separate, the thickness of the (final) liquid layer between the rebounding particles is the volume of the indented cylinder divided by the area of one cap (dividing by the area of both caps, would only give one-half of the thickness), where the area of one cap is given as

$$A_{cap} = 2\pi R\left(R-\sqrt{R^2-h^2/4}\right) \tag{3.6}$$

Accordingly, the liquid-layer thickness upon rebound, when accounting for excess liquid in the bridge, is

$$\begin{aligned} x_{excess,2-3} &= \frac{v_{cyl,ind}}{A_{cap}} \\ &= \frac{1}{6R}\left[h^2-2R\left(R-\sqrt{R^2-h^2/4}\right)=3x_{0,2-3}\left(R-\sqrt{R^2-h^2/4}\right)\right] \end{aligned} \quad . \tag{3.7}$$

The $x_{excess,2\text{-}3}$ value calculated in this manner for the experiments is found to be ~1-2 orders of magnitude larger than $x_{0,2\text{-}3}$. A similar treatment for the final thickness between particles 1 and 2 is not necessary since the particles are not agglomerated prior to collisions (i.e., no pre-existing liquid bridge is present to provide excess liquid upon rebound). Hence, $x_{f,1\text{-}2} = x_{0,1\text{-}2}$ for purposes of model calculation.

The calculation of $x_{excess,2\text{-}3}$ is a critical component of the model, as can be seen from a comparison of the current model (using $x_{f,2\text{-}3} = x_{excess,2\text{-}3}$) with predictions from the same model except without considering the bridge using $x_{f,2\text{-}3} = x_{0,2\text{-}3}$. This treatment of $x_{f,2\text{-}3}$ enters the model in two areas: (i) x_{max} in Equations 3.4 and 3.5 is equal to the largest liquid separation between two particles, so, when considering $x_{f,2\text{-}3} = x_{excess,2\text{-}3}$, x_{max} is also equal to $x_{excess,2\text{-}3}$; and (ii) upon rebound of particles 2 and 3, the differential Equations 3.2 and 3.3 are solved until the separation of the particles reaches $x_{f,2\text{-}3}$. Therefore, if $x_{f,2\text{-}3} = x_{0,2\text{-}3}$, the equations are solved until a much smaller separation distance is achieved than when $x_{f,2\text{-}3} = x_{excess,2\text{-}3}$. To illustrate these concepts, Figure 3.5 is a representative plot of the wet restitution coefficient for each particle pair versus *St*. Here, increasing the impact velocity of the striker particle increases *St,* while all other parameters remain unchanged. The wet restitution coefficient between particles 1 and 2 is a ratio of the final velocities over the initial velocities and is defined as

$$e_{w,1-2} = \frac{v_{f,2} - v_{f,1}}{v_{0,1}}, \tag{3.8}$$

where the subscripts 1 and 2 indicate particles. Similarly, the wet restitution coefficient between particles 2 and 3 is

$$e_{w,2-3} = \frac{v_{f,3} - v_{f,2}}{v_{0,1}}, \tag{3.9}$$

where it is normalized by the initial velocity of particle 1 since the initial velocities of particles 2 and 3 are zero. When $e_{w,1\text{-}2}$ is zero and $e_{w,2\text{-}3}$ is zero, the outcome is FA; for $e_{w,1\text{-}2}$ zero and $e_{w,2\text{-}3}$ non-zero, the outcome is NC; for $e_{w,1\text{-}2}$ non-zero and $e_{w,2\text{-}3}$ zero, the outcome is RNC; finally, when both are non-zero, the outcome is FS. For collisions

between particles that agglomerate, the wet restitution coefficient is zero by definition, and thus the unphysical negative experimental values stem from the error in velocity measurements. In particular, the error in the measurement of the particle velocity propagates to give an error in e_w of approximately 0.02 for low velocities and 0.002 for high velocities. In Figure 3.5a, the thin lines represent the theoretical predictions for $x_{f,2\text{-}3} = x_{0,2\text{-}3}$, and the thick lines represent the predictions for $x_{f,2\text{-}3} = x_{excess,2\text{-}3}$. The vertical arrows pointing to $St_{1\text{-}2}$* and/or $St_{2\text{-}3}$* are also shown, and the associated outcomes on each side of these values are indicated. The theory without the bridge using $x_{f,2\text{-}3} = x_{0,2\text{-}3}$ predicts only two outcomes: FA at lower *St* and NC at higher *St*. In contrast, the current model accounting for the excess bridge fluid predicts three outcomes: FA at low *St*, RNC at intermediate *St*, and FS at high *St*. To test the model, Figure 3.5b shows the corresponding experimental data. Then, the data reveal outcomes of FA, RNC, and FS as *St* increases, in qualitative agreement with the current model and not with the one neglecting the excess bridge fluid. Furthermore, for the model without the bridge using $x_{f,2\text{-}3} = x_{0,2\text{-}3}$, as the velocity of the striker particle increases, the predicted value of $e_{w,2\text{-}3}$ rises rapidly, levels off, and then increases further. The experimental data, on the other hand, indicate that $e_{w,1\text{-}2}$ rises rapidly and then decreases before it levels off, and $e_{w,2\text{-}3}$ increases smoothly past $St_{2\text{-}3}$*. The same behavior in the experimental data is observed for all of the parameters. In contrast, the current model that utilizes $x_{f,2\text{-}3} = x_{excess,2\text{-}3}$ qualitatively predicts the correct outcomes (FA, RNC, FS as *St* increases). Moreover, its features are similar to the experimental results, and the same is true for all of the parameters presented here.

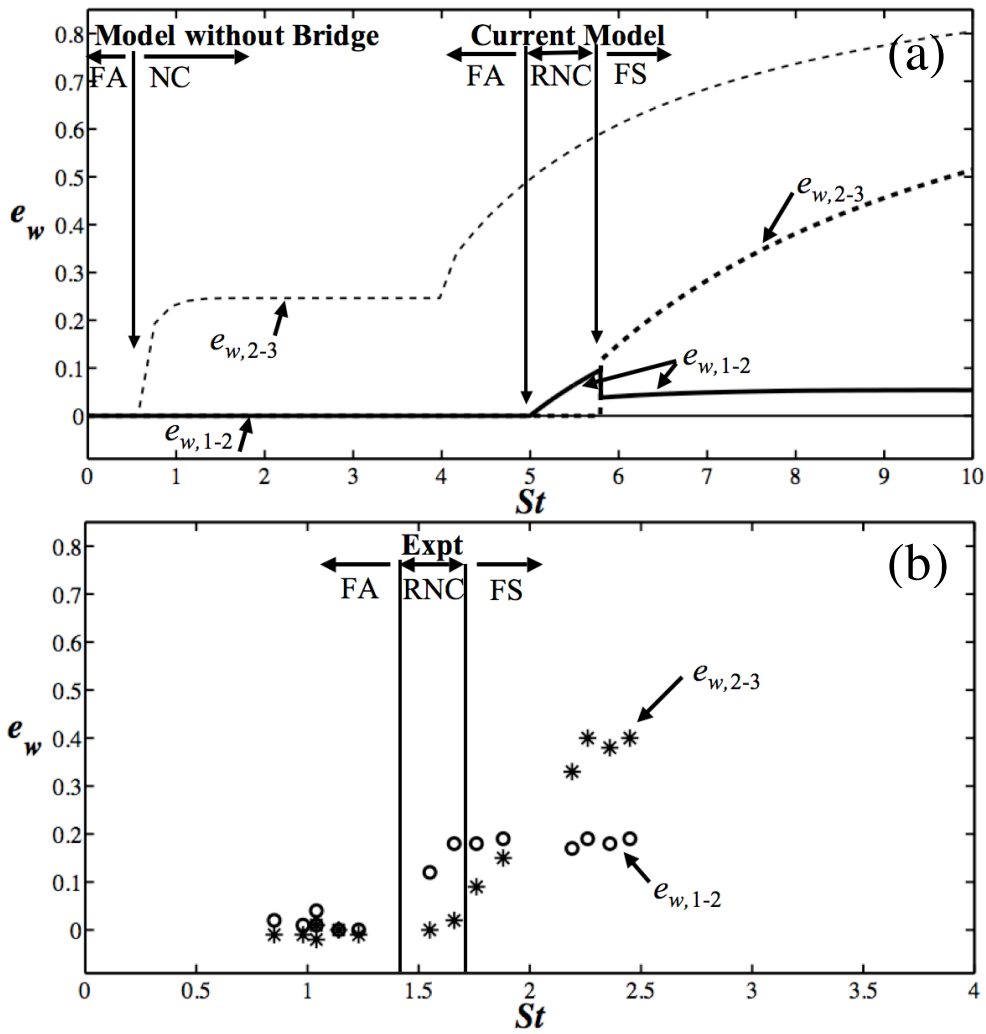

Figure 3.5 Comparisons of (a) theoretical predictions for e_w using the model without the bridge, $x_{f,2\text{-}3} = x_{0,2\text{-}3}$, (thin) and the current model with $x_{f,2\text{-}3} = x_{excess,2\text{-}3}$ (thick), and (b) experimental data using parameters for three-body collisions with 12 Pa·s viscosity oil, chrome-steel particles and thick oil layer (case hμ_cs_tk in Table 3.2). Both models assume that the oil undergoes a glass transition at 5.5×10^8 Pa as a rebound criterion, which is the middle of the range of reported values for silicon oil. Further details about the glass transition are discussed in section 3.4.

It is important to note that the finding demonstrated in Figures 3.5a and 3.5b, namely that accounting for the effect of the excess liquid in the bridge is crucial in obtaining the correct outcomes, does not stem from an (undue) sensitivity to the input

parameters. This concept is illustrated in the regime map of Figure 3.6, which contains a semi-log plot of $x_{f,2\text{-}3}$ versus St. In Figure 3.6, the outcomes (FA, NC, RNC, and/or FS) of the collisions have been calculated according to the current model presented above and all parameters are held constant except the final thickness $x_{f,2\text{-}3}$ and impact velocity (which is proportional to St). The solid lines indicate the border between regions with different outcomes. The calculated points along the lines are indicated by dots. These lines are slightly jagged due to the discrete nature of the calculated outcomes. This feature could be minimized by greater resolution; however, great computational power would be required. The current computational requirements to create a regime map are significant for two reasons: 1) each three-body collision could contain many two-body collisions (some parts of the parameter space require a large number of collisions, for instance, when particles become FA), and 2) the equations are stiff. The dashed lines indicate experimental values of $x_{0,2\text{-}3}$ and $x_{excess,2\text{-}3}$. Consistent with Figure 3.5, more calculations obtained using $x_{f,2\text{-}3} = x_{excess,2\text{-}3}$ predict the ordering of regimes observed experimentally (FA, RNC, FS) whereas predictions obtained using $x_{f,2\text{-}3} = x_{0,2\text{-}3}$ are different (FA, NC). Moreover, it is clear in Figure 3.6 that the erroneous outcomes predicted using $x_{f,2\text{-}3} = x_{0,2\text{-}3}$ do not stem from experimental error, as this value of $x_{f,2\text{-}3}$ is two orders of magnitude smaller than that associated with the correct regimes. Similar to the results depicted in Figures 3.5a and 3.6, results from the rest of the parameter space also point to the need of accounting for the excess liquid in the bridge between the target particles (i.e., $x_{f,2\text{-}3} = x_{excess,2\text{-}3}$).

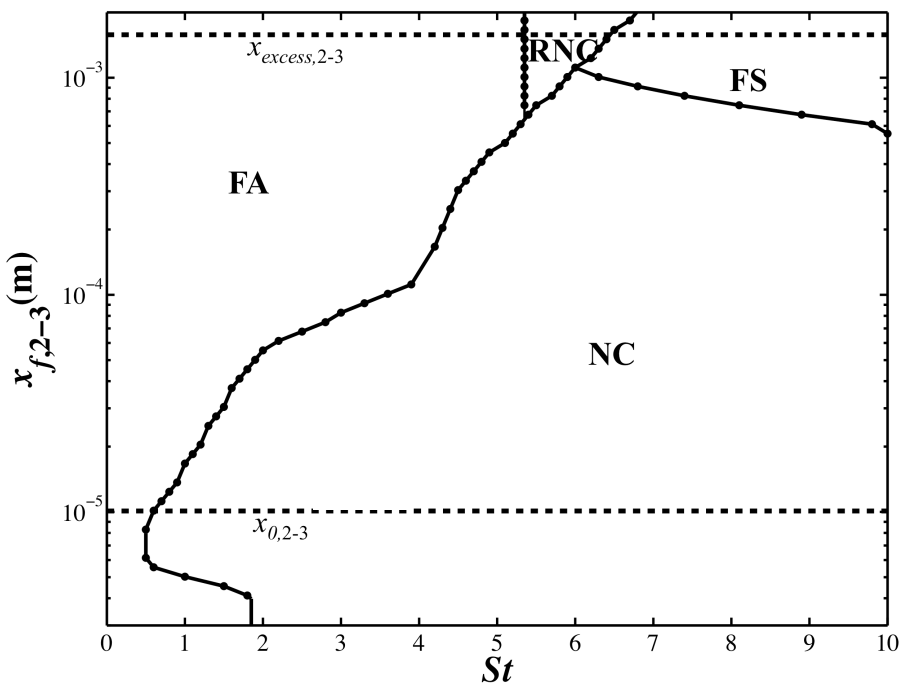

Figure 3.6 Predicted regime map as a function of $x_{f,2\text{-}3}$ and St using parameters for 12 Pa·s oil and chrome-steel particles and thicker initial thickness (corresponding to case hμ_cs_tk in Table 3.2). Dashed horizontal lines represent $x_{f,2\text{-}3} = x_{excess,2\text{-}3}$ and $x_{f,2\text{-}3} = x_{0,2\text{-}3}$. The model assumes that the oil undergoes a glass transition at 5.5×10^{8} Pa.

3.4.4. Pressure-dependent Glass Transition

In addition to the excess liquid in the existing bridge between particles 2 and 3, the effect of the pressure on the properties of the oil in the gap is found to be a critical physical process during the three-body collisions. Note that Barnocky and Davis [8] included pressure dependence in the viscosity of the oil for their work on two-body immersed collisions, though they concluded that its effect was weak for their parameter space. In this work, only the point of glass transition is considered. The glass transition can be viewed as a simplified way to treat a pressure-dependent viscosity, where the viscosity of the oil is equal to the ambient viscosity at pressures lower than the glass-

transition pressure (the pressure at which the silicon oil behaves as a solid), and the viscosity of the oil is infinite at pressures above the glass-transition pressure. For this treatment, the viscosity remains constant throughout the collision process, and rebound will occur if the pressure in the gap reaches the glass-transition pressure. An associated length scale, x_{gt}, can be found by letting $r = 0$ and rearranging Equation 3.5 so that $x = x_{gt}$ when $p = p_{gt}$; therefore,

$$x_{gt} = \sqrt{\frac{3\mu a v x_{\max}^2}{\left(p_{gt} - p_{atm}\right) x_{\max}^2 + 3\mu a v}} \,. \tag{3.10}$$

This criterion for rebound is used in addition to those previously used by Davis *et al.* [3], as described in the next paragraph. In the literature, the glass-transition pressure for silicon oil is reported over a range from 4×10^8 Pa [9] to 7×10^8 Pa [10].

In previous work by Davis *et al.* [3], rebound occurs if one of two conditions is met; namely, the particles have sufficient inertia during the collision to penetrate the liquid layer until their separation decreases to an elastohydrodynamic length scale or to the characteristic roughness of the particles. The elastohydrodynamic length scale for rebound is defined as

$$x_r = \left(3\pi\theta\mu a^{3/2} v_0 / \sqrt{2}\right)^{2/5} \,, \tag{3.11}$$

where v_0 is the initial relative velocity of a given particle-pair collision. Here, θ is calculated from the material properties of the dry particles and is

$$\theta = \frac{2(1-\nu^2)}{\pi E^2} \,. \tag{3.12}$$

The length scale x_r was derived by Davis *et al.* [3] via a scaling argument, which incorporated the effects of lubrication and elastic theories (i.e., elastohydrodynamics). A more formal treatment of elastohydrodynamics (coupling of equations governing lubrication and particle deformation) was utilized by Kantak and Davis [2]. However, since they assume that cavitation occurs upon rebound, no resistance upon rebound is included in their model. As described above in the context of three-particle collisions, it is necessary to have resistance upon the rebound, or else the excess liquid from the pre-existing liquid bridge between the target particles would not affect the dynamics. Without rebound resistance, NC would be predicted as one of the outcomes for the experimental parameters (whereas NC never occurred in the experimental parameter space employed) because the rebound resistance between particles 1 and 2 would be much greater than that between 2 and 3 since $x_{0,1\text{-}2} >> x_{0,2\text{-}3}$ in our experiment. Hence, the approximate model of Davis *et al.* [3] is modified in this effort to include outbound resistance and rebound upon the glass transition. Including the glass transition in the model is an improvement upon Davis *et al.* [3], since it is unphysical for the particles to continue their approach once the glass-transition pressure has been achieved and even higher pressures would be achieved if particles were allowed to continue their approach.

In the model presented here, the differential Equations 3.2 and 3.3 are solved from the initial separation until the particle separation decreases to one of three length scales: (i) x_{gt}, given in Equation 3.11 (ii), x_r, given in Equation 3.12, or (iii) the roughness (bump) size of the particles, x_b. In this work, x_b is assumed to be 1 μm based on previous measurements of similar materials [11]. For the parameter space examined here

(corresponding to the experimental conditions), however, x_{gt} is always encountered before x_r or x_b, and so the glass-transition pressure serves as the criterion for rebound.

Given that the glass-transition criterion is not specific to three-body collisions, it is instructive to first compare the various theories for two-particle collisions, since previous theories have shown reasonable agreement with experimental data. In order to clarify the difference among the theories, Table 3.1 is a summary of the wetted two-body models compared here. The heading 'coupling' refers to the coupling of the hydrodynamics and deformation (i.e., how elastohydrodynamics is accounted for); 'scaling' refers to an approximate coupling through the use of x_r as a rebound criterion (as x_b and x_{gt} do not depend on particle material properties), whereas 'formal' refers to the fully-coupled solution of the lubrication equations and deformation equations. In the current model and the modified model of Davis *et al.* [3], the relative velocity and separation gap are determined using lubrication resistance for undeformed spheres until the gap decreases to the largest of x_r, or x_b [3] or x_{gt}, x_r, or x_b (current model), at which point rebound occurs. In Kantak and Davis [2] the fully-coupled lubrication and elastic deformation equations are solved.

Table 3.1 Two-body wetted model comparisons.

Model	Coupling	Outbound Resistance	Gap at Which Rebound Occurs
Modified Davis *et al.* (2002)[3]	scaling	yes	largest of x_r, x_b
Kantak and Davis (2006)	formal	no	variable
Current Model	scaling	yes	largest of x_{gt}, x_r, x_b

To investigate how well the theories in Table 3.1 perform, Figure 3.7 is two plots of e_w versus St for two-particle collisions with two different viscosities. The wet restitution coefficient for a two-particle collision is defined as

$$e_w = \frac{v_{f,2} - v_{f,1}}{v_{0,1}}, \tag{3.13}$$

where the subscripts 1 and 2 refer to the striker and target particles, respectively. When e_w is zero, the two particles agglomerate, and when e_w is non-zero, the two particles bounce or separate. Here, experimental data obtained from the Stokes's cradle for two-particle collisions (points) are compared to the three theories described above. (In the two-particle implementation of the Stokes's cradle, the striker particle is dry and the single target particle is wetted via the coating bath.) The modified Davis *et al.* [3] model (thin-dashed-dotted) predicts a larger critical Stokes number, St^*, than observed

[3] For a more direct comparison with the current theory, the Davis *et al.* (2002) theory has been modified in three ways: (i) equations 4 and 5 are solved upon approach and rebound, instead of solving the equations of an immersed sphere where the initial separation in multiplied by 2/3 to account for wetting by the finite larger thickness, (ii) x_r directly depends on the relative velocity as a function of time (therefore $x_r = \left(6\pi\theta\mu a^{3/2} v / \sqrt{2}\right)^{2/5}$), and (iii) outbound resistance is included in the model.

experimentally and underpredicts e_w (for non-agglomerated particles) compared to the experimental results. While Kantak and Davis [2] (thick-dashed) does a good job of predicting St^*, it too consistently underpredicts e_w. Kantak and Davis [2] also assumes no resistance on rebound; the inclusion of such resistance would shift their predictions to the right on the plot, resulting in a greater mismatch of St^*. As mentioned previously, outbound resistance is necessary in order to capture the correct outcomes via incorporation of $x_{excess,2\text{-}3}$. Furthermore, the same underpredictions of e_w may be seen when compared to their own experimental data (see Figure 3.7 in original article), since the only experimental data presented used particles with e_{dry} = 0.7 and yet the theory assumes perfectly elastic particles. The current model (solid) includes an assumed glass-transition pressure of 5.5×10^8 Pa, in the middle of the range of the pressures reported in the literature[4]. The current model makes improvements over its modified predecessor [3] in that it predicts a lower St^* and a higher slope of e_w more consistent with the experimental data. Additionally, the current model also offers some quantitative improvements over Kantak and Davis [2] in regions of higher St when the current model exhibits a larger e_w. Nevertheless, the current model is shifted toward higher St than observed experimentally. Thus, quantitative difference may be due to the approximate nature of the model and the possibility that there is only partial resistance during the rebound stage of the experiments (such as would be the case if cavitation occurred but only over a portion of the domain or with a dynamic delay).

---

[4] The overprediction of St^* in two-body collisions by the current model is due to the approximate scaling model employed and the treatment of the glass transition, both of which also lead to an overprediction of $St_{1\text{-}2}^*$ and $St_{2\text{-}3}^*$ in three-body collisions. Therefore, a discussion of the overpredictions can be found below in section 5 with respect to three-body collisions.

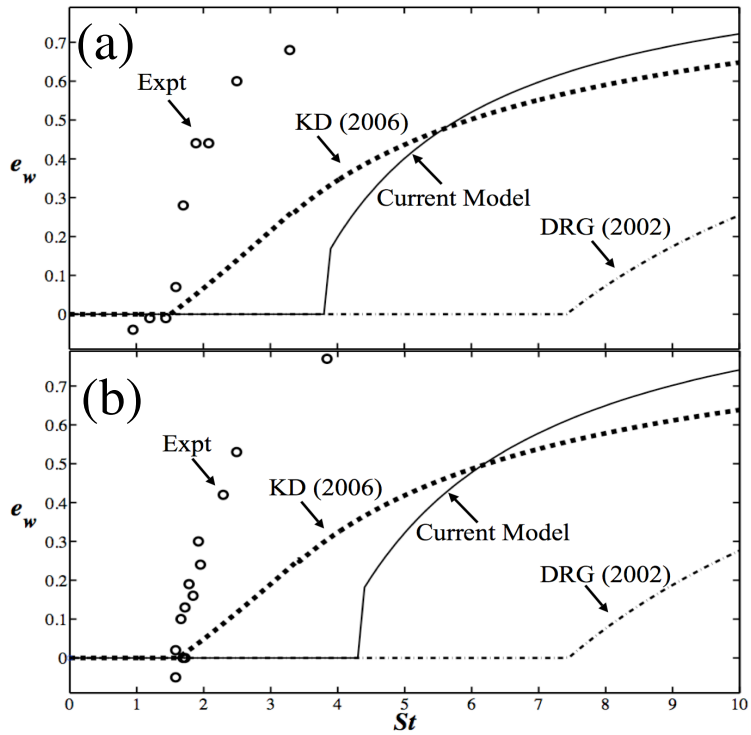

Figure 3.7 Wet restitution coefficient versus Stokes number for wet collisions between two particles with properties of (a) stainless-steel particles, 12 Pa·s viscosity oil, and 294 μm oil thickness and (b) chrome-steel particles, 5.1 Pa·s viscosity oil, and 180 μm oil thickness. Comparisons are presented between experimental results and theories proposed by a modified form of Davis *et al.* [DRG (2002)], Kantak and Davis [KD (2006)], and the current model using a glass-transition pressure of 5.5×10^8 Pa.

The improvement that the inclusion of the glass-transition criterion for rebound makes relative to Davis *et al.* [3] for two-particle collisions is found to be crucial in predicting the correct outcomes of three-body collisions. In Figure 3.8, the three-body collisions are modeled as a series of two-body collisions. The thin lines represent the modified theory of Davis *et al.* [3] without considering the glass transition. The thick lines represent the current theory that includes the condition of rebound at the glass-transition pressure of 5.5×10^8 Pa. The vertical arrows demarcate the outcomes for an easy comparison. As seen in both Figure 3.8a and Figure 3.8b for the two viscosities, the

experimental outcomes observed as *St* increases (for the range of *St* examined) are FA, RNC, and FS, respectively. The predictions using the model of Davis *et al.* [3] produces outcomes of FA and NC for 12 Pa·s, and FA, RNC, NC for 5.1 Pa·s. For the current theory, which has the glass-transition pressure as a rebound condition, the outcomes for 12 Pa·s are in qualitative agreement with experiment. However, the outcomes predicted for 5.1 Pa·s viscosity are FA, RNC, NC and FS, which differ from experimental outcomes since NC was not observed. For the plots using 5.1 Pa·s viscosity, within the region of RNC, $e_{w,1\text{-}2}$ is relatively small, as it is for all 5.1 Pa·s plots presented in this work. Similar to the two-particle collisions (Figure 3.8), the approximate theories overpredict the observed critical Stokes numbers. As mentioned previously, the *Ca* is based upon the *initial* relative velocity of the particles. Because the collisions of particles with 5.1 Pa·s oil have small *final* relative velocities between particles 1 and 2, it is worthwhile to revisit the assumption of neglected capillary forces to determine whether or not the RNC region, which occurs over a very small range of *St*, is still predicted. More specifically, if capillary forces are considered in this region, RNC may not be predicted since particles 1 and 2 would be more likely to agglomerate due to the additional cohesion associated with capillary forces. However, *Ca* is found to still be substantially greater than unity between particles 1 and 2 for *St* within the region where RNC is predicted, when using the final relative velocities of the particles (rather than initial). Therefore, even if capillary forces were considered here, RNC would still be predicted and the predicted progression of outcomes for all parameters explored would remain the same.

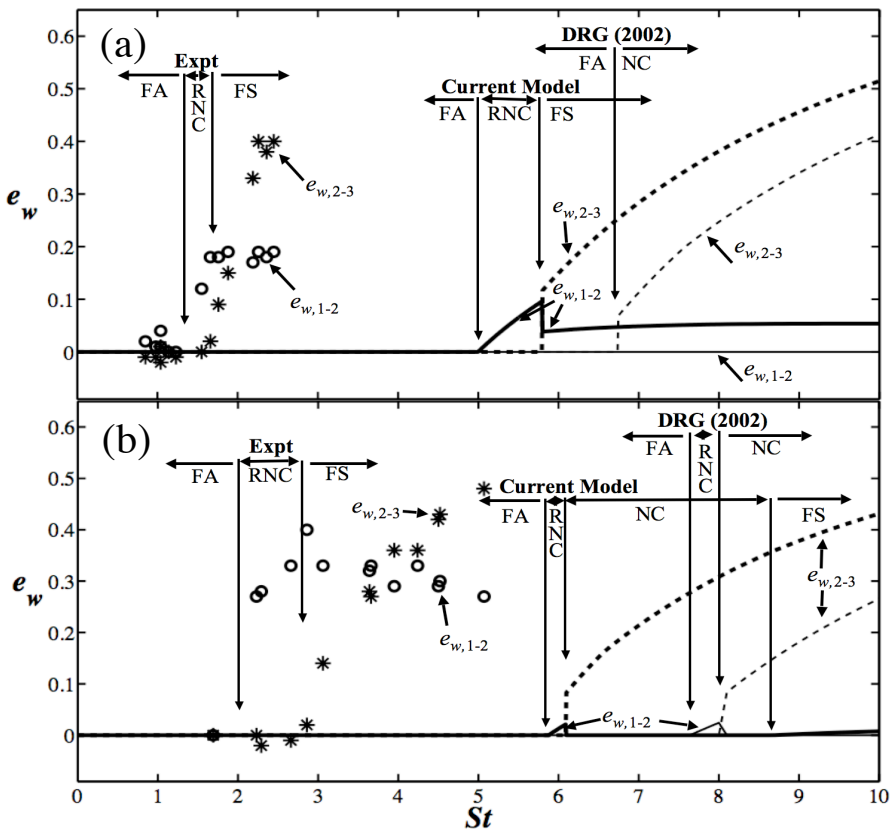

Figure 3.8 Wet restitution coefficient versus Stokes number for normal three-particle collisions with (a) 12 Pa·s oil viscosity and stainless-steel particles (case hμ_cs_tk in Table 3.2), and (b) 5.1 Pa·s oil viscosity and chrome-steel particles (case lμ_ss_tn in Table 3.2). The experimental results are compared against the modified theory of Davis *et al.* [DRG (2002)], represented by the thin lines, and the current model that uses the glass-transition pressure equal to 5.5×10^8 Pa as a rebound point, represented by the thick lines.

To gain insight into the source of the additional predicted outcome (NC) relative to that observed experimentally for 5.1 Pa·s viscosity (Figure 3.8b), a regime map of the predicted outcomes as a function of the glass-transition pressure and *St* is plotted in Figure 3.9. The dashed lines represent the reported glass-transition pressures. In this work, 5.5×10^8 Pa has been used for model predictions, since it is the midpoint of the reported values. However, the regime map (Figure 3.9) clearly indicates that the

predicted outcomes, over this range of glass-transition pressures, are near a transitional point on the regime map. For instance, a glass-transition pressure of 3×10^8 Pa predicts the correct outcomes, which is fairly close to the reported range, especially considering the width of the reported range. Consequently, the experimental/model mismatch does not provide enough evidence of the need for an improvement of the overall physics, only a refinement of the approximations.

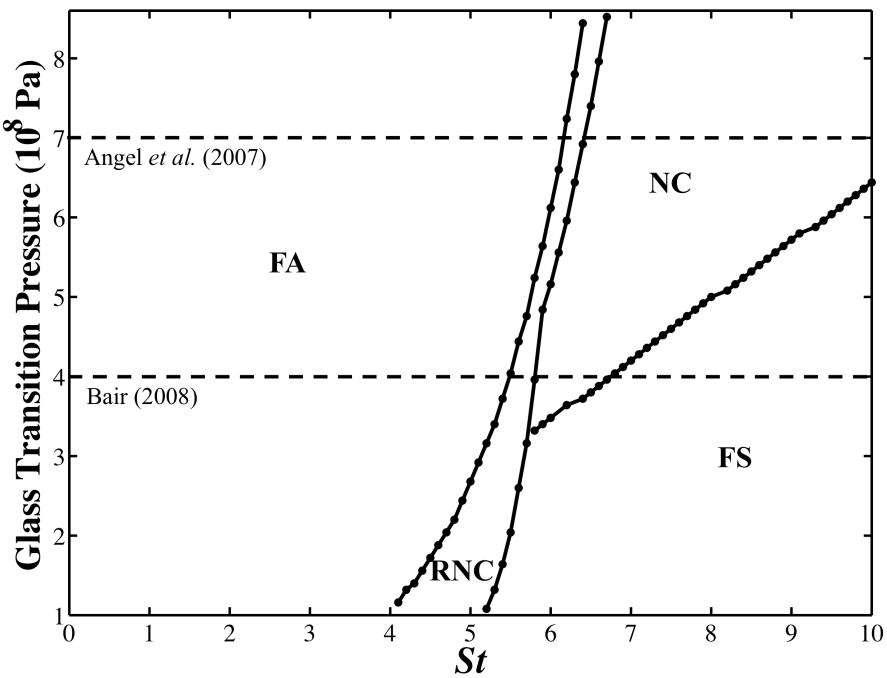

Figure 3.9 Regime map of glass-transition pressure versus *St* for 5.1 Pa·s viscosity oil, chrome-steel particles, and thinner (case lμ_cs_tn in Table 3.2). The dashed lines demarcate the range of the glass-transition pressure for silicon oil that has been reported.

3.4.5. Model Summary

To recap, the theory for three-body collisions that has been developed in this section expands upon the two-body, scaling theory derived by Davis *et al.* [3]. In particular, the position and velocities of the particles are found by considering the three-body collision as a series of two-body collisions and solving the kinematic equations above (Equations 3.2 and 3.3) for each collision. In contrast to previous works, here the value of the maximum liquid-layer thickness, x_{max}, for the collision between the initial agglomerated targets in Equations 3.4 and 3.5 is changed to equal $x_{excess,2\text{-}3}$ due to a pre-existing liquid bridge (not present in two-particle systems). Equations 3.2 and 3.3 are solved with an initial separation equal to the initial (measured) thickness. They are solved for decreasing separation of the sphere noses during the approach stage until one of three rebound criteria is met, two of which were previously explored in Davis *et al.* [3], namely, the separation distance decreases to x_b, x_r or x_{gt}, where surface roughness, elastic deformation, or the glass transition, respectively, becomes important. The additional (third) rebound condition used here is the length scale that incorporates the effects of the glass transition, which for the parameter space explored here, is always encountered before the other two conditions. At the beginning of the rebound stage, the relative velocity is equal to the negative velocity at the time at which the rebound condition was achieved multiplied by e_{dry}. The kinematic equations are again solved until the gap between the particles increases to x_f, at which point separation occurs. For the collision between particles 1 and 2, $x_{f,1\text{-}2}$ remains equal to $x_{0,1\text{-}2}$; between particles 2 and 3, $x_{f,2\text{-}3}$ is now equal to $x_{excess,2\text{-}3}$, since these particles are agglomerated before the collision and their liquid bridge contributes excess liquid to the gap as the spheres separate. If at any

time during this process the relative velocity equals zero, agglomeration occurs and any further integration in time is not required.

3.5. Additional Results and Discussion

Now that the important physics of three-particle collisions have been identified, the objective of the current section is twofold: (i) to further assess the ability of the model to predict the correct progression of outcomes over a wider range of experimental parameters, and (ii) to determine the ability of the model to predict trends in the plot of e_w versus St as experimental parameters are varied. For all cases, model predictions are obtained using the theory described above, namely via an approximation of the three-body collision as a series of two-body collisions, using an effective thickness based upon the excess liquid in the bridge as a final thickness between the target particles, and adding glass-transition effects as a condition of rebound.

With regard to the first objective, a listing of the varied experimental parameters is found in Table 3.2 along with the corresponding outcomes, both experimental and predicted, in order of increasing impact velocity (or, equivalently, increasing St). Parameters that are varied include: oil viscosity, particle material, oil thicknesses (including $x_{0,1\text{-}2}$, $x_{0,2\text{-}3}$ and $x_{excess,2\text{-}3}$), and impact velocity. The notation used to describe each case refers to viscosity, high (hμ) or low (lμ); particle material, chrome steel (cs) or stainless steel (ss); and liquid thickness, thick (tk) or thin (tn). Various oil thicknesses are achieved by varying the drip time (i.e., time to collision after immersion in the coating bath) as illustrated in Figure 3.3c. The particles drip for either 60 (thick) or 120 (thin)

seconds before a collision. The experimental outcomes in all cases are FA, RNC and FS as the impact velocity is increased. For all three-particle collisions involving the higher-viscosity 12 Pa·s silicon oil (cases hμ_cs_tk – hμ_ss_tn), the outcomes predicted are the same as the outcomes observed experimentally. In the collisions involving the lower-viscosity 5.1 Pa·s silicon oil (cases lμ_cs_tk – lμ_ss_tn), the predicted outcomes contain all of the observed outcomes in the correct order, the only difference being that an additional outcome of NC is predicted. However, as described in the section above and illustrated in Figure 3.7, this discrepancy can be explained via the proximity of the predictions to a transitional point on the regime map and uncertainty in previous measurements of the glass-transition pressure, as well as the approximate nature of the scaling theory.

Table 3.2 Experimental parameters for normal, wetted, three-particle collisions. Experimental and predicted outcomes are listed in order of increasing velocity of the striker particle. The possible outcomes are fully agglomerated (FA), Newton's cradle (NC), reverse Newton's cradle (RNC), and fully separated (FS). A glass-transition pressure of 5.5×10^8 Pa is used for all predictions.

case	viscosity (Pa·s)	steel particle material	$x_{0,1\text{-}2}$ (μm)	$x_{0,2\text{-}3}$ (μm)	$x_{excess,2\text{-}3}$ (μm)	impact velocities (m/s)	experimental outcomes	predicted outcomes
hμ_cs_tk	12	chrome	412	10	1534	0.22 – 0.65	FA, RNC, FS	FA, RNC, FS
hμ_cs_tn	12	chrome	310	7	1138	0.23 – 0.83	FA, RNC, FS	FA, RNC, FS
hμ_ss_tk	12	stainless	416	10	1577	0.11 – 1.8	FA, RNC, FS	FA, RNC, FS
hμ_ss_tn	12	stainless	313	7	1155	0.11 – 0.84	FA, RNC, FS	FA, RNC, FS
lμ_cs_tk	5.1	chrome	280	10	1106	0.14 – 0.55	FA, RNC, FS	FA, NC, RNC, FS
lμ_cs_tn	5.1	chrome	202	10	892	0.17 – 0.87	FA, RNC, FS	FA, NC, RNC, FS
lμ_ss_tk	5.1	stainless	295	10	1105	0.11 – 0.40	FA, RNC, FS	FA, NC, RNC, FS
lμ_ss_tn	5.1	stainless	219	10	890	0.19 – 0.51	FA, RNC, FS	FA, NC, RNC, FS

Related to the second objective mentioned above, the theory is able to predict the same trends in $St_{1\text{-}2}$* and $St_{2\text{-}3}$* as the experimental parameters are varied. First, the viscosity of the oil is investigated. To show robustness, Figure 3.10 is a plot of e_w versus St for both (a) chrome steel and (b) stainless steel. The experimental results are shown here as points, but only demarcations of $St_{1\text{-}2}$* for the current model are shown for a qualitative comparison. As the viscosity is increased, the experimental results for both $St_{1\text{-}2}$* and $St_{2\text{-}3}$* decrease (i.e., the particles have a larger tendency to rebound for a given St). As shown, the model is in qualitative agreement with these trends. Observing smaller $St_{1\text{-}2}$* and $St_{2\text{-}3}$* with larger viscosity may at first seem counterintuitive, since a high viscosity implies a 'stickier' collision. In particular, if e_w is plotted against the dimensional impact velocity instead of the dimensionless St, the lower-viscosity oil would experience a transition from FA to RNC at a smaller impact velocity; therefore, in practice, as viscosity is increased the collision is indeed 'stickier' and separation occurs at higher impact velocities. The predicted trend can be traced to the rebound criteria contained in the model. In previous modeling of two-body collisions by Ennis *et al.* [4], the only rebound criterion used was surface roughness (x_b), and e_w was related to the parameters by

$$e_w = \begin{cases} 0 & , \quad St < St_c \\ e_d(1 - St_c / St), & St > St_c \end{cases} \tag{3.14}$$

and

$$St_c = \frac{1}{e_d} \ln\left(\frac{x_b}{x_0}\right). \tag{3.15}$$

Notice that St^* has no dependence on the viscosity, which is contrary to the data contained in Figure 3.10. In contrast, for the work by Kantak and Davis [2], elastohydrodynamics correctly predicts the decrease in St^* for two particles with increasing viscosity. In their work, the trend stems from the fact that as the pressure increases the particles deform more, leading to a greater storage of energy to be released. Therefore, since the pressure increases more with a larger oil viscosity, there is more deformation of the particles, and the collision has a smaller St^* with larger viscosity. Similarly, this physical process is accounted for in the scaling analysis by Davis *et al.* [3] since, in Equation 3.11 and 3.12, x_r depends on the solid-particle properties, namely E and ν. In the current model, the correct trends are predicted even though the x_r does not serve as the rebound length scale. Instead, the glass-transition length scale, x_{gt}, prevails. Accordingly, the point of rebound is only dependent upon the pressure between the particles, not the solid-particle properties. Therefore, in this work the mechanism for the observed trend with viscosity does not arise from elastohydrodynamic theory, but rather from the relation between pressure and viscosity. As seen in Equation 3.4, the pressure is proportional to viscosity, and so a higher pressure is achieved with a higher viscosity. Therefore, rebound at the glass-transition pressure can be achieved at a larger separation distance with a high viscosity. This result can be also seen in Equation 3.10, where x_{gt} increases as the viscosity increases.

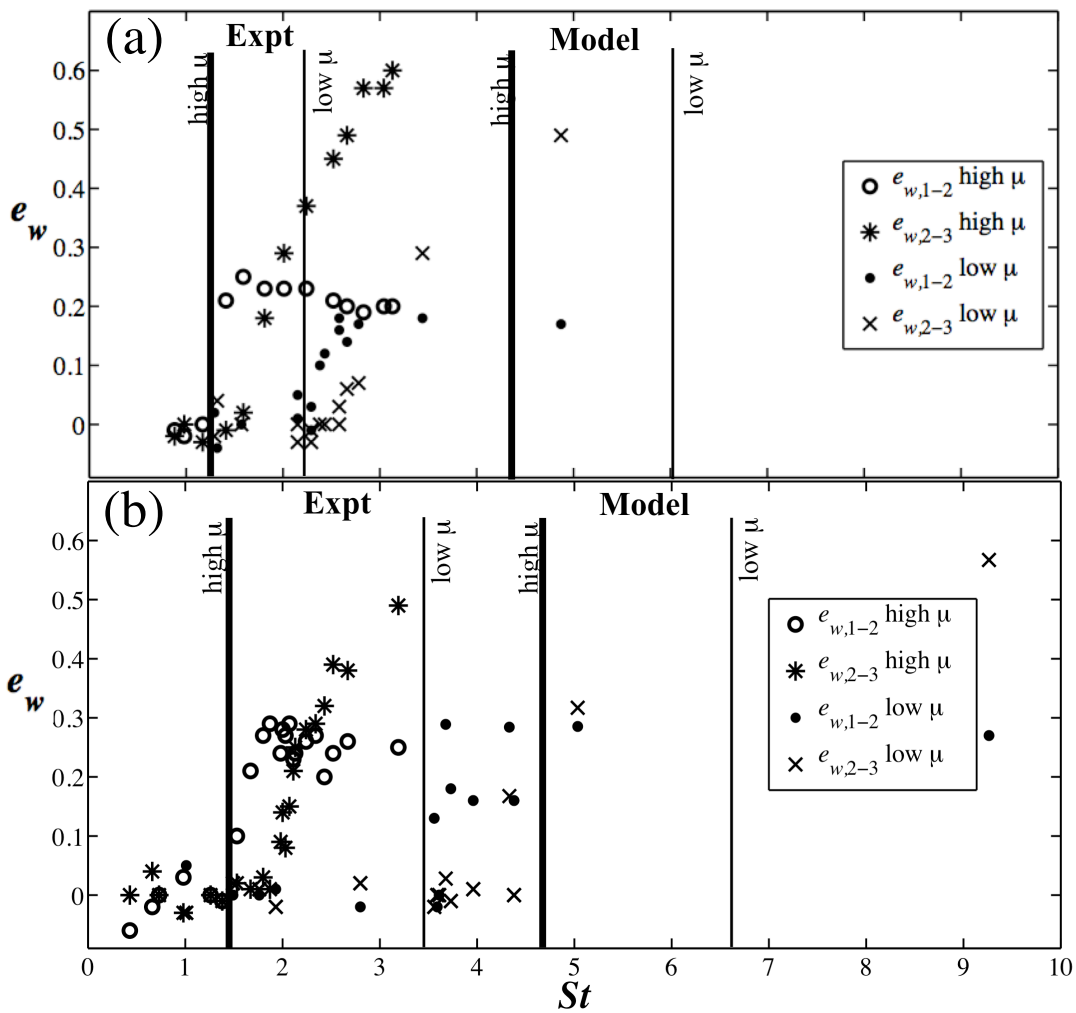

Figure 3.10 Effect of oil viscosity on the wet restitution coefficient for (a) chrome steel and thicker liquid layer (cases hμ_cs_tk and lμ_cs_tk), and (b) stainless steel and thinner liquid layer (cases hμ_ss_tn and lμ_ss_tn). The vertical solid lines demarcate $St_{1\text{-}2}$* and show that this critical value for rebound shifts to higher values for both theory and experiment as the viscosity is decreased.

Although the glass transition is not dependent upon the solid-particle properties, these properties do have an impact on the dynamics of the collision upon velocity reversal (via particle deformation). In particular, the influence of the dry restitution coefficient is demonstrated in Figure 3.11, where viscosity and all thicknesses are held

constant while varying the two different types of particle material, chrome steel (e_d = 0.99) and stainless steel (e_d = 0.90). Both the experiment and theory agree that, as the dry restitution coefficient increases, $St_{1\text{-}2}$* and $St_{2\text{-}3}$* decrease and $e_{w,1\text{-}2}$ and $e_{w,2\text{-}3}$ increase. As expected, the softer particles will experience a greater energy loss during collisions, and thus are more likely to agglomerate. In the theory, upon rebound, the particles have a relative velocity equal to the negative of the relative velocity when the rebound criterion is met, multiplied by e_{dry}. Therefore, after a collision between two particles, a smaller e_{dry} results in a smaller relative velocity and thus a smaller e_w. Nonetheless, since the difference in the dry restitution coefficients between the two particle materials is small, the shift seen is also small. Here, e_{dry} refers to the dry restitution coefficient between two steel particles, since measurements are not available between steel and solid silicon oil. As seen from Figure 3.11, this approximation is able to capture the appropriate trends between harder and softer particles.

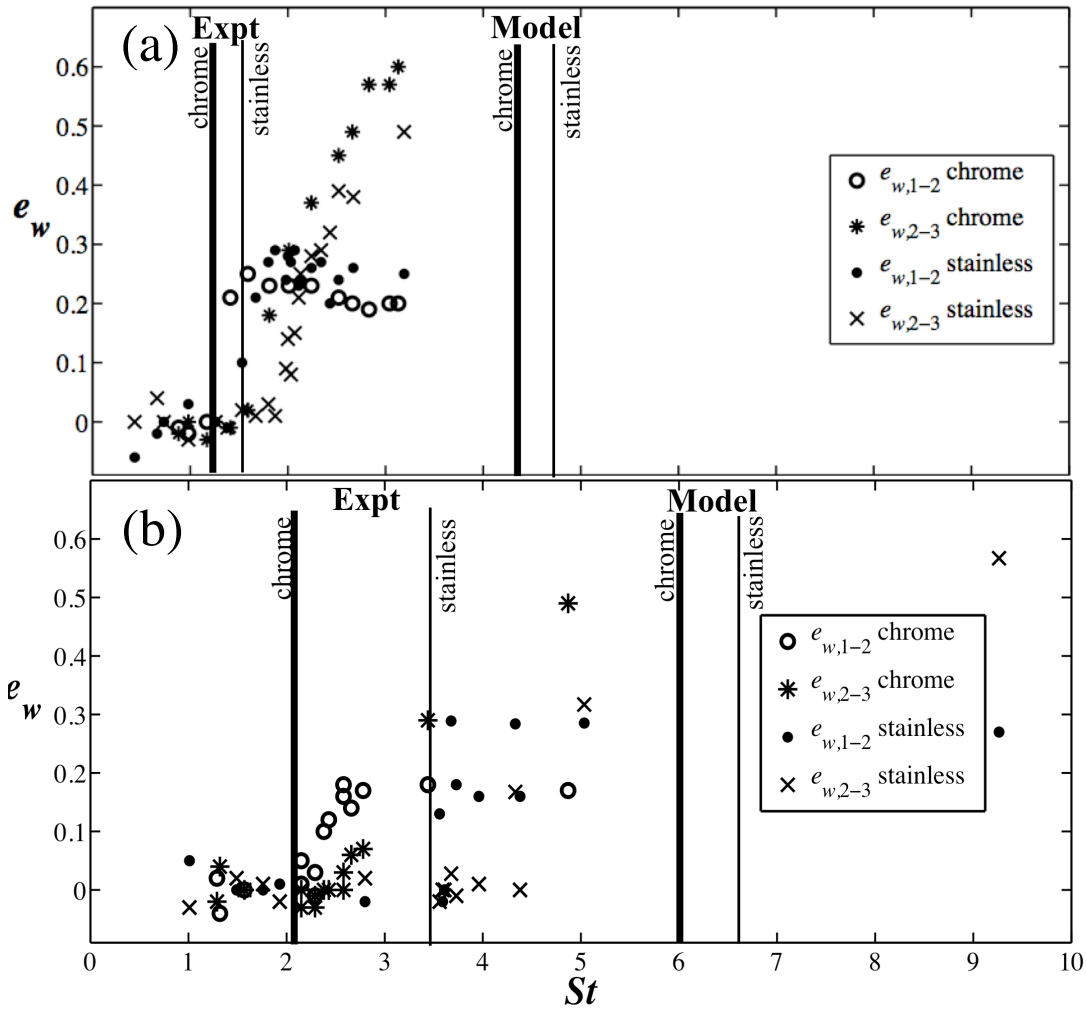

Figure 3.11 Effect of particle material on the wet restitution coefficient with (a) 12 Pa·s and thicker liquid layer (cases hμ_cs_tk and hμ_ss_tk), and (b) 5.1 Pa·s and thinner liquid layer (cases lμ_cs_tn and lμ_ss_tn). The vertical solid lines demarcate $St_{1\text{-}2}$* and show this critical value for rebound shifts to higher values for both theory and experiment as the dry restitution coefficient is decreased.

Finally, in Figure 3.12, the effect of the liquid-layer thickness on e_w is illustrated. Different liquid-layer thicknesses are achieved by allowing the target particles to drip for a longer period of time. Consequently, all three liquid thicknesses are smaller when the particles are allowed to drip for a longer time. In both Figure 3.12a and Figure 3.12b, a

qualitative agreement exists between experiment and theory, and a thinner oil layer has a lower $St_{1\text{-}2}$* and $St_{2\text{-}3}$* , and a higher $e_{w,1\text{-}2}$ and $e_{w,2\text{-}3}$. With a thinner oil layer, the particles have a smaller distance to travel during approach to meet a rebound criterion (since none of the rebound criteria depend on oil thickness), and they have a smaller final distance to travel during rebound to become separated. In other words, the resistance to particle motion is decreased, and agglomeration is less likely.

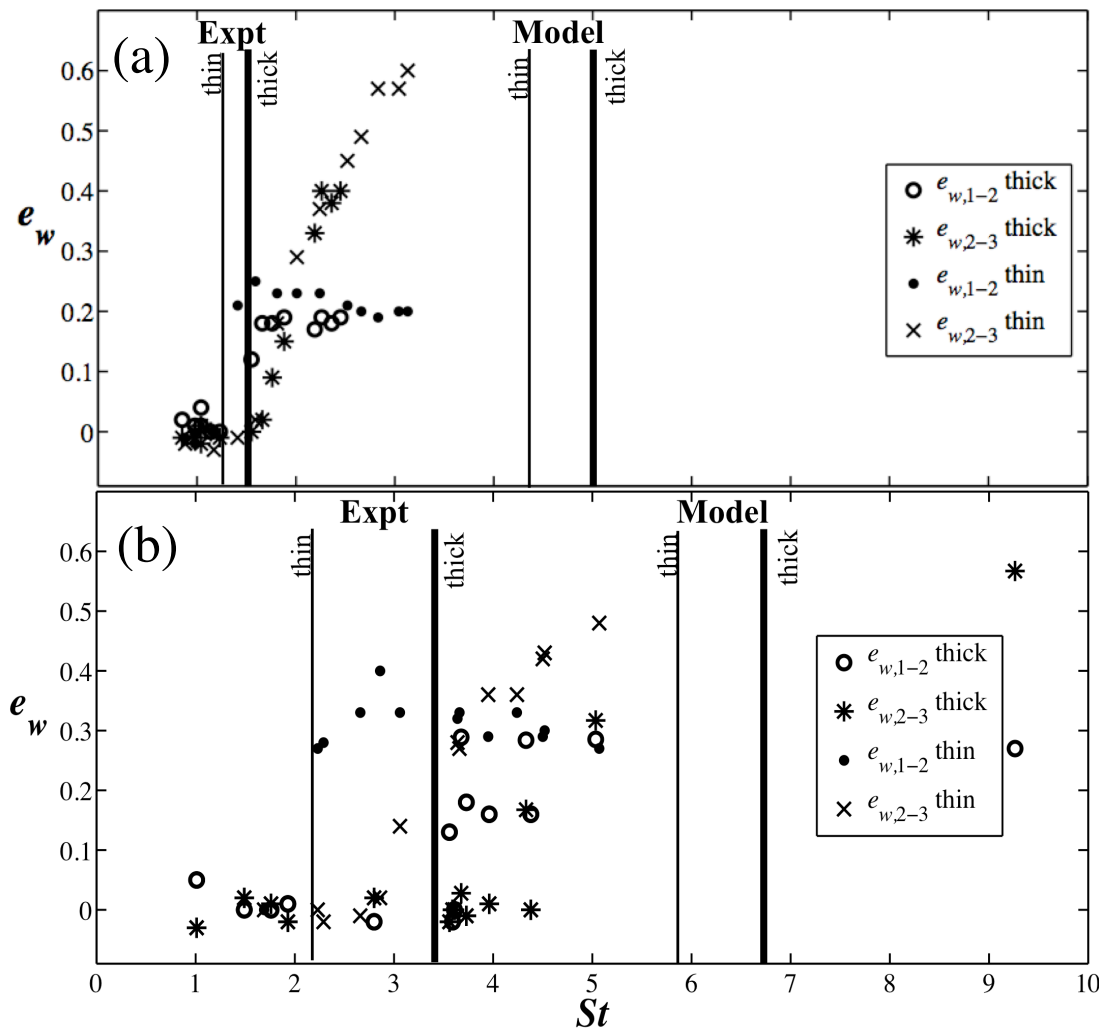

Figure 3.12 Effect of oil thickness on the wet restitution coefficient for (a) 12 Pa·s oil viscosity, chrome steel (cases hμ_cs_tk and hμ_cs_tn), and (b) 5.1 Pa·s, stainless steel (cases lμ_ss_tk and lμ_ss_tn). The vertical solid lines demarcate $St_{1\text{-}2}$* and show that this critical value for rebound shifts to lower values for both theory and experiment as liquid-layer thickness is decreased.

3.6. Summary

Unlike previous efforts on collisions between wetted particles (particles with a thin coating of viscous liquid), which focused on two-body systems, the focus of this work is on the dynamics of three-body, wetted collisions. Here, normal or head-on collisions are considered, in which four outcomes are geometrically possible, unlike two-particle collisions in which only two outcomes are possible. To better understand the

underlying physics of this three-body system, a combination of experiments and lubrication (low-Reynolds number) theory is used.

The experiments are carried out with a Stokes's cradle, which is an apparatus inspired by the desktop toy known as the Newton's cradle. Unlike the Newton's cradle, however, the particles in the Stokes's cradle are wetted prior to collision. Measurements of the liquid-coating thickness and pre- and post-collisional velocities were made using a high-resolution camera and a high-speed camera, respectively. Parameters varied include the oil viscosity, particle material, thicknesses of the oil layer, and the impact velocity. In this work, only outcomes of FA (fully agglomerated), RNC (reverse Newton's cradle) and FS (fully separated) were observed. Surprisingly, the outcome most commonly associated with the desktop toy, NC, proved to be elusive for the conditions investigated. More detail on how investigation of the regime maps lead to experimental realization of NC can be found in Chapter 3.

Comparisons of the experimental results are made against theory that approximates the three-particle collision as a series of two-particle collisions. The objective of the modeling is to achieve qualitative agreement with experimental data in order to identify the dominant physical mechanisms at play during the collision. One evaluation of the qualitative results is made by comparing the experimental outcomes with the predicted outcomes. Previous models for wetted, two-body collisions, which assume Stokes flow (low-*Re*) and particle deformation, do not result in the correct outcomes for three-body systems, and a regime map of the parameters reveals that the mismatch does not result from a (realistic) sensitivity to the input parameters. Accordingly, a scaling model has been developed here that has two key differences from

previous two-body models. First, in a three-particle collision, since the initially agglomerated target particles have a liquid bridge that contains a large amount of 'excess' liquid (not found in a two-particle collision), an effective thickness based upon the excess liquid that fills in the gap between the particles as they separate must be incorporated. Second, unlike most previous two-body theories [2-4, 12], a rebound criterion has been developed which ensures rebound as the pressure between the particles reaches the glass-transition pressure (pressure at which the oil behaves as a solid). A good model/experimental qualitative agreement for the outcomes (i.e. FA, RNC, FS) is found when the above physics are taken into consideration.

In addition to predicting the outcomes, the proposed theory also predicts the qualitative trends in $St_{1\text{-}2}$* and $St_{2\text{-}3}$* as experimental parameters are varied. Most notably, as the viscosity of the oil is increased, $St_{1\text{-}2}$* and $St_{2\text{-}3}$* decrease. Unlike in previous two-body theories, where the same trend arose from elastohydrodynamics, here the glass transition is the source of this behavior. Namely, since the pressure between the particles increases with viscosity (Equation 3.4), higher pressure is obtained with higher viscosity oil. Therefore, the glass-transition pressure is reached at larger separation distances with higher-viscosity oil.

Due to the predicted outcomes and trends showing qualitative agreement with the experiments, the important physical processes have been identified. The scaling analysis used is ideal for this process because it helps to quickly identify any gross mismatches without a comprehensive computational effort. An improved model is required for a more accurate quantitative match, and this can be achieved by refinement upon two approximations: (i) simultaneous treatment of the three-body collision rather than the

series of two-particle collisions, which is expected to be particularly important for wet collisions since lubrication forces act simultaneously on both sides of the middle particle; and (ii) a strict comprehensive coupling of the hydrodynamic (which includes a pressure-dependent viscosity, stiff in nature) and the elastic theories. For a complete model of collisions occurring in practice, oblique collisions will also need to be considered.

Literature Cited

1. Hrenya, C.M. and A.B. Stevens. Comparison of soft-sphere models to measurements of collision properties during normal impacts. *Powder Technology* **154**, 99-109, (2005).
2. Kantak, A.A. and R.H. Davis. Elastohydrodynamic theory for wet oblique collisions. *Powder Technology* **168**, 42-52, (2006).
3. Davis, R.H., D.A. Rager, and B.T. Good. Elastohydrodynamic rebound of spheres from coated surfaces. *Journal of Fluid Mechanics* **468**, 107-119, (2002).
4. Ennis, B.J., G. Tardos, and R. Pfeffer. A Microlevel-Based Characterization of Granulation Phenomena. *Powder Technology* **65**, 257-272, (1991).
5. Lian, G.P., C. Thornton, and M.J. Adams. A Theoretical-Study of the Liquid Bridge Forces between 2 Rigid Spherical Bodies. *Journal of colloid and interface science* **161**, 138-147, (1993).
6. Mikami, T., H. Kamiya, and M. Horio. Numerical simulation of cohesive powder behavior in a fluidized bed. *Chemical Engineering Science* **53**, 1927-1940, (1998).
7. Pepin, X., D. Rossetti, S.M. Iveson, and S.J.R. Simons. Modeling the evolution and rupture of pendular liquid bridges in the presence of large wetting hysteresis. *Journal of colloid and interface science* **232**, 289-297, (2000).
8. Barnocky, G. and R.H. Davis. The Influence of Pressure-Dependent Density and Viscosity on the Elastohydrodynamic Collision and Rebound of 2 Spheres. *Journal of Fluid Mechanics* **209**, 501-519, (1989).
9. Bair, S. *Unpublished*, (2008).
10. Angel, R.J., M. Bujak, J. Zhao, G.D. Gatta, and S.D. Jacobsen. Effective hydrostatic limits of pressure media for high-pressure crystallographic studies. *Journal of Applied Crystallography* **40**, 26-32, (2007).
11. Barnocky, G. and R.H. Davis. Elastohydrodynamic Collision and Rebound of Spheres - Experimental-Verification. *Physics of Fluids* **31**, 1324-1329, (1988).
12. Davis, R.H., J.M. Serayssol, and E.J. Hinch. The Elastohydrodynamic Collision of 2 Spheres. *Journal of Fluid Mechanics* **163**, 479-497, (1986).

4. STOKES'S CRADLE: INFLUENCE OF LIQUID BRIDGE VOLUME ON THE NORMAL COLLISIONS OF THREE WETTED PARTICLES[5]

4.1. Abstract

In this work, three-body collisions between liquid-coated spheres are investigated experimentally using a 'Stokes's cradle', which resembles the popular desktop toy known as the Newton's cradle. Surprisingly, previous work indicates that every possible outcome was observed in the wetted system except the traditional Newton's cradle (NC) outcome. Here, NC is achieved experimentally via guidance from a first-principles model, which revealed that controlling the volume of the liquid bridge connecting the two target particles is the key parameter in attaining the NC outcome. By independently decreasing the volume of the liquid bridge, not only NC is achieved, but also several new findings are uncovered. For example, in contrast to previous work on two-body collisions, three-body experiments provide direct evidence that the fluid resistance upon rebound cannot be completely neglected due to presumed cavitation; this resistance also plays a role in two-body systems yet cannot be isolated experimentally in such systems. The herein micro-level description provides an essential foundation for macro-level descriptions of wetted granular flows.

---

[5] Donahue, C.M., C.M. Hrenya, and R.H. Davis, *Stokes's Cradle: Newton's Cradle with Liquid Coating.* Physical Review Letters, 2010. **105**(3): p. 34501.

4.2. Introduction

Newton's cradle has long been a popular desktop toy. The outcome is well-known: when a solid sphere at the end of a line of dry, suspended spheres is pulled up the arc and released, it falls and strikes the adjacent sphere, causing the sphere on the opposite end to be ejected from the group. In the previous Chapter, it was noted that every possible outcome was observed experimentally in Stokes's cradle (i.e., the wetted version of Newton's cradle) except the traditional Newton's cradle (NC) outcome. Here, the NC outcome is experimentally achieved via guidance from theory, which reveals that controlling the liquid bridge volume connecting the two target particles is key in attaining the NC outcome.

Additionally, by controlling the liquid bridge volume, the effect of the outbound resistance can be isolated from the inbound resistance. Previous works indicate that the pressure upon rebound is significantly below the vapor pressure, leading to a presumption of the onset of cavitation, and thus an assumption of negligible resistance upon *rebound* [1, 2]. However, it is difficult to experimentally isolate the role of cavitation in two-body systems, since a change in the resistance upon rebound (e.g., via a change in viscosity or thickness of the liquid layer) will also result in a change in the resistance upon *approach*. The three-body experiments described in this Chapter provide direct evidence that the fluid resistance upon rebound cannot be completely neglected due to presumed cavitation.

4.3. Experimental Methods

Unlike the Newton's cradle toy, which typically has five dry spheres in a row, our focus is on a wetted, three-sphere system as illustrated in Figure 4.1. Consequently, compared to two-body collisions, where the possible outcomes only include stick or bounce, four outcomes are possible in a three-sphere collision. In addition to the Newton's cradle (NC) outcome (where the sphere opposite the striker sphere separates from the remaining agglomerate), the other possibilities include fully agglomerated (FA, where all spheres stick together), 'reverse Newton's cradle' (RNC, where the striker sphere separates but the other spheres stay agglomerated), and fully separated (FS). Thus, both agglomeration and de-agglomeration may be studied. Figure 4.2 shows representative experimental snapshots of the spheres after the collision for 12.0 Pa·s oil, chrome-steel spheres, and dripping for 60 s before collisions ('thick' liquid layer). Here, all parameters are kept constant between the subfigures, except for impact velocity, in which the arrow size represents the relative magnitude. The outcomes as velocity is increased are FA, RNC, and FS, and do not include the NC outcome, which is counter-intuitive given our experience with the toy. In our companion work [3], a new first-principles model is presented that is able to predict the correct progression of outcomes shown in Figure 4.2, including the consistent absence of NC. To date, no other group has published findings on the collisional dynamics between more than two wetted bodies.

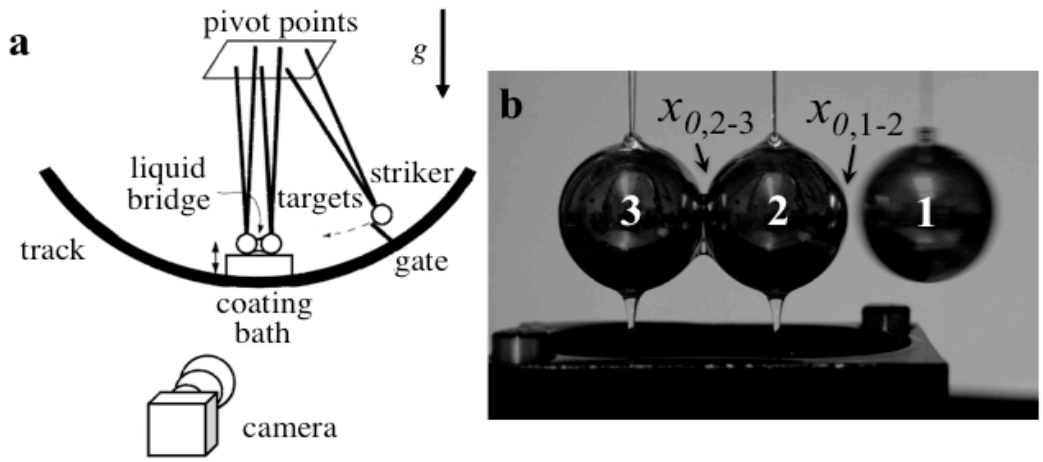

Figure 4.1 Experimental set-up (a) schematic and (b) photograph. For more details, see Chapter 3.

In the current effort, the previously elusive NC outcome is attained by using the aforementioned model to generate an array of regime maps that identify where in the parameter space the NC outcome is expected. Furthermore, this work has shown that the outbound resistance plays a critical role in the collisional outcome. A modified experimental method employed here has allowed us to independently change $x_{f,2\text{-}3}$ by adjusting the liquid-bridge volume while leaving $x_{0,1\text{-}2}$ and $x_{0,2\text{-}3}$ fixed (note that $x_{f,1\text{-}2} = x_{0,1\text{-}2}$, since there is no liquid bridge for the 1-2 pair). This isolation of outbound-resistance effects, which cannot be accomplished in two-body experiments, is detailed below. Moreover, new, counter-intuitive experimental results emerge in this effort, such as producing 'stickier' collisions with a thinner liquid layer. The model again provides the physical insight to explain these behaviors. Hence, the following offers a model overview, followed by experimental results that have led to several findings that did not manifest in previous two- or three-body collisions.

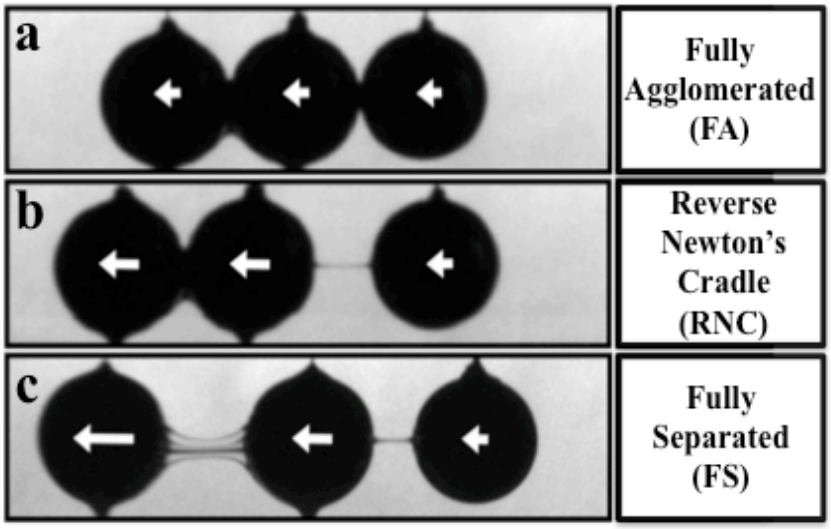

Figure 4.2 Snapshots after a collision using 12.0 Pa·s oil, chrome-steel spheres, and 60 s drip time ($x_{0,1\text{-}2}$= 410 μm, $x_{0,2\text{-}3}$= 14 μm). (a) FA is observed at low velocities, (b) RNC at moderate velocities, and (c) FS at high velocities. Unexpectedly, NC was not initially observed over the wide range of parameters varied.

4.4. Model Description

To better understand the absence of the NC outcome in our initial experiments, a first-principles model is utilized. The three-sphere collision present in the experiments is approximated as a series of two-sphere collisions in the model. The striker sphere (sphere 1 in Figure 4.2) collides with the first target sphere (sphere 2), which subsequently collides with the last target sphere (sphere 3). At this point, the striker sphere may 'catch up' and collide again with the first target sphere, which may then collide again with the second target sphere, etc.; if so, the subsequent collisions are also included in the analysis. However, the current work does not include later collisions after the target spheres reach the end of their arcs and reverse direction due to gravity. This two-body interaction sequence is pursued because our work is focused on identifying the dominating physical mechanisms, and preliminary results show only small quantitative

differences when a three-body model is employed. Furthermore, future work will consider dynamic simulations of many-sphere systems. Hard-sphere models, which account for only two spheres colliding at a time, require far less computational power than their soft-sphere (multi-contact) counterparts and have been shown to successfully simulate cohesive-particle flows that involve contacts and agglomerates of more than two spheres [4, 5].

The model used in this Chapter and in Chapter 3 extends previous models [1, 6] of wetted collisions between only *two* spheres, with two important distinctions detailed later. An analysis of the appropriate dimensionless numbers indicates that Stokes flow prevails (low-Reynolds number, $Re = \rho|v|x/\mu < 0.06$) and that capillary forces may be neglected (high capillary number, $Ca = 3\mu a|v|/\sigma x > 3400$) in the experiments. Here, ρ is fluid density, v is relative velocity of the two spheres, x is separation distance between the surfaces of the two spheres, μ is fluid viscosity, $a = R_1R_2/(R_1 + R_2)$ is reduced radius of the spheres where R is the radius, and σ is surface tension. Air resistance is neglected. The relevant equations of motion for two wetted spheres are provided in our previous work [3] and contain no fitting parameters. As two spheres approach, they (i) experience resistance starting at the separation x_0 due to lubrication during approach, (ii) may reach a minimum separation and reverse direction due to one of three criteria, and (iii) experience resistance upon rebound until the separation reaches x_f. Agglomeration occurs if the initial momentum is not great enough to overcome the total resistance from lubrication. Alternatively, rebound past x_f may occur if the initial momentum is large enough that a portion of the kinetic energy becomes stored as elastic deformation rather than lost to viscous dissipation. However, rebound of sphere 1 from 2 occurs more easily than 2

from 3, because of the additional resistance from the excess fluid associated with the liquid bridge (see Figure 4.1b) between 2 and 3, leading to a bias for the RNC versus NC outcome. The rebound criteria include surface roughness (a measurable quantity of dry sphere) and the elasticity length scale (derived previously from elastohydrodynamic theory [1, 6]). Unlike existing two-sphere models [1, 6], included are (i) the glass-transition length scale as an additional rebound criteria, and (ii) outbound resistance, which was previously neglected due to assumed cavitation. Specifically, the glass-transition length scale is derived by assuming the oil viscosity remains at atmospheric-pressure viscosity until the glass-transition pressure of the oil is achieved. Moreover, the increased resistance will cause the collisions to become stickier, particularly between the target spheres (2 and 3), where the outbound resistance is large due to the relatively large liquid-bridge volume. The model is able to successfully reproduce the same progression of outcomes as observed in the experiments, as shown in Figure 4.2, as well as other observed experimental trends.

4.5. Newton's Cradle Outcome

Encouraged by the robust model prediction of experimental trends, the parameter space of the model is extended even further to explore the possibility of achieving the NC outcome. A model-based map of $x_{f,2\text{-}3}$ versus St is shown in Figure 4.3. When the target spheres (2 and 3) separate after collision, the fluid in the connecting bridge fills the gap between the separating spheres as suction pressure draws in fluid. As described previously [3], $x_{f,2\text{-}3}$ is the final liquid thickness between these spheres, after which rebound is assumed to occur with no further resistance; $x_{f,2\text{-}3}$ is calculated based on the

liquid-bridge volume. St is defined as $mv_0/6\pi\mu a^2$, where v_0 is the initial impact velocity of the striker. Figure 4.3 shows the desired NC outcome in the lower-right corner. The top dotted line represents the original value of $x_{f,2\text{-}3}$ used in the prior experiments (Figure 4.2) and does not include NC. The absence of NC is consistent with experimental observations (FA, RNC, and then FS as impact velocity is increased while holding other parameters constant). This map suggests reducing the value of $x_{f,2\text{-}3}$ amply leads to a NC outcome, perhaps due to reduced viscous resistance (more discussion below).

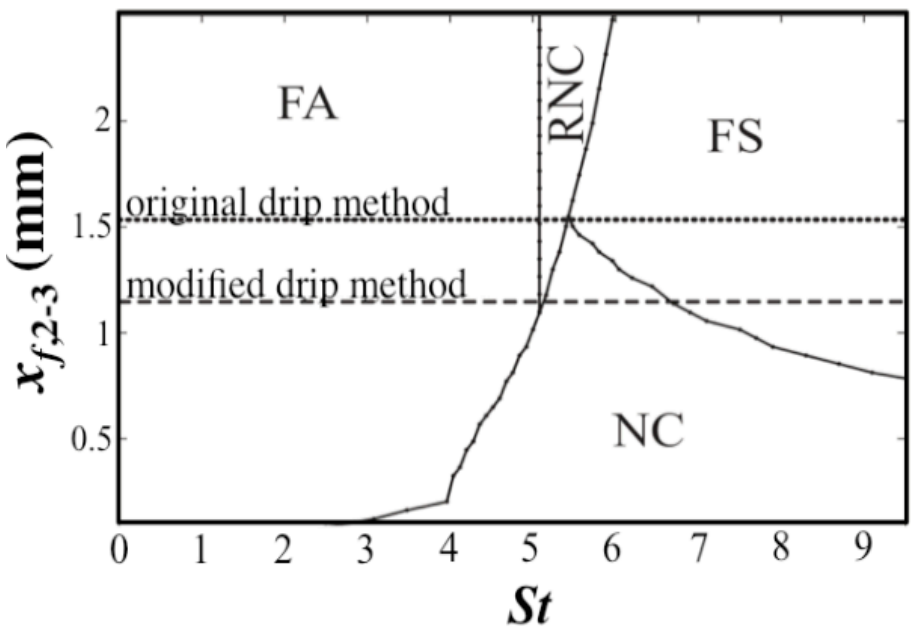

Figure 4.3 Model-based regime map of $x_{f,2\text{-}3}$ versus St for 12.0 Pa·s oil, chrome-steel spheres, and a 60 s drip time ($x_{0,1\text{-}2}$ = 410 μm, $x_{0,2\text{-}3}$ = 14 μm). The dotted line (top) represents the spheres dripped as an agglomerate, while for the dashed line (bottom) the spheres dripped separately. Note that $x_{0,2\text{-}3} << x_{f,2\text{-}3}$ since the two target spheres are pulled together by capillary forces prior to the collision.

In an attempt to experimentally achieve the NC outcome, the final thickness of the liquid layer between the initially motionless spheres ($x_{f,2\text{-}3}$) was decreased while all other parameters were kept constant. A smaller final thickness was achieved by modifying the dripping process to yield a smaller volume of the liquid bridge. For results presented thus

far and contained in our previous work [3], the two target spheres were dipped in the same coating bath and allowed to drip as an agglomerated pair with a liquid bridge connecting them. To reduce the bridge volume and consequently $x_{f,2\text{-}3}$, the target spheres in the current work are separated while undergoing the dripping process and are brought together just prior to the collision. In this way, fluid more easily drains from the pair, decreasing the excess fluid in the bridge ($x_{f,2\text{-}3}$ reduced) while maintaining the initial liquid-layer thicknesses ($x_{0,1\text{-}2}$ and $x_{0,2\text{-}3}$).

When using this modified dripping method and thus achieving a smaller liquid-layer thickness between spheres 2 and 3 upon rebound (dashed line in Figure 4.3), the previously missing NC outcome is indeed obtained at intermediate impact velocities, as suggested by the model-based regime map. In particular, outcomes of FA and NC are obtained as *St* is increased (i.e., going left to right in Figure 4.3); FS was not observed due to experimental limitations on the maximum velocity (i.e., *St*) that could be achieved. Figure 4.4 shows snapshots after the collision for a case where NC was achieved.

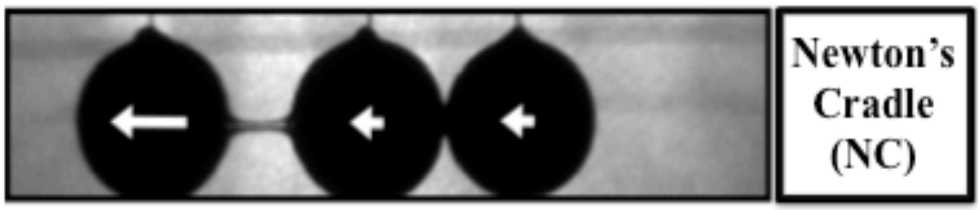

Figure 4.4 Snapshot after a collision with a NC outcome using 12.0 Pa·s oil, chrome-steel spheres and 60 s drip time ($x_{0,1\text{-}2}$= 410 μm, $x_{0,2\text{-}3}$= 18 μm, $x_{f,2\text{-}3}$= 1150 μm).

The experiments with the reduced value of $x_{f,2\text{-}3}$ (modified dripping method) show different outcomes that are consistent with model predictions over the parameter space explored (impact velocity, oil viscosity, oil thickness, and particle material). Notably, the

collisions between stainless-steel spheres, using 12.0 Pa·s oil and a 2 min modified dripping method, exhibited outcomes of FA at low *St*, RNC and FS at middle *St*, and NC at high *St*, as shown in Figure 4.5. On the other hand, NC was never observed for the collisions between spheres using 5.12 Pa·s oil, even when using the modified dripping method and even though this fluid has less viscous resistance, which is also consistent with the model within experimental uncertainty.

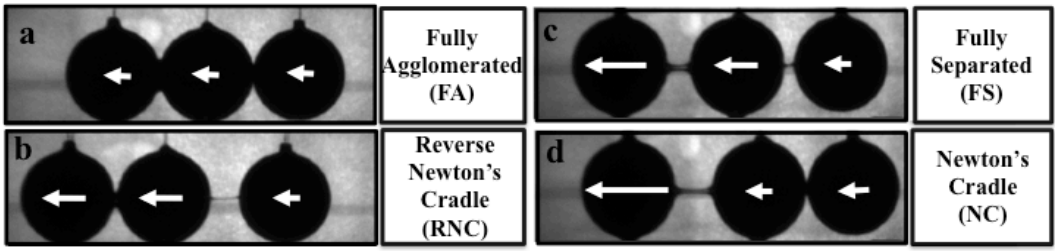

Figure 4.5 Experimental results of collisions that exhibit all four outcomes. Collisions used 12.0 Pa·s oil, stainless-steel spheres, and a drip time of 120 s ($x_{0,1\text{-}2}$ = 323 μm, $x_{0,2\text{-}3}$ = 11 μm, $x_{f,2\text{-}3}$ = 800 μm). (a) FA is observed at low velocities, (b) RNC and (c) FS at moderate velocities, and (d) NC at high velocities, consistent with the model-based regime map (not shown).

4.6. Discussion

Perhaps even more curious than the initial absence of the NC outcome itself is the physical reasoning that eventually leads to its discovery. Consider first the wetted spheres that once displayed FA, RNC and FS as *St* is increased (Figure 4.2). By decreasing the liquid bridge volume and thus $x_{f,2\text{-}3}$ (i.e., going 'downward' in the regime map of Figure 4.3), the resistance between target spheres (2 and 3) decreases. Consequently, it may seem natural that regions of low *St* that were once FA (2-3 and 1-2 agglomerated) would now separate and exhibit the NC outcome (2-3 separated and 1-2 agglomerated), since no change was made to the liquid layer between the striker and the

first target (1-2). However, both experiments and model predictions show that, as the 2-3 bridge thickness decreases, regions of the regime map (Figure 4.3) that were FA remain so (left-hand side), and regions of the regime map that exhibited FS (2-3 separated and 1-2 separated) now exhibit the NC configuration (Figure 4.4) for the same *St* (right-hand side). In other words, a change in the resistance between the 2-3 target spheres does nothing to the 2-3 outcome, but rather influences the 1-2 outcome. The ability of the hard-sphere model to successfully predict the outcome can be traced to the resolution of subsequent binary collisions (when one sphere 'catches up' to another after the first series of collisions), and is another testament to the robustness of the model. For example, one way of achieving FS in the model is if sphere 2 rebounds off 1, and 3 rebounds off 2. However, if after this first set of binary collisions, 2 transferred enough momentum to 3 so that 1 has a greater velocity than 2, they will collide again. If they stick together and their velocity is less than 3, a NC outcome will result. Physically, as the striker impacts the targets, the 2-3 liquid bridge dampens the momentum transfer to 3. Thus, 2 retains a larger portion of the momentum and does not become agglomerated with 1, which has lost most of its momentum. As the 2-3 bridge volume decreases, more momentum is transferred to 3, and 2 ends up with less momentum, so 1 and 2 agglomerate. This transition of the FS outcome to NC with decreasing $x_{f,2\text{-}3}$ at the same impact velocity is also counter-intuitive for another reason. Specifically, in two-sphere collisions, a decrease in the thickness of the liquid layer is associated with more 'bounciness' (i.e., a transition from agglomeration to rebound at a smaller *St*). A naïve translation to three-sphere collisions may imply that a thinner liquid layer would result in more separated spheres. However, the smaller $x_{f,2\text{-}3}$ results in two agglomerated spheres (NC), while a

thicker layer results in all three spheres separated (FS) for the same *St*. So, a thinner liquid layer does not always result in more spheres rebounding, as confirmed by experiments and predictions alike.

Beyond the surprising experimental results and physical explanation described above, the three-sphere collisions examined here provide a rare example of when a more complicated system reveals a physical process that is important to, but not revealed by, a simpler system. Previous two-body models predict that the pressure in the liquid gap during rebound drops below the vapor pressure of the oil and thus cavitation was assumed to occur [1, 6]. Thus, no lubrication resistance upon rebound was included in the previous models and the concept of a final rebound thickness (x_f) is thus irrelevant. In two-sphere collisions, the role of resistance during rebound is difficult to test, since the final thickness cannot be independently changed without also changing the initial thickness (i.e., no liquid bridge as a source of excess fluid exists prior to collision). However, in the more complex three-sphere system, the final thickness between the target spheres can be independently changed, since it is controlled via the bridge volume while the initial thickness is controlled by the surface tension that pulls the spheres together. As described above when holding all other parameters constant, a decrease in bridge thickness qualitatively changes the results. Thus, investigating three spheres instead of two spheres leads to an important physical finding: outbound resistance plays a major role in the collisional process, even under conditions in which it appears that cavitation may be present. Probing the physics of systems with more than two spheres is necessary to understand de-agglomeration since it involves an existing agglomerate colliding with another body. The plethora of unexpected results described above, such as the initial

absence of the NC outcome or more de-agglomeration with a larger liquid bridge, is not possible from two-body studies. Accordingly, this three-body work is an important step toward the macro-behavior of practical, many-body systems.

Literature Cited

1. Kantak, A.A. and R.H. Davis. Elastohydrodynamic theory for wet oblique collisions. *Powder Technology* **168**, 42-52, (2006).
2. Davis, R.H., D.A. Rager, and B.T. Good. Elastohydrodynamic rebound of spheres from coated surfaces. *Journal of Fluid Mechanics* **468**, 107-119, (2002).
3. Donahue, C.M., C.M. Hrenya, R.H. Davis, K.J. Nakagawa, A.P. Zelinskaya, and G.G. Joseph. Stokes' cradle: normal three-body collisions between wetted particles. *Journal of Fluid Mechanics* **650**, 479-504, (2010).
4. Weber, M.W. and C.M. Hrenya. Square-well model for cohesion in fluidized beds. *Chemical Engineering Science* **61**, 4511-4527, (2006).
5. Weber, M.W. and C.M. Hrenya. Computational study of pressure-drop hysteresis in fluidized beds. *Powder Technology* **177**, 170-184, (2007).
6. Davis, R.H., J.M. Serayssol, and E.J. Hinch. The Elastohydrodynamic Collision of 2 Spheres. *Journal of Fluid Mechanics* **163**, 479-497, (1986).

5. OBLIQUE COLLISIONS OF TWO WETTED PARTICLES USING A PENDULUM APPARATUS[6]

5.1. Abstract

Experiments using a pendulum apparatus are conducted for two particles engaged in oblique wetted collisions over a range of impact angles, impact velocities, coating thicknesses, liquid viscosities, particle materials, and particle radii. As established in previous studies, in normal (head-on) collisions, particles de-agglomerate if the Stokes number is greater than the critical Stokes number. However, in oblique collisions, so-called centrifugal forces can cause particles to de-agglomerate for a Stokes number less than the critical Stokes number. Surprisingly, the resulting trends of the normal (wet) restitution coefficient and the angle the doublet rotates during the collision are different depending on whether the Stokes number is less than or greater than the critical Stokes number. An accompanying theory based on lubrication, solid deformation, and the glass transition of the liquid layer agrees well with experimental results and gives insight into the observed trends.

---

[6] Donahue, C.M., W.M. Brewer, R.H. Davis, and C.M. Hrenya, *Agglomeration and De-agglomeration of Rotating Wet Doublets*. Submitted, (2011).

5.2. Introduction

Previous experimental and theoretical studies have focused on head-on collisions between two particles and head-on or oblique collisions between a particle and a wall [1-5]. However, in many-particle flows, collisions between two particles are more often than not oblique. Unlike particle-wall collisions, the particles in an oblique particle-particle collision can form a doublet and rotate. Such rotation may cause particles to de-agglomerate solely due to centrifugal forces.

In this chapter, a microscopic approach is taken to investigate collisions between two wetted particles in which viscous (dynamic) forces dominate over capillary (static) forces, and the liquid flow is in the low-Reynolds-number regime. Consequently, Stokes flow prevails and the normal Stokes number,

$$St_n = mv_{0,n}/6\pi\mu a^2, \tag{5.1}$$

has been found to be a key dimensionless parameter [3, 6]. Here, $m = m_1m_2/(m_1+m_2)$ is the reduced mass, $v_{0,n}$ is the normal component of the relative impact velocity, μ is the liquid viscosity, and $a = a_1a_2/(a_1+a_2)$ is the reduced radius. For normal collisions, de-agglomeration of particles occurs for values of St_n greater than a critical Stokes number, namely St_n*. The value of St_n* can be determined either empirically via experiments or theoretically by considering both the properties of the fluid and the solid particles [2, 7, 8]. In *immersed* collisions dominated by Stokes flow, velocity reversal of a particle impacting a wall occurs when St_n is greater than a critical value of Stokes number, St_n*, approximately equal to 10 [9, 10] for both normal and oblique collisions. Experiments of *wetted* particle-wall oblique collisions have shown that, for a range of St_n greater than

St_n*, the normal and tangential motions are approximately decoupled, which suggests that the value of St_n* found in head-on collisions might also demarcate agglomeration versus de-agglomeration in oblique collisions [4]. However, the ability of St_n* to predict agglomeration versus de-agglomeration in oblique collisions was not verified due to experimental limitations.

Unlike previous efforts, here we investigate oblique collisions between two wetted particles. Experiments are performed using a pendulum apparatus and are compared to theoretical predictions. In contrast to oblique, particle-wall collisions, the target is now mobile, such that an agglomerated doublet (connected by a liquid bridge) can form and rotate. We observe a new outcome for oblique, particle-particle collisions in which two colliding particles initially form an agglomerate and then later de-agglomerate due to centrifugal forces. A corresponding theory is also developed that agrees well with the regime map of outcomes for impact angle versus St_n, and both experiments and predictions show that the new outcome occurs at large impact angles for $St_n < St_n$*. Finally, we investigate a range of parameters for different liquid viscosities, coating thicknesses, particle materials and particle radii and analyze the corresponding trends of the (wet) normal restitution coefficient and rotation angle. Surprisingly, the trends depend on whether a de-agglomerating collision occurs for $St_n > St_n$* or $St_n < St_n$*. Furthermore, the theory is able to predict the trends and provides further insight into the physical mechanisms responsible for particle reversal and de-agglomeration.

5.3. Experimental Setup

The experimental setup is composed of two solid spheres suspended with pendulum strings of 1 m length, as shown in Figure 5.1. The pendulums strings are attached from above to a rotating glass plate. The string holding the striker is attached to the center of the plate, so that when the plate is rotated its position does not change (Figure 5.1b). The string holding the target particle is attached one particle diameter away from the striker string. As the plate is rotated, the position of the target particle moves relative to the striker such that a range of impact angles is possible (Figure 5.1c). Prior to the collision, the striker particle is held in place by a gate that employs a solenoid as the release mechanism. The position of the gate can be moved along the track to achieve different impact velocities. The target particle is coated with silicon oil, which is contained in a bath positioned underneath the target particle. The bath lifts to coat the particle, and the time that the liquid is allowed to drip from the particle prior to collision determines the thickness of the liquid coating at collision.

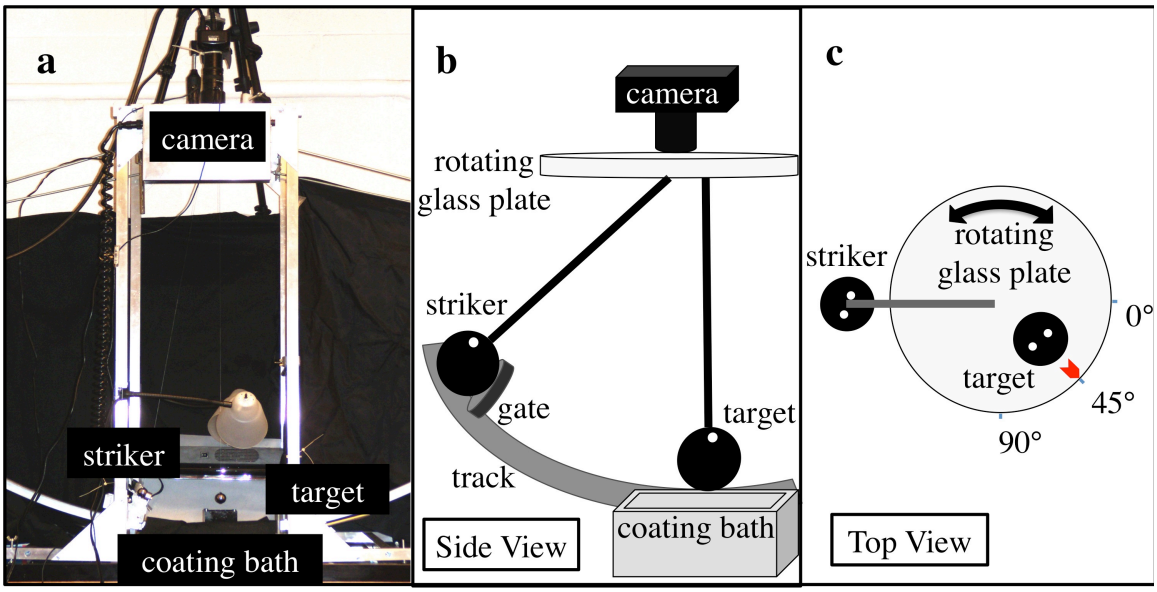

Figure 5.1 Experimental setup: (a) photograph from the side view, and schematic from the (b) side view and (c) top view of the pendulum apparatus.

5.3.1. Materials

The pendulum string is attached to the particles via a small tube welded on the top of the particle. The string is ice fishing line manufactured by Berkley, chosen for its high spring constant (stiff) of 1.2 kN m^{-1}, which balances the centrifugal acceleration of the striker particle as it swings through an arc before it collides with the stationary target particle. The particles are either chrome steel (AISI 52100) or stainless steel (316 grade). The properties of the chrome-steel particles are: dry restitution coefficient e_{dry} = 0.99; Young's modulus $E = 2.03 \times 10^{11}$ N/m^2; Poisson's ratio $\nu = 0.28$; density $\varrho = 7830$ kg/m^3; reduced radius a = 6.4 mm or 4.0 mm. The properties of the stainless-steel particles are: dry restitution coefficient e_{dry} = 0.90; Young's modulus $E = 1.93 \times 10^{11}$ N/m^2; Poisson's ratio ν = 0.35; density ϱ = 8030 kg/m^3; reduced radius a = 6.4 mm. The particles are coated with silicon oil of viscosities 5.1, 12, or 99 Pa·s at 25 °C, which is the nominal

temperature of the experiments, and all three oils have densities of 0.97 g/cm^3. To summarize the properties, a list of the collisional parameters can be found in Table 5.1. The notation used to describe each case refers to viscosity, namely low (μ_{low}), medium (μ_{med}), or high (μ_{high}); coating thickness, namely small layer ($x_{0,small}$), medium layer ($x_{0,med}$), large layer ($x_{0,large}$), or extra-large layer ($x_{0,xlarge}$); particle material, namely chrome steel (cs) or stainless steel (ss); and particle radius, namely large (a_{large}) or small (a_{small}).

Table 5.1 Experimental parameters.

Case	Liquid Viscosity (Pa·s)	Coating Thickness (μm)	Steel Particle Material	Particle Radius (mm)
μ_{low}_$x_{0,med}$_ss_a_{large}	5.12	270	Stainless	12.7
μ_{low}_$x_{0,small}$_ss_a_{large}	5.12	180	Stainless	12.7
μ_{med}_$x_{0,med}$_cs_a_{small}	12.0	263	Chrome	7.9
μ_{med}_$x_{0,large}$_cs_a_{large}	12.0	418	Chrome	12.7
μ_{med}_$x_{0,large}$_ss_a_{large}	12.0	420	Stainless	12.7
μ_{med}_$x_{0,med}$_cs_a_{large}	12.0	270	Chrome	12.7
μ_{med}_$x_{0,med}$_ss_a_{large}	12.0	270	Stainless	12.7
μ_{high}_$x_{0,xlarge}$_ss_a_{large}	99.0	850	Stainless	12.7

5.3.2. Methods

To characterize the collisions, two sets of measurements are performed: (i) off-line measurements of the thickness of the liquid layer coating the target particle and (ii) on-line measurement of pre- and post-collisional velocities (linear and rotational) and impact angle. First, measurements of the coating thickness are made independently from

the collisions with a high-resolution Pentax SLR K110D with 6.1 megapixels. Wide-angle distortion is minimized using a zoom lens that allows the camera to be placed approximately 1.5 m away from the coated particle. Photographs are taken every 3 s during the dripping process, and the process is repeated 5 times. The lighting, aperture, and shutter speed are set at levels to make the particle, and particularly the edge of the particle, well defined and dark with respect to the background. The photographs are analyzed in *Matlab*, and the coating thickness is found from a given photograph by subtracting the edge-to-edge distance of the dry particle photograph from the wet particle, and then dividing the resulting quantity in half. The coating thickness is then found for a particular drip time from a linear fit of these off-line data five seconds before and after the drip time. The error in the measurements of the coating thickness is approximately ± 5 μm.

Second, the particle positions, and hence the relevant velocities and geometries, are tracked in time throughout the collisional process using a high-speed camera that is placed above the rotating glass plate. The camera is manufactured by DVC (model 340 M) with a 640 × 480 pixel resolution. However, depending on the impact velocity and angle, the effective resolution ranges between approximately 200 × 75 and 400 × 175 pixels. Similar to the high-resolution camera, a Navitar 7000 zoom lens allows for the camera to be placed approximately 1 m from the particles, so that wide-angle effects are essentially eliminated. The camera operates at 40MHz with a frame rate of 320 ms. Two fluorescent dots are painted on the top of each particle, and the apparatus is lit using fluorescent lights only. In this way, the camera tracks only the dots, so that linear and angular velocities and the impact angle can be extracted using image tools in *Matlab*.

Depending on the impact angle and the impact velocity, the translational-velocity error ranges between 0.010 and 0.023 m/s, the rotational-velocity error ranges between 0.006 and 0.015 rad/s, and the impact-angle error ranges between 0.9° and 6.2°.

5.4. Theory Description

To illuminate the dominant physical mechanisms, the theory for two-particle, wetted, oblique collisions is developed. In addition to the typical fluid forces, tension from the pendulum strings is included. As the doublet rotates from its impacting position, tension from strings arises that resist normal and rotational motion. The relevant dimensionless numbers are the Reynolds number *Re*, and the capillary number *Ca*. The largest Reynolds number (ratio of fluid inertia to fluid viscous forces in the liquid gap between colliding particles) encountered experimentally is

$$Re_{max} = \rho v_{0,n} x_0 / \mu = 0.04 \quad , \tag{5.2}$$

where ρ is the liquid density, $v_{0,n} = v_0 \cos \theta_0$ is the initial normal component of relative velocity between particles, θ is the angle between the relative velocity and the line connecting the centers of the particles at initial contact and the subscript 0 indicates the initial impact value, x_0 is the initial coating thickness, and μ is the liquid viscosity (figure 5.2). Therefore, the collisions occur at low *Re*, and the dynamics of the liquid between the particles is governed by Stokes flow (lubrication). The smallest capillary number (ratio of viscous forces in the liquid gap between the particles to capillary forces between the particles) encountered is

$$Ca_{\min} = 3\mu a v_{0,n} / \sigma x_0 = 1500 \quad , \tag{5.3}$$

where σ is the surface tension of the silicon oil. Since $Ca >> 1$, capillary forces are negligible, as was confirmed by Salcudean *et al*. [12]. Finally, an evaluation of the Stokes number for a particle suspended in air shows resistance from the interstitial air is negligible.

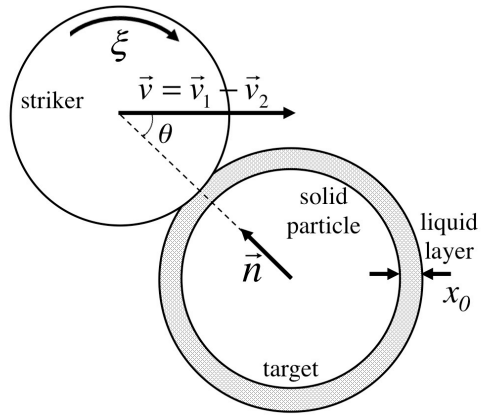

Figure 5.2 Impact geometry.

5.4.1. Lubrication

The viscous (lubrication) force that resists the relative motion of the particles acts in both the normal and the tangential directions. For small deformations and for $x << a$, the normal component of the lubrication force has been derived by Kantak & Davis (2006) for liquid-coated spheres as

$$F_{L,n} = \frac{6\pi\mu a^2 v_n}{x}\left(1 - \frac{x}{x_0}\right)^2, \tag{5.4}$$

where the subscript n indicates the normal direction. The normal vector, $\vec{n}$, is a unit vector that points from the center of the target to the center of the striker (figure 2). In

the tangential direction, the force between two immersed particles was solved numerically by Kantak and Davis [13] such that

$$F_{L,t} = -24\pi\mu a^2\left(\frac{1}{3}\ln\frac{2a}{x_0}(\omega-\xi)+1.2720\omega+0.1583\xi\right). \tag{5.5}$$

Here, $\omega = (v/4a)\sin\theta$ is the angular velocity of the doublet about the center of mass of the doublet, ξ is the angular velocity of each single particle about its center of mass (i.e., rotational velocity of particle), and the subscript t indicates the tangential direction (figure 2). In this work, the particles are wetted rather than immersed; therefore, the second and third terms on the right hand side of Equation 5 are omitted since they are due to the viscous resistance from the liquid in the outer region (absent for wetted particles) away from the liquid gap between the particles. Since both particles initially do not rotate about their centers ($\xi_{\text{striker}} = \xi_{\text{target}} = 0$) and the fluid exerts an equal-magnitude force on each particle, the corresponding angular accelerations of the two identical particles are also equal; therefore, throughout the collision the particles have equal angular velocities ($\xi_{\text{striker}} = \xi_{\text{target}} = \xi$). Finally, when $\omega = \xi$, the surfaces of the particles do not move relative to each other and thus there is no shearing of the fluid between the particles (i.e., $F_{L,t} = 0$).

5.4.2. String Tension

To accurately model the experiments, the force of tension from the pendulum strings must be accounted for. In particular, at the moment the striker particle collides with the target particle, tension only acts in the vertical direction parallel to gravity; therefore, string tension does not influence the collision at the moment of impact (i.e.,

tension is balanced by gravitational force). However, as the particles begin to rotate about the center of mass of the doublet, the pendulum strings are no longer aligned with gravity. Consequently, tension from the pendulum strings emerges in both the normal and tangential directions. In the normal direction, this tension is

$$F_{S,n} = \frac{8mga}{l}\sin^2\left(\frac{\beta}{2}\right)\sqrt{1-\frac{16a^2}{l^2}\sin^2\left(\frac{\beta}{2}\right)}, \tag{5.6}$$

where g is the acceleration of gravity, l is the length of the pendulum string, and β is the angle the doublet has rotated from the time of the initial impact. In the tangential direction, the tension from the strings is

$$F_{S,t} = -\frac{4mga}{l}\sin(\beta)\sqrt{1-\frac{16a^2}{l^2}\sin^2\left(\frac{\beta}{2}\right)}. \tag{5.7}$$

5.4.3. Kinematic Equations

The kinematic equations corresponding to the experimental setup are

$$\frac{dx}{dt} = -v_n, \tag{5.8}$$

$$m\frac{dv_n}{dt} = F_{L,n} + F_{S,n} - 4ma\omega^2, \tag{5.9}$$

$$\frac{d\beta}{dt} = \omega, \tag{5.10}$$

$$4ma\frac{d\omega}{dt} = F_{L,t} + F_{S,t} + 2mv_n\omega, \tag{5.11}$$

$$\frac{8}{5}ma\frac{d\xi}{dt} = -F_{L,t}. \tag{5.12}$$

Equations 8-12, together with expressions given for the lubrication and tension forces above (Equations 4-7), are solved in time for x, β, v_n, ω, and ξ. The particles approach each other with an initial separation equal to the initial (measured) coating thickness x_0 (Equation 4), normal impact velocity $v_{n,0} = v_0 \cos \theta_0$, initial angular velocity of the agglomerate $\omega_0 = v_0 \sin \theta_0/(4a)$, and initial angular velocity of each particle $\xi_0 = 0$. Upon approach, the particles may stick (agglomerate) if their normal relative acceleration and velocity drop to zero. During the collisional process, the particles may reverse direction due to (i) centrifugal forces, or by (ii) encountering a reversal criterion also present in normal collisions (i.e., glass transition of liquid layer, elastohydrodynamics, or surface roughness), which is discussed in more detail below (Section 5.4.4). As the particles move away from each other, they may stick (agglomerate) if their normal acceleration and velocity drops to zero due to viscous resistance. Otherwise, de-agglomeration is said to occur when their separation distance reaches x_0. Additionally, the simulations are stopped and are considered to stick (agglomerate) if the doublet rotates 180° from its initial position (at which point the strings cross) or if the angular velocity of the doublet reverses before a separation distance equal to x_0 is achieved.

To assess the accuracy of the theory, predictions of the angular velocity of the doublet (ω) and the angular velocity of the particles (ξ) over time are compared to experimental results in Figure 5.3. The error in ω is generally smaller than the error in ξ, since two sets of two dots painted on the top of each particle spaced further apart are used to determine ω, whereas only one set of dots is used to find ξ. As mentioned previously, when $\omega = \xi$ (time ~ 0.01 s), the surfaces of the particles no longer rotate relative to each other, and the doublet has formed an approximately rigid dumbbell. The initial rapid

decline in ω and the corresponding rapid incline in ξ over this short time is due to the tangential lubrication as the doublet quickly forms a dumbbell. At longer times, the relatively slow decline in ω and ξ results from string tension. As mentioned previously, the tangential lubrication theory used here is a modified version of that for two immersed spheres; since the results for the conditions in Figure 5.3 are representative of the rest of the parameter space, the modified immersed theory serves as a good approximation for wetted particles.

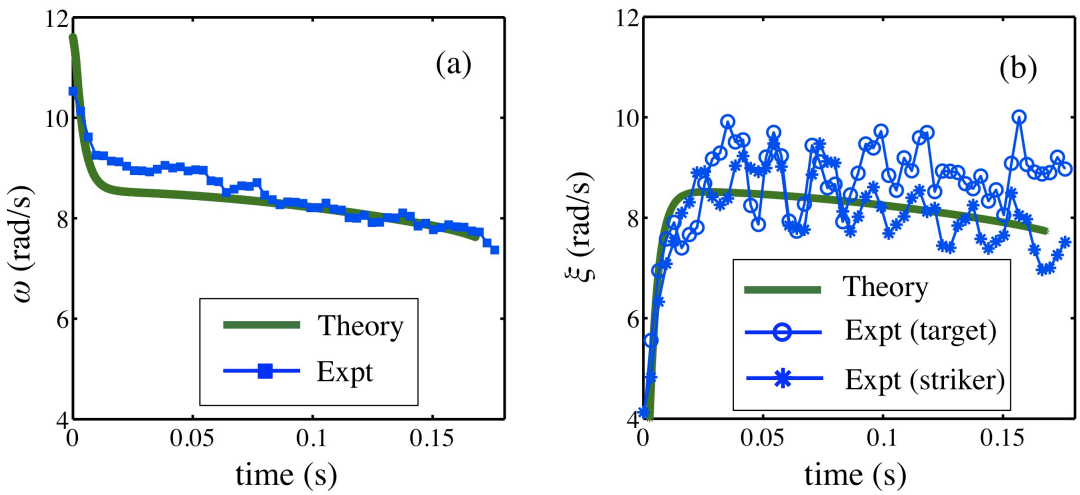

Figure 5.3 Experimental results and theoretical predictions of the angular velocity of (a) doublet (ω) and (b) angular velocity of the particles (ξ) over time for a collision of case $\mu_{\text{med}}\_x_{0,\text{thick}}\_\text{cs}\_a_{\text{large}}$ for St_n equal to 1.1 and $\theta_0 = 46°$. The initial rapid decline of the doublet angular velocity is due to the tangential lubrication force (time ~< 0.02 s), while the slower decline at longer times is due to the string tension (time ~> 0.02 s).

5.4.4. Reversal Criteria

As stated previously, when the particles approach each other for normal (head-on) collisions, three mechanisms have been identified that cause the particles to deform and then reverse their relative motion: (i) glass-transition of the liquid, (ii) elastohydrodynamic forces, and (iii) particle roughness. First, the pressure in the liquid

gap rapidly increases during approach; if the pressure exceeds the glass-transition pressure, p_{gt}, then the liquid behaves as a solid and the particles reverse direction. The glass-transition rebound separation is

$$x_{gt} = \sqrt{\frac{3\mu a v_n x_0^2}{\left(p_{gt} - p_{atm}\right)x_0^2 + 3\mu a v_n}} \approx \sqrt{\frac{3\mu a v_n}{(p_{gt} - p_{atm})}} \qquad \text{when } x_{gt} << x_0, \qquad (5.13)$$

where p_{atm} is the atmospheric pressure [8]. Second, the large lubrication pressures cause the solid particle to deform; the stored energy in this deformation leads to reversal in the relative normal motion if the following separation length scale, determined using a coupling of elastic and lubrication theories (i.e. elastohyrdrodynamics), is reached:

$$x_r = \left(6\pi\Theta\mu a^{3/2} v_n / \sqrt{2}\right)^{2/5}, \qquad (5.14)$$

where $\Theta = 2(1-\nu^2)/\pi E^2$ and ν is Poisson's ratio and E is Young's modulus [6]. Finally, the surface roughness, x_b, is assumed to be 1 μm based on previous measurements of similar materials [1], and the particle surfaces will touch and the relative normal particle velocity will reverse if this separation is reached. If the theory predicts that any one of the three reversal criteria has been met upon approach (i.e., the gap x decreases to the largest of x_{gt}, x_r, or x_b), then the particles deform and rebound with their normal relative velocity reversed and multiplied by the dry restitution coefficient e_{dry} to account for the (kinetic) energy dissipation experienced by the particle during deformation.

To assess the accuracy of the new component of our theory (involving rotational motion of oblique collisions), it is essential to start with accurate predictions for normal (head-on) collisions. In previous work, the glass-transition rebound criterion dictated the reversal process for the conditions investigated and was critical in the prediction of the correct outcomes and trends for normal three-body collisions [8]. In that three-body

work, a pendulum apparatus was also used, and the materials and the range of parameters used were similar to this work. The theory used in Donahue *et al*. [8] is the same in this work for head-on collisions with $\omega = \xi = 0$. Therefore, not surprisingly, the glass-transition state is the first reversal criterion met in the theoretical predictions here. Due to a lack of well-established data for the value of p_{gt} for silicon oil, the value of p_{gt} has been chosen for each different viscosity oil used based on the experimental value obtained for St_n*. Figure 5.4 compares the normal wet restitution coefficient, $e_{w,n}$, found in experiments for normal collisions against the theoretical predictions. Since, for normal collisions, $e_{w,n}$ is a ratio of the magnitude of the relative post-collisional velocity to that of the pre-collisional velocity, $e_{w,n} = 0$ when the particles stick (agglomerate), and $e_{w,n} > 0$ when the particles bounce (de-agglomerate). Here, St_n increases due to an increase in impact velocity, as all other parameters remain unchanged. In Figure 5.3, $St_n^* = 1.5$, representing the value of St_n at which $e_{w,n}$ transitions to a non-zero value. The current theoretical predictions agree well quantitatively and qualitatively with experimental results. Two other theories are also compared to experimental results. The theory of Kantak & Davis [13] uses a complete treatment of elastohydrodynamics to model a wetted collision, but with constant viscosity. The theoretical predictions of Kantak & Davis [13] have a somewhat fortuitous match of St_n*, since not including the glass transition provides for closer approach and more resistance that balances the lack of (known) resistance upon rebound due to presumed cavitation; however, $e_{w,n}$ is underpredicted for $St_n > St_c$*. The more simplified theory by Davis *et al*. [14], in which particles only rebound due to surface roughness, has the simple form $St_n = e_{dry}$ (1-St_n^*/St_n) for $St_n > St_n^*$, where $St_n^* = \ln (x_0/x_b)$. Here, x_b is chosen such that St_n^* matches

the experimental value. Again, the theory underpredicts the value of $e_{w,n}$ for $St_n > St_n^*$. Compared to the other two theories that do not include the glass transition, the current theory is the appropriate choice for this work.

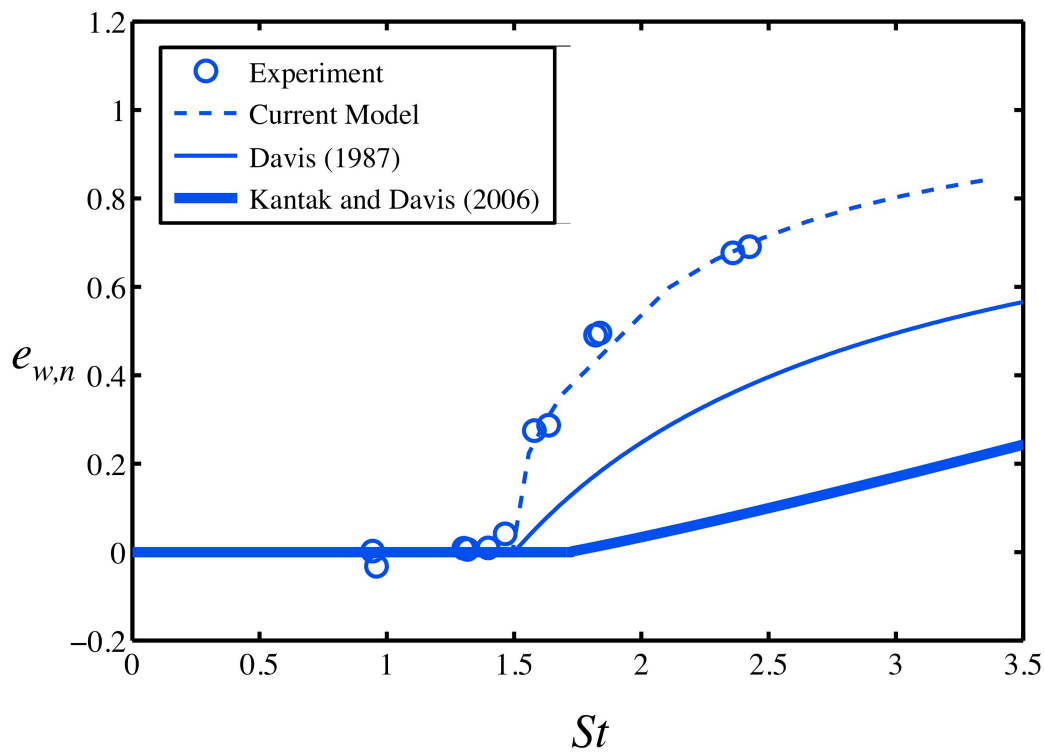

Figure 5.4 Restitution coefficient for normal (head-on) collisions for case $\mu_{\text{med}}\_x_{0,\text{large}}\_\text{ss}\_a_{\text{large}}$ compared for the current theory, Davis [14], and Kantak and Davis [15].

5.5. Results and Discussion

In Figure 5.5, three sets of collision snapshots are shown, and only the impact velocity between the three sets was changed. The three sets represent the three different outcomes observed in the wetted oblique collisions. Two of the outcomes were also observed in previous experimental works involving wetted normal particle-particle and

oblique particle-wall systems, namely stick (S, Figure 5.5a) in which the striker particle forms an agglomerate with the target object, and bounce (B, Figure 5.5c) in which the striker collides with the target and essentially immediately separates [4, 16]. Conversely, an outcome only observed in oblique particle-particle collisions is shown in Figure 5.5b [11]. Here, the two particles collide and initially stick together, and then at a later time after the agglomerate has rotated through a significant angle, the two particles de-agglomerate due to centrifugal forces. This outcome, characterized by collisions that eventually separate but have collision durations greater than for head-on collisions, is named stick-rotate-separate (SRS).

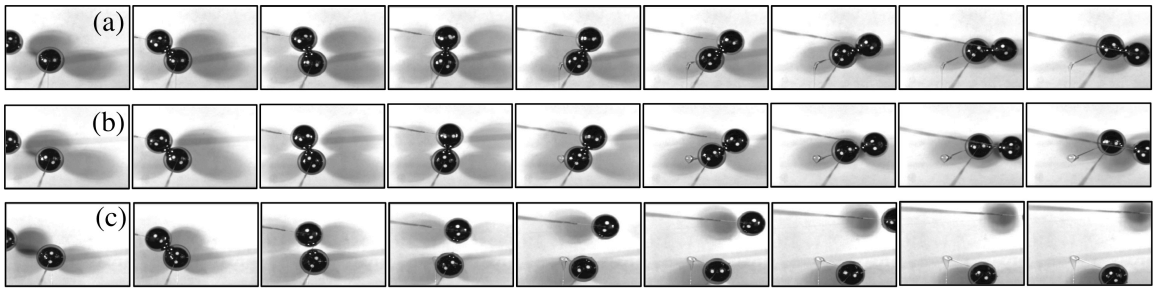

Figure 5.5 Top-view snapshots (using high-speed camera) of collisions with outcomes of (a) stick (S), (b) stick-rotate-separate (SRS), and (c) bounce (B) for parameters of case $\mu_{\text{med}}\_x_{0,\text{large}}\_\text{cs}\_a_{\text{large}}$ and $\theta_0 = 45°$. Only the normal impact velocity changes between the three subfigures such that the velocities are (a) 0.25 m/s ($St_n = 0.95$), (b) 0.29 m/s ($St_n = 1.1$), and (c) 0.34 m/s ($St_n = 1.3$).

5.5.1. Comparison of Experiment and Theoretical predictions

As a first validation of the theory, Figure 5.6 contains experimental data and theoretical predictions for case $\mu_{\text{med}}\_x_{0,\text{thick}}\_\text{ss}\_a_{\text{large}}$. Figure 5.6a shows the regime map of outcomes over a range of impact angle and St_n. The symbols represent outcomes

of individual experimental collisions (stick, stick-rotate-separate, and bounce), and the lines represent the boundaries between the various outcomes predicted by the theory. Overall, good agreement is achieved between experiment and theoretical predictions, except the observed impact angle that separates stick and stick-rotate-separate for a given St_n is higher than the predicted boundary. For normal collisions (θ_0 = 0º), the Stokes number at the transition between stick and bounce, St_n*, is equal to 1.4. For oblique collisions, experiments and theoretical predictions show generally that, if $St_n < St_n$*, particles either stick or stick-rotate-separate, whereas if $St_n > St_n$*, particles bounce. For all parameters listed in table 1, the regime maps are qualitatively similar in that all three outcomes are observed in analogous regions of the parameter space.

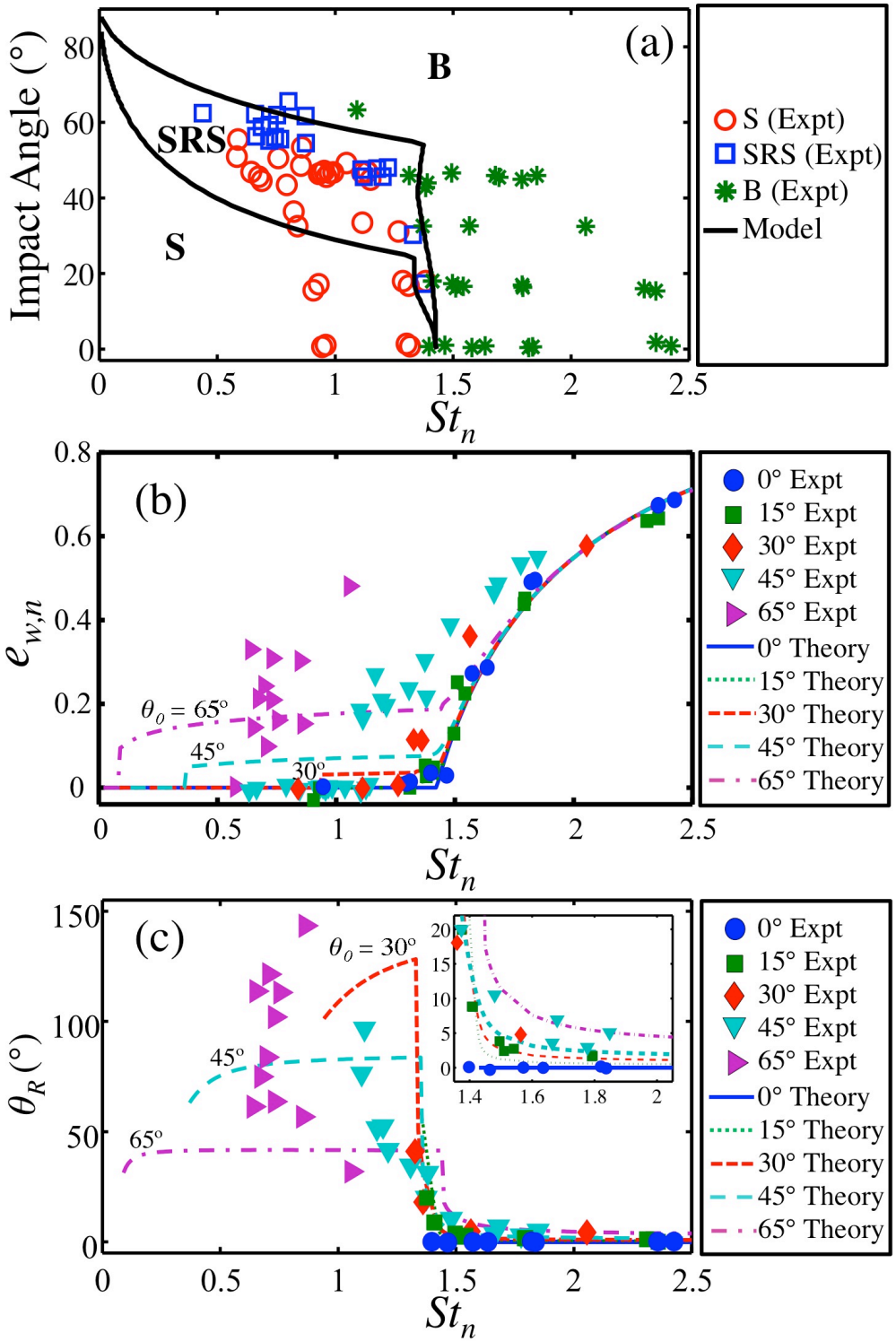

Figure 5.6 (a) Regime map of outcomes, (b) normal restitution coefficient and (c) rotation angle for case μ_{med}_$x_{0,\text{large}}$_cs_a_{large}. The inset in (c) is a close up of the theoretical predictions and experimental results in the vicinity of St_n*.

In collisions between dry particles, the normal restitution coefficient has traditionally been defined as $e_n = -(\vec{v}_f \cdot \vec{n}_0)/(\vec{v}_0 \cdot \vec{n}_0)$, where the subscripts 0 and *f* represent the initial and final values, respectively. This definition is sufficient for dry collisions, since the collision duration is short and particles do not rotate far; in other words, $\vec{n}$ does not vary significantly during the collision. But, when the particles do rotate significantly, as is true for sufficiently oblique collisions between wetted particles, so does the normal vector. Anomalous behavior of the restitution coefficient due to the rotation of the colliding particles was first observed in nanocluster collisions reported by Saitoh *et al.* [17]. Therefore, in this work, the definition of the (wetted) normal restitution coefficient used is

$$e_n = -(\vec{v}_f \cdot \vec{n}_f)/(\vec{v}_0 \cdot \vec{n}_0) \ . \tag{5.15}$$

Using this modified definition of the normal restitution coefficient, $e_{w,n}$ is plotted versus St_n in Figure 5.6b for a range of impact angles. All subfigures in Figure 5.6 are plotted versus the same range of St_n for comparison. For each specified impact angle, symbols represent experimental collisions within 5° of the given angle, and curves represent the theoretical predictions. The theory agrees well with the experiment and correctly predicts the trend of $e_{w,n}$ as the impact angles changes. In particular, the curves of $e_{w,n}$ for impact angles of 15° and 30° are similar to the curve of the 0° collisions in both experiment and theory. Therefore, the small change in the value of $e_{w,n}$ at small impact angles indicates that centrifugal forces associated with the rotating pair play a negligible role in the de-agglomeration of these (nearly head-on) collisions. The curves of $e_{w,n}$ for larger impact angles of 45° and 65° show collisions de-agglomerate ($e_{w,n} > 0$) for $St_n < St_n^*$

in both experiment and theory, and this de-agglomeration is the stick-rotate-separate (SRS) mechanism due to centrifugal forces. The corresponding predictions for $St_n > St_n^*$ are instead dominated by the same bounce (B) mechanisms that cause reversal in normal collisions, which is why they appear to collapse on the $\theta_0 = 0^o$ curve. The discontinuity in the slope observed at St_n^* is due to the different mechanisms responsible for de-agglomeration for $St_n < St_n^*$ versus $St_n > St_n^*$. The scatter in measured $e_{w,n}$ increases as θ_0 increases, since the uncertainty in the measured θ_0 increases with θ_0 and more error is associated with the stick-rotate-separate outcome due to the sensitivity of rotation angle to impact velocity (Figure 5.6c).

In addition to comparing the normal components of motion, the rotational motion of an agglomerate is also investigated by comparing the rotation angle. The rotation angle, θ_R, is the angle through which an agglomerate rotates between initial impact and de-agglomeration:

$$\theta_R = \int_0^{t_c} \omega(t)\,dt \ , \tag{5.16}$$

where t_c is the collision duration (i.e., the time during which the spheres are in near-contact with $x < x_0$ during the collision). Therefore, if either the collision duration or the doublet angular velocity ω increases, θ_R also increases. Figure 5.6c is a plot of θ_R versus St_n for those collisions that de-agglomerate (SRS and B). Near St_n^*, a sharp decrease in θ_R is observed for a given θ_0 in both experiment and theory as the outcome transitions from stick-rotate-separate to bounce. This observation stems from the fact that the collision duration of a stick-rotate-separate collision ($St_n < St_n^*$) is much longer than that for a bounce collision ($St_n > St_n^*$), allowing for the particles to rotate further during the collision. Moreover, for $St_n > St_n^*$, θ_R increases as θ_0 increases for a given St_n in both

experiment and theory, which is more clearly seen in the inset. In this region, the relative normal velocity of the particles reverses direction due to the normal reversal criteria; therefore, the collision duration is primarily dependent on impact velocity (collision duration decreases as impact velocity increases) and not on θ_0. However, as θ_0 increases, the angular velocity of the agglomerate increases so that the particles rotate a larger distance in the same amount of time.

On the other hand, for $St_n < St_n^*$ the opposite trend is observed in Figure 5.6c; the rotation angle decreases as impact angle increases at fixed St_n in both experiment and theory. In this region, the centrifugal force is responsible for de-agglomeration, and the magnitude of the centrifugal force increases with impact angle in proportion to the square of the angular velocity. Therefore, the decrease in the collision duration due to increased centrifugal forces dominates over the increased angular velocity, and the particles do not rotate as far as θ_0 increases. While the theory predicts well the qualitative features of the experimental observations, a quantitative mismatch still persists. This quantitative mismatch may be due to the deformation of the liquid bridge as the particles move apart and liquid is pulled into the bridge.

The theory not only predicts the dynamics of the collisions, but, because it allows for physical mechanisms to be turned "on" and "off", the influence of each factor can be ascertained. In Figure 5.7, $e_{w,n}$ and θ_R are plotted both with string tension included and with string tension removed. Note that the values of $e_{w,n}$ and θ_R are largely unaffected by turning off the string tension in regions where collisions had de-agglomerated with string tension (i.e., for $\theta_0 = 15°$, $St_n > 1.4$; for $\theta_0 = 30°$, $St_n > 1$; for $\theta_0 = 45°$, $St_n > 0.5$; and for $\theta_0 = 65°$, $St_n > 0.2$). Therefore, as described in the next section, the trends in $e_{w,n}$ and θ_R for de-

agglomerating collisions are also not greatly affected by the presence of the pendulum strings. Except for one instance, string tension generally does not affect the observed trends in $e_{w,n}$ and θ_R for de-agglomerating collisions. However, for a given impact angle, the value of St_n that demarcates agglomeration versus de-agglomeration, $St^*(\theta_0)$, is largely influenced by string tension, since without string tension all oblique collisions are predicted to de-agglomerate; therefore, in this work the trends of $St^*(\theta_0)$ are not analyzed. (In Figure 5.7, with string tension, $St^*(\theta_0 = 0°) = 1.4$, $St^*(\theta_0 = 15°) = 1.3$, $St^*(\theta_0 = 30°) = 0.9$, $St^*(\theta_0 = 45°) = 0.4$, $St^*(\theta_0 = 65°) = 0.1$.)

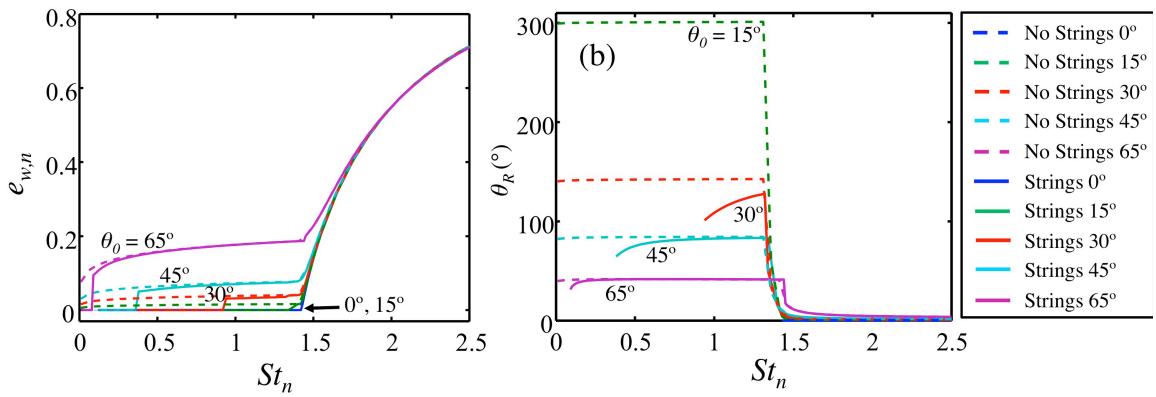

Figure 5.7 Theoretical predictions of (a) normal restitution coefficient and (b) angle rotated for case μ_{med}_$x_{0,\text{large}}$_cs_a_{large} at several impact angles with pendulum strings (solid curves) and without pendulum strings (dashed curves).

5.5.2. Effect of Experimental Parameters

In this section, the effect of the various input parameters are scrutinized by examining the trends in $e_{w,n}$ and θ_R as those parameters are varied. Additionally, a comparison of trends between experiment and theoretical predictions further serves to validate the theory. For purposes of conciseness, Table 5.2 at the end of this section serves to summarize the trends and provides an easy visual comparison.

To determine the role of the elasticity of the solid sphere in a wetted collision, the cases $\mu_{\text{med}}\_x_{0,\text{large}}\_\text{ss}\_a_{\text{large}}$ and $\mu_{\text{med}}\_x_{0,\text{large}}\_\text{cs}\_a_{\text{large}}$ are compared so that only particle material changes from the softer stainless steel (e_{dry} = 0.90) to the harder chrome steel (e_{dry} = 0.99). Figure 5.8a is a plot of experimental values of $e_{w,n}$ versus St_n for a range of impact angles. Open and closed symbols represent stainless steel and chrome steel, respectively. The value of St_n* (the critical St_n for de-agglomeration in head-on collisions) is not sensitive to e_{dry} and neither are the values of $e_{w,n}$ for $St_n < St_n$*. However, for $St_n > St_n$*, as e_{dry} is increased, the value of $e_{w,n}$ increases. Figure 5.8b shows the corresponding theoretical predictions and is plotted on the same scale for direct comparison. The theory agrees well with the experimental trends of $e_{w,n}$, though there are quantitative differences as noted earlier. The theory is especially useful here to provide insight into the cause of this trend. In particular, the value e_{dry} only affects the theoretical predictions if $St_n > St_n$* and bouncing occurs. Then, one of the three normal reversal criteria is met, and the relative velocity at that point is reversed and multiplied by e_{dry} to account for the dissipation of energy in the solid particle during deformation. However, when $St_n < St_n$*, and the particles reverse direction due to centrifugal forces, they do not deform and the value of e_{dry} is not used.

To see how e_{dry} affects the rotational motion of the doublet, the experimental θ_R is plotted versus St_n in Figure 5.8c, and no difference in θ_R is noted between the two values of e_{dry} examined. The corresponding theoretical predictions are plotted in Figure 5.8d, and this plot again has the same scale for direct comparison. Consistent with the experiments, the theory also indicates that e_{dry} does not significantly affect the rotation angle. Since the values of e_{dry} vary by only a small amount (< 10%), the collision

duration negligibly decreases as e_{dry} increases. Furthermore, the particle material does not affect the angular velocity (Equations 5.11 and 5.12). Since collision duration and angular velocity are unaffected by e_{dry}, θ_R also does not depend on e_{dry}. The theory is able to correctly predict the trends in $e_{w,n}$ and θ_R as e_{dry} increases, which is clearly seen in table 2; however, the theory does exhibit some quantitative mismatch.

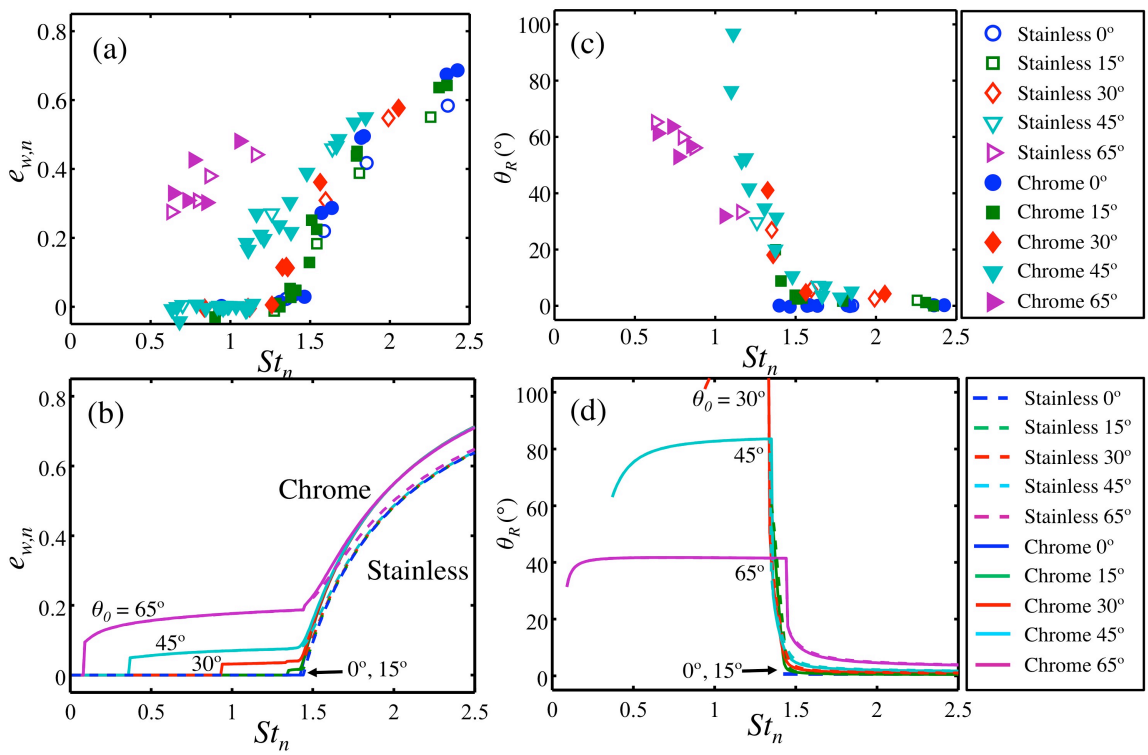

Figure 5.8 Normal restitution coefficient from (a) experiment and (b) theory, and rotation angle from (c) experiment and (d) theory as the dry restitution coefficient is increased from 0.90 (open symbols, dashed curves) to 0.99 (closed symbols, solid curves) for cases $\mu_{\text{med}}\_x_{0,\text{large}}\_\text{cs}\_a_{\text{large}}$ and $\mu_{\text{med}}\_x_{0,\text{large}}\_\text{ss}\_a_{\text{large}}$.

To investigate the effect of liquid viscosity, the cases $\mu_{\text{low}}\_x_{0,\text{med}}\_\text{ss}\_a_{\text{large}}$ and $\mu_{\text{med}}\_x_{0,\text{med}}\_\text{ss}\_a_{\text{large}}$, in which only the viscosity changes, are compared. Figures 5.9a and 5.9b are plots of $e_{w,n}$ versus St_n for the experiments and theoretical predictions, respectively. Both experiment and theoretical predictions show St_n* decreases as

viscosity increases (the particles more readily bounce at fixed St_n, which requires larger impact velocity for larger viscosity). For the low-viscosity-oil collisions, $St_n^* \sim 2.0$, whereas for medium-viscosity-oil collisions, $St_n^* \sim 1.0$ (Figure 5.9a). Therefore, to compare collisions that de-agglomerate due to centrifugal forces with different viscosities, only the region of St_n less than the medium-viscosity St_n^* is compared. Similarly, to compare the region where normal rebound criteria cause velocity reversal, only the region of St_n greater than the low-viscosity St_n^* is compared.

In Figures 5.9a and 5.9b, for $St_n > 2.0$ (low-viscosity $St_n^* = 2.0$), as viscosity increases, $e_{w,n}$ increases for a given value of St_n because higher lubrication pressures cause the glass transition to be reached with less penetration and a smaller fraction of the particle kinetic energy lost. Recall that the value of p_{gt} was chosen for each viscosity used in this work to agree with the experimental values of St_n^* for normal collisions only. Therefore, it is not surprising that in this region where particles reverse direction due to the glass-transition criterion, experimental trends agree with theoretical predictions. However, for $St_n < 1.0$ (medium-viscosity $St_n^* = 1.0$), where no glass transition criterion is met and therefore the value of p_{gt} is irrelevant, the same trend is not observed. Namely, the value of $e_{w,n}$ in this region is not sensitive to changes in viscosity. Again, the theory allows for further insight into the mechanics of the collision. Specifically, velocity reversal for $St_n < St_n^*$ is due only to centrifugal forces. As viscosity increases, the collision velocity must also increase in proportion at fixed St_n, so that the penetration depth when the relative normal motion is arrested is unchanged. Similarly, the fractional recovery of the normal velocity when the particles separate is unchanged, and so $e_{w,n}$ is left unaffected by changes in viscosity.

In Figures 5.9c and 5.9d, θ_R is plotted against St_n using the experimental data and theoretical predictions, respectively, again for cases with differing viscosities. For $St_n >$ 2.0 (low-viscosity $St_n^* = 2.0$), θ_R decreases as viscosity increases for a given St_n because the glass transition is reached more quickly. However, for $St_n < 1.0$ (high-viscosity $St_n^* =$ 1.0), no glass transition is predicted to occur and θ_R is essentially unaffected by changes in viscosity at fixed St_n. Again, higher viscosity requires higher impact velocity at fixed St_n. The resulting increase in rotational velocity is off set by a proportional decrease in collision duration due to the increased centrifugal force. The theory agrees well with the observed trends; however, a quantitative mismatch is shown for $St_n < St_n^*$.

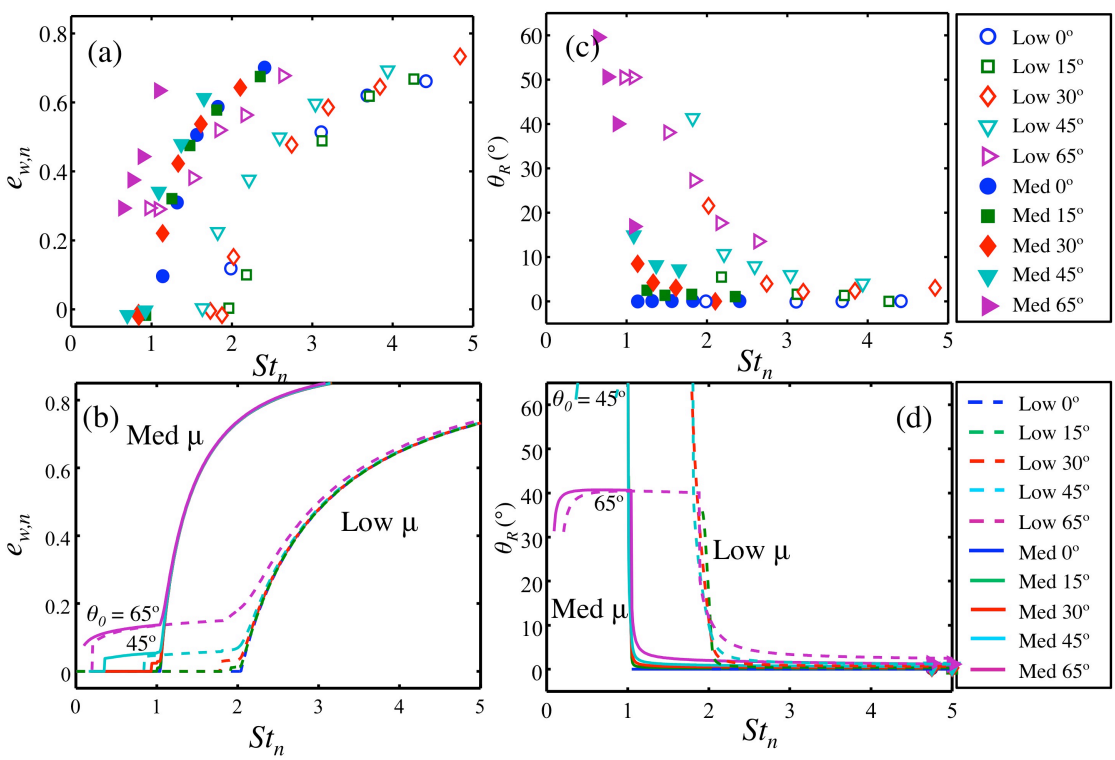

Figure 5.9 Normal restitution coefficient from (a) experiment and (b) theory, and rotation angle from (c) experiment and (d) theory as viscosity is increased from 5 Pa·s (open symbols, dashed curves) to 12 Pa·s (closed symbols, solid curves) for cases $\mu_{\text{low}}\_x_{0,\text{med}}\_\text{ss}\_a_{\text{large}}$ and $\mu_{\text{med}}\_x_{0,\text{med}}\_\text{ss}\_a_{\text{large}}$.

Figure 5.10 shows experimental data (Figure 5.10a) and corresponding theoretical predictions (Figure 5.10b) for $e_{w,n}$ for two cases with different thicknesses of the liquid coating, namely $\mu_{\text{med}}\_x_{0,\text{med}}\_\text{ss}\_a_{\text{large}}$ and $\mu_{\text{med}}\_x_{0,\text{large}}\_\text{ss}\_a_{\text{large}}$. For both the experiments and theory, St_n* increases as coating thickness increases. When $St_n < 1.0$ (thin-layer St_n* = 1.0), no obvious difference is observed in the experimental values of $e_{w,n}$ as coating thickness is changed, and likewise only very minor differences are observed in the theory. Since the initial separation distance of the particle surfaces is larger for the thick-coated particles, so that the lubrication resistance is less, the gap decreases by a greater amount during approach. However, the energy lost to viscous dissipation to bring relative normal motion to rest is independent of the fluid-layer thickness, and so the viscous losses as the particles subsequently separate due to centrifugal forces is also nearly independent of the layer thickness, so $e_{w,n}$ is nearly independent of x_0 when St_n is less than the thin-layer St_n*. Conversely, for $St_n > 1.4$ (thick-layer St_n* = 1.4), more viscous dissipation occurs for the larger coating thickness as the separation between the surfaces decreases to the critical gap value specified by the dominant reversal criterion, and then increases again after reversal, and so $e_{w,n}$ decreases with increasing x_0.

In Figures 5.10c and 5.10d, θ_R is plotted against St_n for experimental results and theoretical predictions, respectively. Only small changes in θ_R are observed in experiment and theoretical predictions for St_n less than the thin-layer St_n*, since the angular velocity is not sensitive to coating thickness (Equation 5.11), and the collision duration is approximately the same. In contrast, for St_n greater than the thick-layer St_n*, as coating thickness increases, the particles must penetrate a larger distance during

approach and reversal, so the collision duration increases, which results in an increase in θ_R in both experiment and theoretical predictions. The theory continues to predict the experimentally-observed trends, but again, a quantitative mismatch is shown for $St_n < St_n^*$.

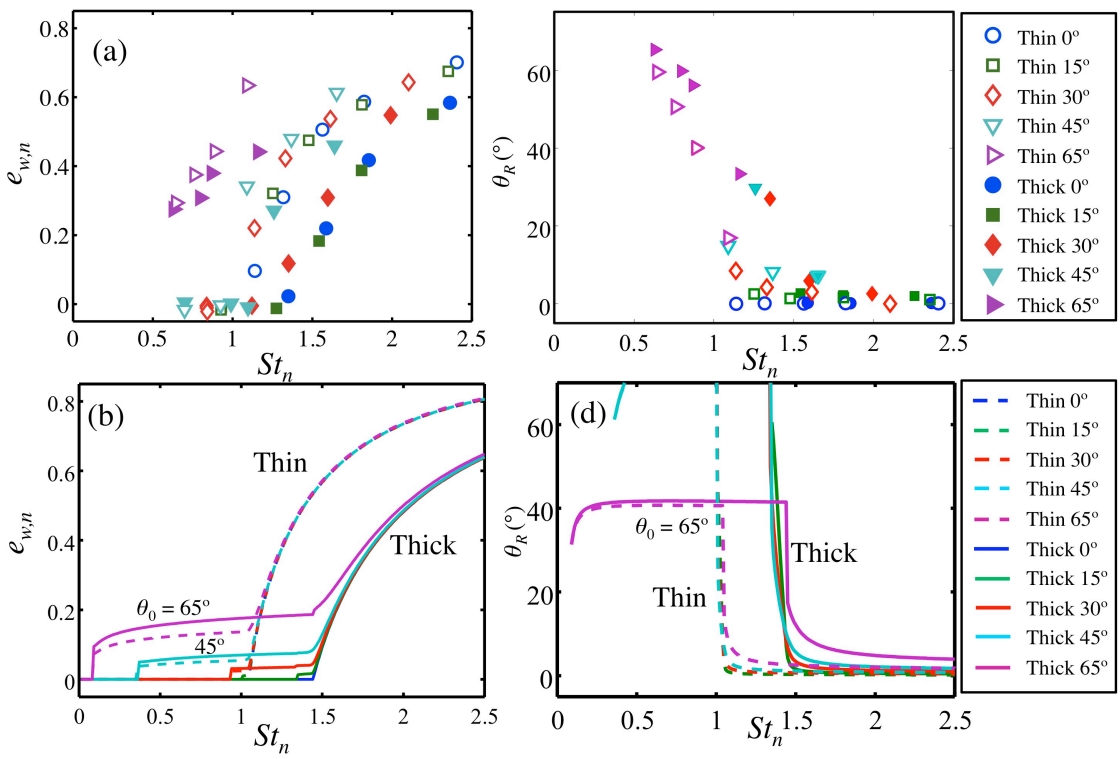

Figure 5.10 Normal restitution coefficient from (a) experiment and (b) theory, and rotation angle from (c) experiment and (d) theory as the coating thickness is increased from 270 μm (open symbols, dashed curves) to 420 μm (closed symbols, solid curves) for cases $\mu_{\text{med}}\_x_{0,\text{med}}\_\text{ss}\_a_{\text{large}}$ and $\mu_{\text{med}}\_x_{0,\text{large}}\_\text{ss}\_a_{\text{large}}$.

Finally, Figure 5.11 shows the effect of particle radius on $e_{w,n}$ and θ_R for the cases $\mu_{\text{med}}\_x_{0,\text{med}}\_\text{cs}\_a_{\text{small}}$ and $\mu_{\text{med}}\_x_{0,\text{med}}\_\text{cs}\_a_{\text{large}}$. Here, particle material density is held

constant so that particle mass also increases with radius. In Figures 5.11a and 5.11b, $e_{w,n}$ is plotted against St_n for the experimental results and theoretical predictions, respectively. The value of St_n* remains constant as particle radius increases for both experiment and theoretical predictions. Furthermore, over the entire range of St_n for de-agglomerating collisions ($St_n > 1.1$), the values of $e_{w,n}$ remain constant as particle radius increases for both experiment and theoretical predictions (within experimental error). Since Figure 5.11a and 5.11b are plotted in terms of St_n, which takes into account the changes in particle inertia and fluid resistance with changes in particle radius, the curves associated with the different radii collapse for $St_n > St_n$ *. For $St_n < St_n$ *, the theory predictions show a decrease in $e_{w,n}$ with an increase in radius. This change is due to the balance of lubrication and centrifugal forces in Equation 5.9, with v_n decreasing in proportion to $1/a^2$ (Equation 5.4).

In Figures 5.11c and 5.11d, θ_R is plotted against St_n for experimental results and theoretical predictions, respectively, for systems with different particle radii. Again, plotting θ_R versus St_n causes the curves associated with the different radii to nearly collapse for $St_n > St_n$*. However, for $St_n < St_n$*, a decrease in θ_R as particle radius increases is observed in both experiment and theoretical predictions. This decrease is due to string tension. As seen in Equation 5.7, string tension increases with particle radius, so that the larger particles are slowed down more and do not rotate as far.

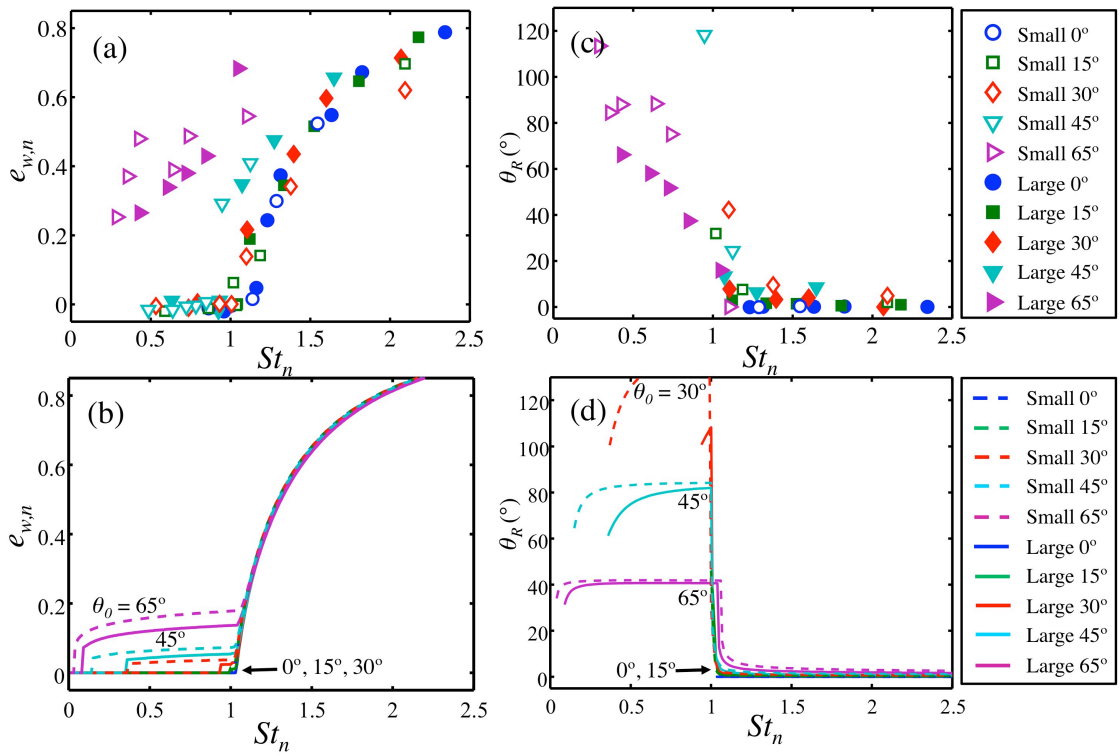

Figure 5.11 Normal restitution coefficient from (a) experiment and (b) theory, and rotation angle from (c) experiment and (d) theory as the radius is increased from 7.9 mm (open symbols, dashed curves) to 12.7 mm (closed symbols, solid curves) for casesμ_{med}_$x_{0,\text{med}}$_cs_a_{small} and μ_{med}_$x_{0,\text{med}}$_cs_a_{large}.

As previously mentioned, the trends are summarized in Table 5.2 for all of the parameters discussed. The theory consistently predicts the observed trends in $e_{w,n}$ and θ_R, which supports the physical interpretation of the experimental results presented in this work. For most parameters, different trends are observed for $St_n < St_n^*$ (stick-rotate-separate) versus $St_n > St_n^*$ (bounce), since different mechanism are responsible for de-agglomeration.

Table 5.2 Summary of trends of $e_{w,n}$ and θ_R at fixed St_n (↑ increase, ↓ decrease, ↔ no or small change)

	for $St_n < St_n^*$	for $St_n > St_n^*$	Figure
As e_{dry}↑, $e_{w,n}$	↔ (Experiment) ↔ (Theory)	↑ (Experiment) ↑ (Theory)	5.8
As e_{dry}↑, θ_R	↔ (Experiment) ↔ (Theory)	↔ (Experiment) ↔ (Theory)	5.8
As μ ↑, $e_{w,n}$	↔ (Experiment) ↔ (Theory)	↑ (Experiment) ↑ (Theory)	5.9
As μ ↑, θ_R	↔ (Experiment) ↔ (Theory)	↓ (Experiment) ↓ (Theory)	5.9
As x_0 ↑, $e_{w,n}$	↔ (Experiment) ↔ (Theory)	↓ (Experiment) ↓ (Theory)	5.10
As x_0 ↑, θ_R	↔ (Experiment) ↔ (Theory)	↑ (Experiment) ↑ (Theory)	5.10
As a ↑, $e_{w,n}$	↓ (Experiment) ↓ (Theory)	↔ (Experiment) ↔ (Theory)	5.11
As a ↑, θ_R	↓ (Experiment) ↓ (Theory)	↔ (Experiment) ↔ (Theory)	5.11

5.6. Conclusions

Unlike previous efforts on wetted collisions, which focused on normal particle-particle collisions and normal and oblique particle-wall collisions, the focus of this work is on oblique collisions between two particles. In this system, the wetted particles can agglomerate and rotate as a doublet, so that centrifugal forces play a role in the dynamics. To better understand the interplay between the underlying physical mechanisms, a theory is used with combination of experiments and lubrication (low Reynolds number) theory. In this work, the parameter space of the collisions is extended to include changes in viscosity, coating thickness, particle material, and particle radius. The theory

consistently predicts the experimentally observed trends in the wetted restitution coefficient ($e_{w,n}$) and the angle that the agglomerate rotates during the collision (θ_R) as parameters are changed. Surprisingly, the trends are different depending on whether de-agglomeration occurs for values of St_n less than St_n* or greater than St_n*, the value of the Stokes number at which normal (head-on) collisions transition from stick to bounce. Since the collision dynamics and de-agglomeration are primarily influenced by the particle deformation and reversal criteria associated with normal collisions when $St_n > St_n$*, the same trends are observed here as in previous normal particle-particle collisions [8]. However, centrifugal forces, which dominate the de-agglomeration process for $St_n < St_n$*, do not have the same dependence on the experimental parameters; accordingly, the values of $e_{w,n}$ and θ_R are not very sensitive to any of the parameters varied for both experiment and theory predictions (within experimental error). Therefore, the resulting trends for $e_{w,n}$ and θ_R are different when $St_n < St_n$* then when $St_n > St_n$* (as summarized in table 2). Furthermore, while the pendulum strings affect the St_n at which agglomeration occurs, they do not affect significantly the values of $e_{w,n}$ and θ_R for the outcomes stick-rotate-separate and bounce; thus, strings do not affect a majority of the trends found, except for one – the effect of particle radius on θ_R.

In this work, a micro-level (particle-level) approach has been taken to study the collisions between wetted particles. Such work is crucial to understanding macro-level behavior of many-particle systems, since collisions between particles in such systems are typically oblique. In descriptions of many-particle systems, normal collisions alone are not sufficient to describe the trends of bulk flow when input parameters are varied, since collisions that reverse direction due to centrifugal forces exhibit consistently different

trends. Furthermore, the work here together with previous work of oblique particle-wall collisions and normal collisions between more than two particles provides the foundation for discrete element method (DEM) simulations of many-particle systems [1, 4, 8]. Additionally, the surprising influence of centrifugal forces on de-agglomeration is expected to lead to the development of better population balance (continuum) models that more accurately take into account oblique collisions.

Literature Cited

1. Barnocky, G. and R.H. Davis. Elastohydrodynamic Collision and Rebound of Spheres - Experimental-Verification. *Physics of Fluids* **31**, 1324-1329, (1988).
2. Ennis, B.J., G. Tardos, and R. Pfeffer. A Microlevel-Based Characterization of Granulation Phenomena. *Powder Technology* **65**, 257-272, (1991).
3. Lian, G., M. Adams, and C. Thornton. Elastohydrodynamic collisions of solid spheres. *Journal of Fluid Mechanics* **311**, 141-152, (1996).
4. Kantak, A.A. and R.H. Davis. Oblique collisions and rebound of spheres from a wetted surface. *Journal of Fluid Mechanics* **509**, 63-81, (2004).
5. Darabi, P., K. Pougatch, M. Salcudean, and D. Grecov. A novel coalescence model for binary collision of identical wet particles. *Chemical Engineering Science* **64**, 1868-1876, (2009).
6. Davis, R.H., J.M. Serayssol, and E.J. Hinch. The Elastohydrodynamic Collision of 2 Spheres. *Journal of Fluid Mechanics* **163**, 479-497, (1986).
7. Davis, R.H., D.A. Rager, and B.T. Good. Elastohydrodynamic rebound of spheres from coated surfaces. *Journal of Fluid Mechanics* **468**, 107-119, (2002).
8. Donahue, C.M., C.M. Hrenya, R.H. Davis, K.J. Nakagawa, A.P. Zelinskaya, and G.G. Joseph. Stokes' cradle: normal three-body collisions between wetted particles. *Journal of Fluid Mechanics* **650**, 479-504, (2010).
9. Joseph, G.G., R. Zenit, M.L. Hunt, and A.M. Rosenwinkel. Particle-wall collisions in a viscous fluid. *Journal of Fluid Mechanics* **433**, 329-346, (2001).
10. Gondret, P., M. Lance, and L. Petit. Bouncing motion of spherical particles in fluids. *Physics of Fluids* **14**, 643, (2002).
11. Donahue, C.M., R.H. Davis, A.A. Kantak, and C.M. Hrenya. Identification of a new dimensionless number needed for prediction of de-agglomeration of rotating doublets *Submitted*, (2011).
12. Salcudean, M., P. Darabi, K. Pougatch, and D. Grecov. A novel coalescence model for binary collision of identical wet particles. *Chemical Engineering Science* **64**, 1868-1876, (2009).
13. O'Neill, M.E. and R. Majumdar. Asymmetrical slow viscous fluid motions caused by the translation or rotation of two spheres. Part I: The determination of exact

solutions for any values of the ratio of radii and separation parameters. *Zeitschrift für Angewandte Mathematik und Physik (ZAMP)* **21**, 164-179, (1970).

14. Davis, R.H. Elastohydrodynamic Collisions of Particles. *Physicochemical Hydrodynamics* **9**, 41-52, (1987).
15. Kantak, A.A. and R.H. Davis. Elastohydrodynamic theory for wet oblique collisions. *Powder Technology* **168**, 42-52, (2006).
16. Donahue, C.M., C.M. Hrenya, and R.H. Davis. Stokes's Cradle: Newton's Cradle with Liquid Coating. *Physical Review Letters* **105**, 34501, (2010).
17. Saitoh, K., A. Bodrova, H. Hayakawa, and N.V. Brilliantov. Negative Normal Restitution Coefficient Found in Simulation of Nanocluster Collisions. *Physical Review Letters* **105**, 238001, (2010).

6. INFLUENCE OF CENTRIFUGAL AND CAPILLARY FORCES IN OBLIQUE COLLISIONS OF TWO FREE-FALLING WETTED PARTICLES[7]

6.1. Abstract

Previous studies on wetted particle-particle collisions have been limited to head-on collisions, but in bulk flows collisions are inherently oblique. In this work, such oblique collisions are explored both experimentally and theoretically. Whereas in normal collisions particles rebound only due to solid deformation, so-called centrifugal forces in oblique collisions produce an outcome in which the particles initially form a rotating agglomerate, and then de-agglomerate at a later time. Surprisingly, capillary forces are essential in oblique collisions even when the capillary number (viscous over capillary forces) is high. This recognition leads to the introduction of a dimensionless number, the centrifugal number (centrifugal over capillary forces), which together with the previously established Stokes number characterizes the regime map of outcomes. Unexpectedly, a normal restitution coefficient greater than unity is observed at large impact angles, the mechanism for which may also be observed in other agglomerating systems.

---

[7] Donahue, C.M., R.H. Davis, A.A. Kantak, and C.M. Hrenya, *Mechanisms of Agglomeration and De-agglomeration following Oblique Collisions of Wet Particles.* Submitted, (2011).

6.2. Introduction

In the previous Chapter, the role of centrifugal forces in wetted two-body collisions was investigated. However, in those experiments, string tension from the pendulum played a significant role in the collision, particularly in the agglomeration behavior. In this Chapter, the string tension is removed from the theory and the predictions are analyzed.

The scope of this work is targeted at low-Reynolds number, *Re* (ratio of inertia to viscous forces of the liquid in the gap between particles) such that Stokes flow prevails. Previous low-*Re* work on wetted collisions found that the primary dimensionless parameter that dictates agglomeration versus de-agglomeration is the Stokes number, $St_n = mv_{n,0}/6\pi\mu a^2$, which is a ratio of the particle inertia to the viscous force. Here, $m = m_1 m_2/(m_1 + m_2)$ is the reduced mass of the particles, $v_{n,0}$ is the normal component of the relative impact velocity, μ is the liquid viscosity, and $a = R_1 R_2/(R_1 + R_2)$ is the reduced radius. Experiments showed that if St_n is below a critical value, St_n*, the two bodies agglomerate and if $St_n > St_n$*, they de-agglomerate regardless of whether it is a normal particle-particle or oblique particle-wall collision [1]. The value of St_n* is found theoretically via a coupling of hydrodynamics and solid mechanics (i.e., elastohydrodynamics) [2] or measured directly in experiments [3].

Pendulums have proven useful for experiments of normal and oblique particle collisions as they allow for small impact velocities [4-6] (as needed for Stokes flow with large particles, for example). In this work, the striker and target particles are held by pendulum strings spaced one diameter apart. A coating bath is used to coat the target particle, where the thickness of the liquid coating at a given drainage time is measured

using a high-resolution camera. The release position of the striker along the pendulum arc controls the impact velocity, and the string holding the target particle is attached to a rotating plate that controls the impact angle, θ_0, where $\theta_0 = 0^o$ for normal collisions and $\theta_0 = 90^o$ for perfectly tangential collisions. The pre- and post-collisional velocities are measured using a high-speed camera. Finally, data collection ceases if the doublets that are still agglomerated past 180°, since the two strings holding the particles cross, or if the angular velocity of the doublet reverses direction. As illustrated in Figure 6.1, three possible outcomes are observed. At small St_n, the particles stick (S, Figure 6.1a) due to viscous losses. At large St_n, the particles bounce (B, Figure 6.1c) due to elastic deformation. There are only two outcomes predicted and observed previously for normal collisions of two wet particles [7]. However, at intermediate St_n* for oblique collisions, the particles initially stick due to viscous losses, rotate for a substantial amount of time, and then separate due to centrifugal forces (SRS, Figure 6.1b). Note that the 'bounce' de-agglomeration mechanism is nearly instantaneous, whereas the 'stick-rotate-separate' mechanism is relatively slow.

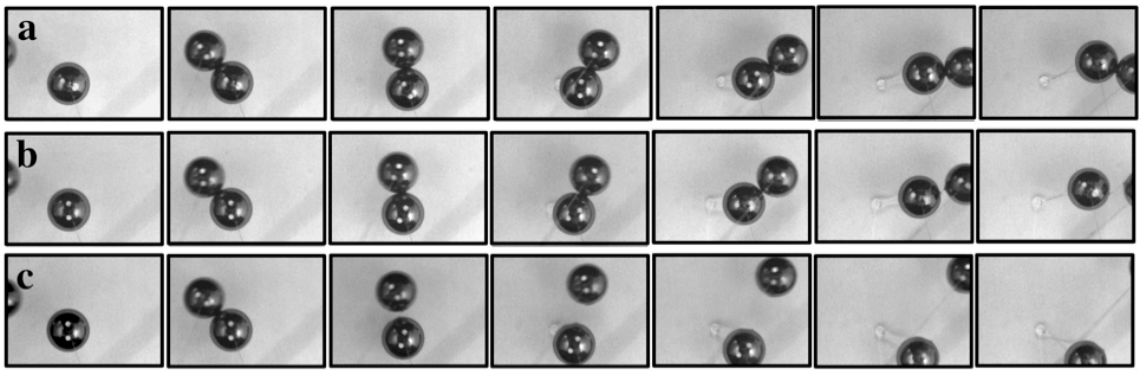

Figure 6.1 Top-view snapshots of collisions with outcomes of a**)** stick (S), b) stick-rotate-separate (SRS), and c) bounce (B) for parameters of 12 Pa·s oil, 420-μm oil thickness, chrome steel spheres of 25.4 mm diameter, and a 45°-impact angle. The only parameter that changes between the subfigures is impact velocity, such that the St_n for each subfigure is a**)** 1, b**)** 1.3, and c**)** 1.5. Corresponding videos can be found in the Supplementary Material. The time between each frame is a) 79 ms, b) 61 ms, and c) 49 ms.

6.3. Collisions with String Tension

For further physical insight into this mechanism for de-agglomeration, previous wetted-particle theories are extended to our system [3, 8, 9]. As mentioned previously, since Re is small ($Re = \rho v_{n,0} x_0 / \mu < 0.04$ in the experiments, where x_0 is the liquid-layer thickness), the viscous (dynamic) forces in the liquid bridge can be described by Stokes flow. Additionally, since the capillary number, (ratio of viscous to capillary forces, $Ca = 3\mu a v_{n,0} / \sigma x_0 >$ 1500, where σ is the surface tension), is large, capillary (static) forces are relatively small. Previous experiments with pendulums, including oblique collisions of dry particles and wet particle-wall collisions, have shown that the strings exert negligible tension on the particles [4-6]. However, the inclusion of string tension is critical to predicting the correct outcomes and trends, since the particles rotate through a

significant angle before de-agglomerating, allowing for large string tension forces to act over a long period of time.

Newton's equations of motion are solved (Table 6.1), including the centrifugal 'force', with an initial separation equal to the liquid-layer thickness, x_0. As the two particles approach each other, the pressure in the gap rapidly increases to squeeze out the liquid causing the solid particles to deform, which can lead to velocity reversal. If one of three reversal criteria is met, namely (i) the glass-transition pressure, p_{gt}, is exceeded, (ii) the separation distance of the particle surfaces, x, equals the elasticity length scale, x_r, based on previous elastohydrodynamic theory [3], or (iii) x equals the surface roughness, x_b, then the particles reverse direction. Specifically, the relative velocity is reversed and multiplied by the dry restitution coefficient, e_{dry}, to account for the energy dissipated by the solid particles upon deformation. Note that these criteria are identical to those present in normal collisions, and are independent of potential reversal caused by centrifugal forces (which are not present in normal collisions). The particles then separate (de-agglomerate) from each other when x reaches x_0. Due to the lack of well-established data, p_{gt} is estimated based on the measured value of St_n* [9].

TABLE 1. **Theory Description.**

	Lubrication	String Tension	Capillary
Relevant Forces	$F_{L,n} = -\frac{6\pi\mu a^2 v_n}{x}\left(1-\frac{x}{x_0}\right)^2$ 8 $F_{L,t} = -8\pi\mu a^2(\omega-\xi)\ln\frac{2a}{x_0}$ 9	$F_{S,n} = \frac{8mga}{l}\sin^2\left(\frac{\theta}{2}\right)\sqrt{1-\frac{16a^2}{l^2}\sin^2\left(\frac{\theta}{2}\right)}$ $F_{S,t} = -\frac{4mga}{l}\sin(\theta)\sqrt{1-\frac{16a^2}{l^2}\sin^2\left(\frac{\theta}{2}\right)}$	$F_c = 4\pi a\sigma\exp\left(\frac{Ax}{2a}+B\right)+C$ [10] $A = -1.1V^{-0.53}$ $B = (-0.34\ln V - 0.96)\phi^2 - 0.019\ln V + 0.48$ $C = 0.0042\ln V + 0.078$
Kinematic Equations	$m\frac{dv_n}{dt} = F_{L,n} + F_{S,n} + F_C + 4ma\omega^2$ $4ma\frac{d\omega}{dt} = F_{L,t} + F_{S,t} - 2mv_n\omega$ $\frac{8}{5}ma\frac{d\xi}{dt} = -F_{L,t}$		

Here, the subscripts n and t denote the normal and tangential directions, respectively, $v_n(t)$ is the relative normal velocity of the two spheres, $x(t)$ is the distance between their surfaces, $\omega(t)$ is the angular velocity of the doublet about its center of mass, $\xi(t)$ is the angular velocity of each particle about its center, $\beta(t)$ is the angle through which the doublet has rotated from initial contact, l is the length of the pendulum string, g is the gravitational acceleration, V is the liquid bridge volume non-dimensionalized by the particle radius cubed (assumed constant), and ϕ is the contact angle of the liquid with the solid sphere (assumed 0). Note that the tangential lubrication force in the normal direction is the classic formula of G.I. Taylor, corrected for the finite thickness of the thin film [8], whereas the tangential component is an approximation using the asymptotic analysis for nearly-touching, fully-immersed spheres [11], but modified by removing the constant term so that there is no hydrodynamic force on the doublet when in rigid-body motion ($\omega = \xi$).

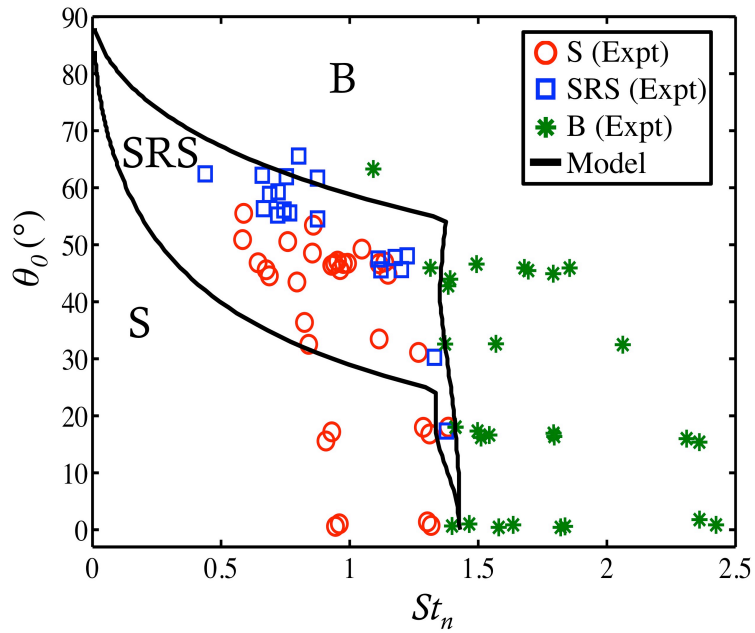

Figure 6.2 Regime map of collisional outcomes for pendulum apparatus. Symbols represent the outcome of a given experiment, and lines represent boundaries between the outcomes as predicted by the model for e_{dry} = 0.99, x_0 = 420 μm, x_b = 1 μm, a = 0.63 cm, μ = 12 Pa·s, m = 34 g, p_{gt} = 12 MPa. Pendulum strings are responsible for sticking collisions at oblique angles ($\theta_0 > 0$).

A regime map of the outcomes is shown in Figure 6.2. The model and experiments show all three outcomes and are in good agreement except that the S-SRS boundary occurs at higher θ_0 for a given St_n in the experiment. Furthermore, the model is able to well predict experimental trends in how the boundaries between outcomes change with a change in physical parameters (e_{dry}, x_0, a, μ), the details of which are not included here for brevity. In Figure 6.2, the value of St_n at which normal collisions (θ_0 = 0º) transition from stick to bounce, namely St_n*, is equal to 1.4. For oblique collisions, the value of St_n* also serves to demarcate the transition between agglomeration and de-agglomeration for small impact angles (θ_0~< 50º). At large impact angles (θ_0~> 50º), however, St_n* serves as a boundary between stick-rotate-separate and bounce. This

inability of St_n* to be used as a predictor of agglomeration versus de-agglomeration for more oblique collisions can be traced to the role of centrifugal forces, which are responsible for the ultimate de-agglomeration for the stick-rotate-separate outcome.

6.4. Collisions with Capillary Forces

In practical applications in both nature and industry, clearly pendulum strings are not connected to particles. Thus, to more realistically model these systems, model without string tension (but with capillary forces) is developed. If two particles in a rotating doublet are to stick together, their relative velocity, and, hence, lubrication suction force, must eventually go to zero. Since the centrifugal force continues to pull the particles in a rotating doublet apart, another (cohesive) force is needed to balance it, if the particles are to remain agglomerated. When particles stick in a free collision, the additional force is provided by capillary forces. Recall that in this work, *Ca* is large, implying that capillary forces may be neglected [12]. Therefore, and somewhat surprisingly, even when *Ca* is large, capillary forces are non-negligible for *oblique* collisions and thus included (but not in the model for experiments since agglomeration due to strings was found to overshadow capillary forces).

Figure 6.3 is a regime map of possible outcomes produced by solving Newton's equations for the oblique collision of two wetted particles without pendulum strings but with the capillary force included, for input parameters consistent with values representative of the granulation process and common to other industrial applications. De-agglomeration occurs when the liquid bridge ruptures at $x_f = 2aV^{1/3}$ [13]. It is important to point out here that while the shape of the boundary between stick and stick-

rotate-separate appears to be similar in Figure 6.2 and 6.3a, the mechanisms for sticking (agglomeration) are surprisingly different. In both cases, if $St_n < St_n^*$, the particles initially agglomerate due to viscous forces and rotate as a doublet with conservation of angular momentum. The corresponding centrifugal force tends to pull the doublet apart. In Figure 6.2, with pendulum strings, the centrifugal force is opposed to by a lubrication suction force (to draw fluid into the gap as the particles separate) and string tension; agglomeration is assumed if the particles are still together when $\theta_0 = 180^\circ$ and the strings cross or if the angular velocity reverses direction due to string tension. In Figure 6.3a, for particles without pendulum strings, the centrifugal force is opposed by lubrication suction and the capillary force; without the capillary force, de-agglomeration would always occur once the doublet rotates far enough. On the other hand, unlike oblique collisions, normal collisions are practically unaffected by the presence of capillary forces. Normal collisions still agglomerate for $St_n < St_n^*$ even when capillary forces are removed (as indicated by the arrow pointing to $\theta_0 = 0$ in the inset of Figure 6.3a), which is consistent with previous models [3, 8, 9].

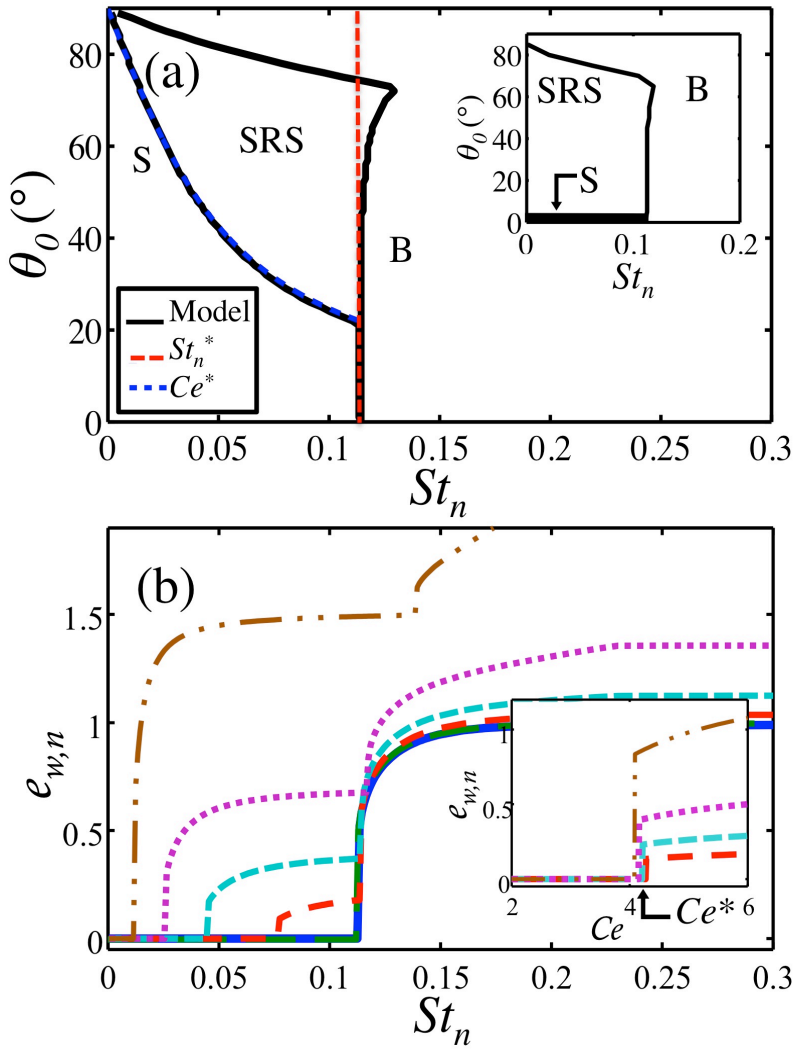

Figure 6.3 Model predictions for free collisions (no strings attached): (a) outcome regime map and (b) normal restitution coefficient for collisions with e_{dry} = 0.99, x_0 = 8 μm, x_b = 0.2 μm, a = 50 μm, μ = 2 Pa·s, m = 5.2×10^{-6} g, σ = 0.025 N/m, p_{gt} = 20 MPa, V = 0.1, and θ_0 = 0º, 15º, 30º, 45º, 60º, and 75º (bottom to top). The dimensionless numbers Ce^* = 4.2 and St_n^* = 0.11 serve as boundaries to the stick outcome. The inset of (a) shows the model without capillary forces, so that only normal collisions agglomerate.

6.5. Centrifugal Number

The identification of the relative role of centrifugal and capillary forces in the agglomeration behavior of oblique collisions leads to a new dimensionless number that,

together with the Stokes number, is key to predicting agglomeration versus de-agglomeration. Since the transition between stick and stick-rotate-separate occurs when centrifugal forces dominate over capillary forces, a relevant dimensionless number is proposed, namely the centrifugal number,

$$Ce = \frac{m\omega_0^2}{\sigma}, \tag{6.1}$$

where ω_0 is the initial angular velocity. In Figure 6.3a, a critical value of Ce, namely Ce^* = 4.2, and a critical value of St_n (St_n^* = 0.11) are plotted on top of the model predictions, and the two lines enclose the stick region (agglomeration) superbly. (Note that when the first kinematic equation is non-dimensionalized by $a\sigma$, the centrifugal number falls out from the centrifugal force term.)

To investigate the dynamics of the collisions in more detail, the predicted wet normal restitution coefficient, $e_{w,n}$ is plotted against St_n in Figure 6.3b. In this work, $e_{w,n} = -\vec{v}_f \cdot \vec{n}_f / (\vec{v}_0 \cdot \vec{n}_0)$, where the subscripts *0* and *f* denote pre- and post-collisional values, respectively [14]. Note that, unlike the traditional definition, this definition distinguishes between the initial and final direction of $\vec{n}$, the unit vector that points from the center of one particle to the other. The curve of $e_{w,n}$ for θ_0 = 15° collisions is almost indistinguishable from normal collisions (θ_0 = 0) and only stick ($e_{w,n}$ = 0) and bounce are observed. At higher impact angles, the curves also exhibit a region of stick-rotate-separate outcomes (moderate St_n), for which the curves are qualitatively different than in the bounce outcome (higher St_n^*), and a discontinuity in the slope at St_n^* = 0.11 separates the two outcomes. The relevance of Ce is further illustrated by the inset of Figure 6.3b,

which is a plot of $e_{w,n}$ versus Ce for the subset of collisions at impact angles large enough so that only centrifugal forces facilitate rebound (no normal reversal criterion is met). The exact value of Ce^* depends very little on impact angle. Moreover, doubling the values of V, x_0, μ,σ, m and a leads to a change in Ce^* by a factor of 1.0, 0.79, 0.99, 1.01, 1.01 and 1.13, respectively. Therefore, large changes in input parameters result in relatively small changes in Ce^*. This lack of sensitivity of Ce^* has important implications in practical flows where, for example, there may not be a uniform distribution of liquid. Therefore, a mid-range value of Ce^* should still be able to predict agglomeration well in this regime ($St_n < St_n^*$).

A remarkable aspect of Figure 6.3b is that $e_{w,n} > 1$ in some regions, indicating that the normal component of the post-collisional relative velocity is greater than its pre-collisional value. The normal coefficient of restitution typically ranges between zero and one, with perfectly inelastic collisions giving zero and perfectly elastic collisions giving unity. One exception is oblique, dry collisions of a hard particle impacting a soft wall where a normal restitution coefficient greater than unity has been observed for collisions past a critical impact angle, which is related to the local deformation of the wall [14, 15]. However, there is no indication that the same mechanisms would be present in (dry) particle-particle collisions. In the case of wetted particles, the initial separation of the particles is x_0, but the final rupture distance x_f is larger due to stretching of the liquid bridge. The moment of inertia of the doublet, $I = ma^2\left(\left(\frac{x}{a}+4\right)^2+\frac{32}{5}\right)$, increases as x increases, and since angular momentum ($I\omega$) is conserved, the angular velocity decreases. Therefore, since the total kinetic energy is $\frac{1}{2}I\omega^2+\frac{1}{2}mv_n^2$, v_n must increase as the rotational

kinetic energy decreases if viscous dissipation is ignored. So, when the increase in the normal velocity due to this hysteresis in the initial and final separation distance is greater than the amount lost due to viscous dissipation, the magnitude of final normal velocity will be larger than the initial value, which leads to $e_{w,n} > 1$. This effect could also be observed in other systems of agglomerates that exhibit hysteresis in the initial and final separation distance, such as in nanoclusters where the object shape may deform.

6.6. Conclusions

In conclusion, an experimentally validated model has been used to study agglomeration/de-agglomeration behavior for oblique collisions of two wet spheres. In addition to the stick and bounce outcomes observed for head-on collisions, an outcome has been observed for oblique collisions in which particles initially agglomerate, and then later de-agglomerate due solely to centrifugal forces. Furthermore, even at high Ca, capillary forces are surprisingly essential for the doublet to remain agglomerated in oblique collisions. The relative importance of the centrifugal and capillary forces is characterized by a new dimensionless number, the centrifugal number, Ce. For the case of oblique collisions, Ce and the previously established St_n are essential for characterizing agglomeration versus de-agglomeration, where as previously only the role of St_n had been identified in normal collisions. In practical, many-particle systems, oblique collisions are the norm, so this introduction of Ce is key to an accurate prediction of agglomeration versus de-agglomeration. Similar dimensionless numbers may also be useful in other agglomerating systems by replacing the capillary force in the denominator of Ce by a measure of the relevant cohesive force (for instance, in agglomeration of very small particles, the van der Waals force). Not only do the dimensionless numbers Ce and St_n

aid in our physical understanding, but the associated computational costs of modeling bulk flow by solving the equations for each individual particle via discrete element model (DEM) simulations can be reduced, since the full equations need not be solved depending on the dominant physics present in a given collision. Additionally, a normal coefficient of restitution greater than unity has been observed, where the normal relative velocity increases at the expense of angular kinetic energy. This mechanism is not limited to wetted collisions, but is possible in any collision in which the initial separation distance is smaller than the final separation distance, such as in the collision of viscoelastic drops. The micro-level understanding of the physical mechanisms of wetted-particle collisions, as investigated here, is essential for a macro-level understanding of bulk flow of diverse systems from pharmaceuticals here on earth to interstellar grains in an asteroid belt.

Literature Cited

1. Kantak, A.A. and R.H. Davis. Oblique collisions and rebound of spheres from a wetted surface. *Journal of Fluid Mechanics* **509**, 63-81, (2004).
2. Ennis, B.J., J.L. Li, G.I. Tardos, and R. Pfeffer. The Influence of Viscosity on the Strength of an Axially Strained Pendular Liquid Bridge. *Chemical Engineering Science* **45**, 3071-3088, (1990).
3. Davis, R.H., D.A. Rager, and B.T. Good. Elastohydrodynamic rebound of spheres from coated surfaces. *Journal of Fluid Mechanics* **468**, 107-119, (2002).
4. Sorace, C.M., M.Y. Louge, M.D. Crozier, and V.H.C. Law. High apparent adhesion energy in the breakdown of normal restitution for binary impacts of small spheres at low speed. *Mechanics Research Communications* **36**, 364-368, (2009).
5. Donahue, C.M., C.M. Hrenya, and R.H. Davis. Stokes's Cradle: Newton's Cradle with Liquid Coating. *Physical Review Letters* **105**, 34501, (2010).
6. Yang, F.L. and M.L. Hunt. Dynamics of particle-particle collisions in a viscous liquid. *Physics of Fluids* **18**, 121506, (2006).
7. Davis, R.H. Elastohydrodynamic Collisions of Particles. *Physicochemical Hydrodynamics* **9**, 41-52, (1987).
8. Kantak, A.A. and R.H. Davis. Elastohydrodynamic theory for wet oblique collisions. *Powder Technology* **168**, 42-52, (2006).

9. Donahue, C.M., C.M. Hrenya, R.H. Davis, K.J. Nakagawa, A.P. Zelinskaya, and G.G. Joseph. Stokes' cradle: normal three-body collisions between wetted particles. *Journal of Fluid Mechanics* **650**, 479-504, (2010).
10. Mikami, T., H. Kamiya, and M. Horio. Numerical simulation of cohesive powder behavior in a fluidized bed. *Chemical Engineering Science* **53**, 1927-1940, (1998).
11. O'Neill, M.E. and R. Majumdar. Asymmetrical slow viscous fluid motions caused by the translation or rotation of two spheres. Part I: The determination of exact solutions for any values of the ratio of radii and separation parameters. *Zeitschrift für Angewandte Mathematik und Physik (ZAMP)* **21**, 164-179, (1970).
12. Salcudean, M., P. Darabi, K. Pougatch, and D. Grecov. A novel coalescence model for binary collision of identical wet particles. *Chemical Engineering Science* **64**, 1868-1876, (2009).
13. Lian, G.P., C. Thornton, and M.J. Adams. A Theoretical-Study of the Liquid Bridge Forces between 2 Rigid Spherical Bodies. *Journal of colloid and interface science* **161**, 138-147, (1993).
14. Saitoh, K., A. Bodrova, H. Hayakawa, and N.V. Brilliantov. Negative Normal Restitution Coefficient Found in Simulation of Nanocluster Collisions. *Physical Review Letters* **105**, 238001, (2010).
15. Louge, M.Y. and M.E. Adams. Anomalous behavior of normal kinematic restitution in the oblique impacts of a hard sphere on an elastoplastic plate. *Physical Review E* **65**, 21303, (2002).

7. CONCLUSIONS AND FUTURE WORK

7.1. Conclusions

The focus of this work has been to extend the previous wetted-particle experiments and theory to (i) collisions between more than two particles and (ii) oblique collisions between two particles. In a normal or head-on, two-body collision, only two possible geometrical outcomes exist, stick or bounce. Conversely, in a three-particle collision four geometrically possible outcomes exist (under both wet or dry conditions).

Before investigating normal (head-on) three-particle wet collisions, experiments of the dry counterpart were performed and compared to existing soft-sphere and hard-sphere models. To model a three-body collision using a hard-sphere model, the collision was approximated as a series of two-body collisions. In dry collisions, the only outcome observed was that of all particles fully separated. Furthermore, the striker particle was observed to reverse direction with a relatively small velocity after impact. While the hard-sphere model is unable to predict this velocity reversal (unlike the soft-sphere models), it predicts the correct outcome of separate spheres. Additionally, the hard-sphere model predicts well the velocity of the target particle opposite the striker, which receives a majority of the momentum. While this work has shown that most soft-sphere models outperform the hard-sphere model, the shortcomings of the hard-sphere model do

not appear insurmountable, and it still remains an attractive choice in simulations given its relatively low computational costs.

Next, the same experimental apparatus was used to investigate wetted three-particle collisions by coating the target particles with silicon oil. Because the liquid layer is characterized by low-Reynolds number (Stokes) flow, the apparatus is coined 'Stokes's cradle'. The initial set of experiments over a wide range of parameters revealed every outcome except for the one outcome associated with the Newton's cradle in which the particle opposite the target is ejected from the group, and the rest are left motionless. A comparison of the theory to the experimental results identified two key pieces of physics ignored in previous works: 1) as the pressure in the liquid gap between the particles increases, the liquid may reach the glass transition, at which point the particles reverse direction; 2) while the pressure in the liquid gap is predicted to drop below the vapor pressure of the liquid, implying cavitation may have occurred, outbound resistance cannot be neglected. With aid from the theory developed in this work, eventually the Newton's cradle outcome was experimentally attained by changing the amount of liquid in the bridge connecting the two target particles.

Finally, to investigate how rotation of an agglomerate affects de-agglomeration, oblique particle-particle collisions were explored experimentally and theoretically. In normal (head-on) collisions between two particles, de-agglomeration only occurs when energy stored in the deformation of the solid particle during approach is released, causing the particles to reverse direction. Furthermore, normal collisions were observed to either stick or bounce. On the other hand, in oblique collisions, centrifugal forces cause the particles to reverse their relative motion from forward to away from one another, which

leads to a new outcome, namely stick-rotate-separate, in which the particles initially form a rotating agglomerate and then de-agglomerate at a later time. Furthermore, even when the capillary number (viscous over capillary forces) is large compared to unity, capillary forces are essential for agglomeration of particles in oblique collisions; otherwise, all oblique collisions would eventually de-agglomerate due to centrifugal forces. This recognition lead to the introduction of a dimensionless number, the centrifugal number (centrifugal over capillary forces), which together with the previously established Stokes number, characterizes the regime map of possible outcomes.

The work here has added to the understanding of wetted-particle collisions, particularly since a number of physical mechanisms have been identified and the effect of different parameters has been established. Specifically, the mechanisms identified include the glass transition of the coating liquid, viscous resistance during particle separation, centrifugal forces, and capillary forces. When modeling wetted particles, future works will need to account for these physical mechanisms. For example, previous work on normal collisions has shown that the capillary forces can be neglected when the capillary number is large. Conversely, this work has shown capillary forces are important in oblique collisions even when the capillary number is large. Since collisions are more often than not oblique, in most practical systems capillary forces need to be considered. Additionally, to characterize wetted flow, the properties of the liquid coating and the solid particle are needed. Current measurements that are routinely taken include liquid viscosity, surface tension, and dry restitution coefficient. By identifying the relevant physical mechanisms, this work drives what measurements are important. Particularly, the glass-transition pressure is not typically measured for the liquids

involved in wetted flows, but is an important parameter that determines agglomeration versus de-agglomeration.

In previous works, trends in the critical Stokes number and restitution coefficient for normal two-body collisions have been well established. Furthermore, when the critical Stokes number decreases, the probability of normal collisions to de-agglomerate increases, causing collisions to be 'bouncier'. However, those same trends may not be directly applied to many-particle systems that include both oblique collisions and collisions involving more than two particles. For example, changing parameters that make normal two-particle collisions bouncier does not always make normal three-particle collisions bouncier (i.e. a larger number of particles separated). Normal two-particle collisions are always bouncier as the liquid layer thickness is decreased. However, this work has shown that, for particular parameters, decreasing the amount of liquid results in 'stickier' three-particle collisions. Additionally, the trends of oblique collisions that de-agglomerate due to centrifugal forces are different than the trends of normal collisions. For instance, a few ways to increase the wet coefficient of restitution in normal collisions for a given Stokes number are to decrease the coating thickness, increase the viscosity, or increase the dry restitution coefficient of the solid. However, for an oblique collision that de-agglomerates with a Stokes number less than the critical Stokes number, changing any of these parameters will not change the value of the wet restitution coefficient.

7.2. Recommendations for Future Work

7.2.1. Microscopic

The primary focus in this work was to identify the relevant physical mechanisms in normal three-body collisions and oblique two-body collisions. Further work should be focused on refinement of the important physics. Such physical mechanisms include the glass transition, cavitation, and the deformation of the liquid bridge. The high-speed camera used in this work was primarily employed to measure pre- and post-collisional velocities and, due to the low frame rate, was unable to capture the dynamics during a normal collision. However, since all three mechanisms above influence the post-collisional velocity, isolating the effect of each physical mechanism is difficult. A high-speed camera with greater spatial and temporal resolution could be used to determine accelerations of each particle during the collision process and, therefore, the forces experienced by each particle. In turn, the experimental force profiles could be compared against theoretical predictions during different stages of the collision. For instance, in a normal collision, as the particles approach each other, the particles experience resistance from the viscous liquid. As the pressure in the gap increases, the viscosity increases and so does the viscous resistance. The effect of such pressure-dependent viscosity can be compared to the theoretical force profiles as the particles are approaching one another, since cavitation is not assumed to be relevant at this point. Furthermore, the influence of temperature due to viscous heating of the liquid as the particles are approaching was not investigated in this work. An approximate calculation can be made by assuming that a majority of the energy lost during the collision is contributed to viscous heating such that the change in temperature is

$$\Delta T = \frac{\frac{1}{4} m_p v_0^2 (e_w^2 - 1)}{m_l c_p} \tag{7.1}$$

where m_p is the mass of the particle, v_0 is the impact velocity, e_w is the wet restitution coefficient, m_l is the mass of the liquid heated, and c_p is the specific heat of the oil. The volume of the liquid heated during the collision is assumed to be equal to $x_0 \times \pi(2ax_0)$ where x_0 is the initial thickness, $\sqrt{2ax_0}$ is the characteristic radial distance over which the lubrication force is distributed, and a is the reduced radius of the particle. Subsequently, the change in temperature is quite modest and is no more than 2 K for the parameters used in this work. Additionally, the current work indicates that presumed cavitation conditions (predicted pressure lower than vapor pressure) do not preclude the outbound resistance, but the influence of such cavitation is still uncertain. Therefore, to assess the effect of cavitation, experimental force profiles as the particles are moving away from each other could be compared to theoretical predictions. Finally, in the current model, viscous resistance was assumed negligible when the particles reached a separation distance equal to either the initial liquid thickness or an effective thickness based on the volume of the liquid bridge connecting the particles. However, during the collision, the liquid no longer evenly coats the particles but deforms as the bridge elongates and, therefore, the separation distance at which lubrication goes to zero should be refined. One way to determine how deformation of the bridge influences lubrication is to determine the distance at which the forces go to zero as the particles are separating.

While the dimensionless centrifugal number was identified in Chapter 6, no experiments were carried out to verify its ability to demarcate the transition between

agglomeration and de-agglomeration of wetted oblique collisions. Previous experimental works have verified the prediction that the Stokes number must be above a critical Stokes number for de-agglomeration of normal collisions to occur. Accordingly, the Stokes number has become a significant number in both research papers and textbooks. The centrifugal number is expected to play a similarly important role in oblique collisions, since the centrifugal number is a measure of the centrifugal forces to the capillary forces, which are relevant in oblique collisions but not in normal collisions under conditions investigated. For the experiments on oblique collisions performed as part of this work, recall that de-agglomeration was prevented by the presence of pendulum strings rather than capillary forces, the latter which would dominate in unconstrained (no pendulum) collisions. As a result, the ability of the centrifugal number to predict agglomeration/de-agglomeration behavior for two particles was not tested in this work. A recommendation for future work is to experimentally validate the critical centrifugal number. Since the particles could no longer be held by pendulum strings, experiments would need to be performed in a free-falling manner, such as a reduced-gravity aircraft or drop tower. While free-falling collisions of two particles have been performed in table-top experiments [1], such collisions have been between dry particles in which the collision time is considerably shorter, therefore requiring a shorter drop distance. In wetted collisions, preliminary results of the model of Chapter 5 and 6 indicated for similar materials used in this work, the collision times could be as large as 5 seconds. Therefore, the minimum drop distance for such collisions would be 125 m.

7.2.2. Macroscopic

Many tools are available to study the macroscopic flow of particles. Discrete element models (DEM) of individual particles offer a direct way to implement the microscopic theory developed in this work to study bulk flow. Previous work of two-body collisions alone did not provide an adequate foundation for DEM simulations since neither collisions of more than two particles nor the rotational motion of an agglomerate had been studied. The work here on normal three-body collisions indicates that approximating a collision involving more than two particles via a series of two-body collisions and using a hard-sphere model may be adequate for purposes of DEM simulations. Such a treatment will significantly reduce the computational power required, since a wet coefficient of restitution can be calculated *a priori* and the full differential equations do not need to be solved for each collision. On the other hand, a series of two-body collisions requires that the collision time is short enough so that only the particle velocities significantly change during the collision and not the particle positions. In normal collisions, such as in the collisions in Chapter 3 and 4, this is the case, but in oblique collisions the collision time is long. During this long collision time, the colliding particles may change positions considerably. For example, if one particle strikes two agglomerated particles at an oblique angle, the striker and the first target particle will rotate around the center of mass of those two particles. Therefore, since it is assumed that the target particle opposite the striker is not engaged in the collision, its distance from the other target particle will increase as that target particle rotates away. The lure of low computational costs is such that creative approximations to this problem should be pursued.

Since computational power limits the number of particles that can be simulated in DEM, continuum theory is also important in describing the macroscopic flow of industrial systems. Such a continuum framework for describing wetted-particle agglomeration and de-agglomeration exists via in the population balance, which is a rate equation that tracks the change in the number of particles of a given property. However, many of the current agglomeration models used in population balances have been largely empirical. As a result, they are not useful for predicting effects of scale-up, design changes, or changes in properties. A small number of models are semi-empirical or physically based and depend on the critical Stokes number [2]. However, current models only account for the normal component of velocity and not impact angle. In future works, to account for a range of impact angles, population balance models should be based on the centrifugal number as well as the Stokes number.

7.2.3. Applications

In addition to identifying and refining the physical understanding of wetted-particle collisions, making the findings of this work more accessible and useful for practical situations (granulation, agglomeration, etc.) is important. In previous works, the critical Stokes number was identified as the key parameter for predicting agglomeration versus de-agglomeration. In this work, the centrifugal number has also been identified as a crucial parameter in predicting agglomeration versus de-agglomeration. Both values can be found theoretically but require good models and detailed measurements of specific parameters. For instance, the glass-transition pressure is necessary to determine the critical Stokes number. However, even for the silicon oils used in this work and

elsewhere well-established measurements do not yet exist. Therefore, methods should be developed to empirically determine the critical Stokes number and the critical centrifugal number.

To measure the critical Stokes number, a particle could be dropped onto a wetted wall (or a fixed particle). The height at which the particles transition from stick to rebound can then be used to find the impact velocity and thus the critical Stokes number. Detailed measurements of post-collisional velocities are not necessary since only the impact velocity factors into the Stokes number. To measure the critical centrifugal number, a particle can be stuck onto a wetted wall that is oriented vertically as long as the capillary force is larger than gravity. Rotating the wall introduces a centrifugal force to the particle. The angular velocity at which the particle leaves the surface, along with the mass of the particle and surface tension of the liquid, can be used to determine the critical centrifugal number. Such devices are already in use [3].

Literature Cited

1. Foerster, S.F., M.Y. Louge, A.H. Chang, and K. Allia. Measurements of the Collision Properties of Small Spheres. *Physics of Fluids* **6**, 1108-1115, (1994).
2. X. Liu, L. and J. D. Litster. Population balance modelling of granulation with a physically based coalescence kernel. *Chemical Engineering Science* **57**, 2183-2191, (2002).
3. Mizes, H., M. Ott, E. Eklund, and D. Hays. Small particle adhesion: measurement and control. *Colloids and Surfaces A: Physicochemical and Engineering Aspects* **165**, 11-23, (2000).

Bibliography

Adams, M., B. Briscoe, and L. Pope. Tribology in Particulate Technology. *Adam Hilger*, (1987).

Adams, M. and V. Perchard. The Cohesive Forces Between Particles with Interstitial Liquid. *Proceedings of Powder Technology*, 147, (1985).

Allen, C., D. Townsend, and E. Zaretsky. Elastohydrodynamic lubrication of a spinning ball in a nonconforming groove. *J. Lubr. Tech* **92**, 89-96, (1970).

Alsaad, M., S. Bair, D. Sanborn, and W. Winer. *Glass transitions in lubricants- Its relation to elastohydrodynamic lubrication/EHD*. 1977.

Angel, R.J., M. Bujak, J. Zhao, G.D. Gatta, and S.D. Jacobsen. Effective hydrostatic limits of pressure media for high-pressure crystallographic studies. *Journal of Applied Crystallography* **40**, 26-32, (2007).

Bair, S. *Unpublished*, (2008).

Barnocky, G. and R.H. Davis. Elastohydrodynamic Collision and Rebound of Spheres - Experimental-Verification. *Physics of Fluids* **31**, 1324-1329, (1988).

Barnocky, G. and R.H. Davis. The Influence of Pressure-Dependent Density and Viscosity on the Elastohydrodynamic Collision and Rebound of 2 Spheres. *Journal of Fluid Mechanics* **209**, 501-519, (1989).

Bonneau, O., C. Vernet, M. Moranville, and P.C. Aitcin. Characterization of the granular packing and percolation threshold of reactive powder concrete. *Cement and concrete research* **30**, 1861-1867, (2000).

Bridges, F.G., A. Hatzes, and D. Lin. Structure, stability and evolution of Saturn's rings. (1984).

Bridgwater, J. Mixing of particles and powders: Where next? *Particuology*, (2010).

Brilliantov, N.V., F. Spahn, J.M. Hertzsch, and T. Poschel. Model for collisions in granular gases. *Physical Review E* **53**, 5382, (1996).

Bull, T. The tensile strengths of viscous liquids under dynamic loading. *British Journal of Applied Physics* **7**, 416, (1956).

Cameron, A., *Basic lubrication theory*. 1981, Ellis Horwood, Chichester.

Ceanga, V. and Y. Hurmuzlu. A new look at an old problem: Newton's cradle. *Journal of Applied Mechanics* **68**, 575, (2001).

Chang, H.-C. and L.-H. Chen. Growth of a gas bubble in a viscous fluid. *Physics of Fluids* **29**, 3530-3536, (1986).

Chu, P. and A. Cameron. Pressure viscosity characteristics of lubricating oils. *J. Inst. Petrol* **48**, 147, (1962).

Cross, N.L. and R.G. Picknett. Comment on Paper Effect of Capillary Liquid on Force of Adhesion between Spherical Solid Particles. *Journal of colloid and interface science* **26**, 247-&, (1968).

Cundall, P.A. and O. Strack. A discrete numerical model for granular assemblies. *Geotechnique* **29**, 47-65, (1979).

Darabi, P., K. Pougatch, M. Salcudean, and D. Grecov. A novel coalescence model for binary collision of identical wet particles. *Chemical Engineering Science* **64**, 1868-1876, (2009).

Davis, R.H. Elastohydrodynamic Collisions of Particles. *Physicochemical Hydrodynamics* **9**, 41-52, (1987).

Davis, R.H., D.A. Rager, and B.T. Good. Elastohydrodynamic rebound of spheres from coated surfaces. *Journal of Fluid Mechanics* **468**, 107-119, (2002).

Davis, R.H., J.M. Serayssol, and E.J. Hinch. The Elastohydrodynamic Collision of 2 Spheres. *Journal of Fluid Mechanics* **163**, 479-497, (1986).

Dippel, S. and D. Wolf. Force schemes in simulations of granular materials. *Journal de physique I* **6**, 5-20, (1996).

Donahue, C.M., R.H. Davis, A.A. Kantak, and C.M. Hrenya. Identification of a new dimensionless number needed for prediction of de-agglomeration of rotating doublets *Submitted*, (2011).

Donahue, C.M., C.M. Hrenya, and R.H. Davis. Stokes's Cradle: Newton's Cradle with Liquid Coating. *Physical Review Letters* **105**, 34501, (2010).

Donahue, C.M., C.M. Hrenya, R.H. Davis, K.J. Nakagawa, A.P. Zelinskaya, and G.G. Joseph. Stokes' cradle: normal three-body collisions between wetted particles. *Journal of Fluid Mechanics* **650**, 479-504, (2010).

Donahue, C.M., C.M. Hrenya, A.P. Zelinskaya, and K.J. Nakagawa. Newton's cradle undone: Experiments and collision models for the normal collision of three solid spheres. *Physics of Fluids* **20**, 110330, (2008).

Dong, K., R. Yang, R. Zou, and A. Yu. Role of interparticle forces in the formation of random loose packing. *Physical Review Letters* **96**, 145505, (2006).

Ennis, B.J., J.L. Li, G.I. Tardos, and R. Pfeffer. The Influence of Viscosity on the Strength of an Axially Strained Pendular Liquid Bridge. *Chemical Engineering Science* **45**, 3071-3088, (1990).

Ennis, B.J., G. Tardos, and R. Pfeffer. A Microlevel-Based Characterization of Granulation Phenomena. *Powder Technology* **65**, 257-272, (1991).

Fairbrother, R.J. and S.J.R. Simons. Modelling of Binder Induced Agglomeration. *Particle & Particle Systems Characterization* **15**, 16-20, (1998).

Faure, A., P. York, and R. Rowe. Process control and scale-up of pharmaceutical wet granulation processes: a review. *European Journal of Pharmaceutics and Biopharmaceutics* **52**, 269-277, (2001).

Fisher, R.A. On the capillary forces in an ideal soil; Correction of formulae given by W. B. Haines. *Journal of Agricultural Science* **16**, 492-505, (1926).

Fleming, R.W., F.A. Taylor, and G. Survey, *Estimating the costs of landslide damage in the United States*. 1980, US Dept. of the Interior, Geological Survey.

Foerster, S.F., M.Y. Louge, A.H. Chang, and K. Allia. Measurements of the Collision Properties of Small Spheres. *Physics of Fluids* **6**, 1108-1115, (1994).

Forsyth, A., S. Hutton, C. Osborne, and M. Rhodes. Effects of interparticle force on the packing of spherical granular material. *Physical Review Letters* **87**, 244301, (2001).

Forsyth, A., S. Hutton, M. Rhodes, and C. Osborne. Effect of applied interparticle force on the static and dynamic angles of repose of spherical granular material. *Physical Review E* **63**, 31302, (2001).

Gamsky, J.N. and P.T. Metzger. *The Physical State of Lunar Soil in the Permanently Shadowed Craters of the Moon*. 2010: ASCE.

Gohar, R. Elastohydrodynamics. (World Scientific Publishing Company, 2001).

Goldhirsch, I. Rapid granular flows. *Annual review of fluid mechanics* **35**, 267-293, (2003).

Goldsmith, W. Impact. (Arnold, 1960).

Goldsmith, W. Impact: the theory and physical behaviour of colliding solids. (Dover Pubns, 2001).

Gondret, P., M. Lance, and L. Petit. Bouncing motion of spherical particles in fluids. *Physics of Fluids* **14**, 643, (2002).

Gorham, D. and A. Kharaz. The measurement of particle rebound characteristics. *Powder Technology* **112**, 193-202, (2000).

Hertz, H. Ueber die Ber¸hrung fester elastischer Kˆrper. *Journal f¸r die reine und angewandte Mathematik (Crelle's Journal)* **1882**, 156-171, (1882).

Hertzsch, J.M., F. Spahn, and N.V. Brilliantov. On low-velocity collisions of viscoelastic particles. *Journal de Physique II* **5**, 1725-1738, (1995).

Hinch, E. and S. SaintñJean. The fragmentation of a line of balls by an impact. *Proceedings of the Royal Society of London. Series A: Mathematical, Physical and Engineering Sciences* **455**, 3201, (1999).

Hrenya, C.M. and A.B. Stevens. Comparison of soft-sphere models to measurements of collision properties during normal impacts. *Powder Technology* **154**, 99-109, (2005).

Hulbert, H. and S. Katz. Chem. *Engng Sci* **19**, 555, (1964).

Hutton, S., A. Forsyth, M. Rhodes, and C. Osborne. Effect of interparticle force on mixing and segregation of dry granular materials. *Physical Review E* **70**, 31301, (2004).

Iveson, S.M. Limitations of one-dimensional population balance models of wet granulation processes. *Powder Technology* **124**, 219-229, (2002).

Jain, K., D.L. Shi, and J.J. McCarthy. Discrete characterization of cohesion in gas-solid flows. *Powder Technology* **146**, 160-167, (2004).

Johnson, K. Contact mechanics *eq.(7) and*, 294, (1985).

Joseph, D.D. Cavitation and the state of stress in a flowing liquid. *Journal of Fluid Mechanics* **366**, 367-378, (1998).

Joseph, G.G., R. Zenit, M.L. Hunt, and A.M. Rosenwinkel. Particle-wall collisions in a viscous fluid. *Journal of Fluid Mechanics* **433**, 329-346, (2001).

Kantak, A.A. and R.H. Davis. Oblique collisions and rebound of spheres from a wetted surface. *Journal of Fluid Mechanics* **509**, 63-81, (2004).

Kantak, A.A. and R.H. Davis. Elastohydrodynamic theory for wet oblique collisions. *Powder Technology* **168**, 42-52, (2006).

Kantak, A.A., C.M. Hrenya, and R.H. Davis. Initial rates of aggregation for dilute, granular flows of wet particles. *Physics of Fluids* **21**, 23301, (2009).

Ketterhagen, W.R., J.S. Curtis, and C.R. Wassgren. Stress results from two-dimensional granular shear flow simulations using various collision models. *Physical Review E* **71**, 61307, (2005).

Khan, M.I. and G.I. Tardos. Stability of wet agglomerates in granular shear flows. *Journal of Fluid Mechanics* **347**, 347-368, (1997).

King, H., R. White, I. Maxwell, and N. Menon. Inelastic impact of a sphere on a massive plane: Nonmonotonic velocity-dependence of the restitution coefficient. *EPL (Europhysics Letters)* **93**, 14002, (2011).

Knapp, R., J. Daily, and F. Hammitt, *Cavitation, 1970*, McGraw-Hill, New York.

Kruggel-Emden, H., E. Simsek, S. Rickelt, S. Wirtz, and V. Scherer. Review and extension of normal force models for the discrete element method. *Powder Technology* **171**, 157-173, (2007).

Kruggel-Emden, H., S. Wirtz, and V. Scherer. A study on tangential force laws applicable to the discrete element method (DEM) for materials with viscoelastic or plastic behavior. *Chemical Engineering Science* **63**, 1523-1541, (2008).

Kuwabara, G. and K. Kono. Restitution coefficient in a collision between two spheres. *Japanese journal of applied physics* **26**, 1230-1233, (1987).

Labous, L., A.D. Rosato, and R.N. Dave. Measurements of collisional properties of spheres using high-speed video analysis. *Physical Review E* **56**, 5717-5725, (1997).

Law, C.L. and A.S. Mujumdar. Drying: Biological Materials. *Encyclopedia of Industrial Biotechnology: Bioprocess, Bioseparation, and Cell Technology*.

Leboreiro Hernandez, J., *Influence of drag laws on segregation and bubbling behavior in gas-fluidized beds*. 2008, University of Colorado at Boulder.

Lee, J. and H.J. Herrmann. Angle of repose and angle of marginal stability: molecular dynamics of granular particles. *Journal of Physics A: Mathematical and General* **26**, 373, (1993).

Li, H.M. and J.J. McCarthy. Phase diagrams for cohesive particle mixing and segregation. *Physical Review E* **71**, 21305, (2005).

Li, H.M. and J.J. McCarthy. Cohesive particle mixing and segregation under shear. *Powder Technology* **164**, 58-64, (2006).

Lian, G., M. Adams, and C. Thornton. Elastohydrodynamic collisions of solid spheres. *Journal of Fluid Mechanics* **311**, 141-152, (1996).

Lian, G., M.J. Adams, and C. Thornton. Elastohydrodynamic collisions of solid spheres. *Journal of Fluid Mechanics* **311**, 141-152, (1996).

Lian, G., C. Thornton, and M. Adams. Discrete particle simulation of agglomerate impact coalescence. *Chemical Engineering Science* **53**, 3381-3391, (1998).

Lian, G.P., C. Thornton, and M.J. Adams. A Theoretical-Study of the Liquid Bridge Forces between 2 Rigid Spherical Bodies. *Journal of colloid and interface science* **161**, 138-147, (1993).

Litster, J. and B. Ennis. The science and engineering of granulation processes. Vol. 15 (Kluwer Academic Pub, 2004).

Liu, P.Y., R.Y. Yang, and A.B. Yu. Dynamics of wet particles in rotating drums: Effect of liquid surface tension. *Physics of Fluids* **23**, 13304-9, (2011).

Louge, M.Y. and M.E. Adams. Anomalous behavior of normal kinematic restitution in the oblique impacts of a hard sphere on an elastoplastic plate. *Physical Review E* **65**, 21303, (2002).

Luding, S., E. ClÈment, A. Blumen, J. Rajchenbach, and J. Duran. Anomalous energy dissipation in molecular-dynamics simulations of grains: The``detachment"effect. *Physical Review E* **50**, 4113-4122, (1994).

Lundberg, J. and H.H. Shen. Collisional Restitution Dependence on Viscosity. *Journal of Engineering Mechanics-Asce* **118**, 979-989, (1992).

Marston, J., W. Yong, W. Ng, R.B.H. Tan, and S. Thoroddsen. Cavitation structures formed during the rebound of a sphere from a wetted surface. *Experiments in Fluids*, 1-18, (2010).

Mason, G. and W.C. Clark. Liquid Bridges between Spheres. *Chemical Engineering Science* **20**, 859, (1965).

Matsen, J.M. Scale-up of fluidized bed processes: Principle and practice. *Powder Technology* **88**, 237-244, (1996).

McCarthy, J.J. Micro-modeling of cohesive mixing processes. *Powder Technology* **138**, 63-67, (2003).

Mikami, T., H. Kamiya, and M. Horio. Numerical simulation of cohesive powder behavior in a fluidized bed. *Chemical Engineering Science* **53**, 1927-1940, (1998).

Mills, P., J. Seville, P. Knight, and M. Adams. The effect of binder viscosity on particle agglomeration in a low shear mixer/agglomerator. *Powder Technology* **113**, 140-147, (2000).

Mishra, B. and C. Thornton. An improved contact model for ball mill simulation by the discrete element method. *Advanced Powder Technology* **13**, 25-41, (2002).

Mizes, H., M. Ott, E. Eklund, and D. Hays. Small particle adhesion: measurement and control. *Colloids and Surfaces A: Physicochemical and Engineering Aspects* **165**, 11-23, (2000).

Muzzio, F.J., T. Shinbrot, and B.J. Glasser. Powder technology in the pharmaceutical industry: the need to catch up fast. *Powder Technology* **124**, 1-7, (2002).

Nedderman, R.M. Statics and kinematics of granular materials. (Cambridge Univ Pr, 1992).

Nowak, S., A. Samadani, and A. Kudrolli. Maximum angle of stability of a wet granular pile. *Nature Physics* **1**, 50-52, (2005).

O'Neill, M.E. and R. Majumdar. Asymmetrical slow viscous fluid motions caused by the translation or rotation of two spheres. Part I: The determination of exact solutions for any values of the ratio of radii and separation parameters. *Zeitschrift für Angewandte Mathematik und Physik (ZAMP)* **21**, 164-179, (1970).

Ottino, J. and D. Khakhar. Mixing and segregation of granular materials. *Annual review of fluid mechanics* **32**, 55-91, (2000).

Pepin, X., D. Rossetti, S.M. Iveson, and S.J.R. Simons. Modeling the evolution and rupture of pendular liquid bridges in the presence of large wetting hysteresis. *Journal of colloid and interface science* **232**, 289-297, (2000).

Pierrat, P. and H.S. Caram. Tensile strength of wet granula materials. *Powder Technology* **91**, 83-93, (1997).

Pitois, O., P. Moucheront, and X. Chateau. Liquid bridge between two moving spheres: An experimental study of viscosity effects. *Journal of colloid and interface science* **231**, 26-31, (2000).

Pont, S., P. Gondret, B. Perrin, and M. Rabaud. Wall effects on granular heap stability. *EPL (Europhysics Letters)* **61**, 492, (2003).

Prescott, J.K. Powder Handling. *Pharmaceutical Process Scale-Up* **118**, 133, (2001).

Princen, H.M. Comments on Effect of Capillary Liquid on Force of Adhesion between Spherical Solid Particles. *Journal of colloid and interface science* **26**, 249-&, (1968).

Rajniak, P., F. Stepanek, K. Dhanasekharan, R. Fan, C. Mancinelli, and R. Chern. A combined experimental and computational study of wet granulation in a Wurster fluid bed granulator. *Powder Technology* **189**, 190-201, (2009).

Randolph, A.D. and M.A. Larson. Theory of particulate processes. (Academic Press New York, 1971).

Roelands, C.J.A. Correlational aspects of the viscosity-temperature-pressure relationship of lubricating oils. *Druk. VRB, Groningen, Netherland s*, (1966).

Sadd, M.H., Q. Tai, and A. Shukla. Contact law effects on wave propagation in particulate materials using distinct element modeling. *International journal of non-linear mechanics* **28**, 251-265, (1993).

Saitoh, K., A. Bodrova, H. Hayakawa, and N.V. Brilliantov. Negative Normal Restitution Coefficient Found in Simulation of Nanocluster Collisions. *Physical Review Letters* **105**, 238001, (2010).

Salcudean, M., P. Darabi, K. Pougatch, and D. Grecov. A novel coalescence model for binary collision of identical wet particles. *Chemical Engineering Science* **64**, 1868-1876, (2009).

Saleh, K., D. Steinmetz, and M. Hemati. Experimental study and modeling of fluidized bed coating and agglomeration. *Powder Technology* **130**, 116-123, (2003).

Samadani, A. and A. Kudrolli. Segregation transitions in wet granular matter. *Physical Review Letters* **85**, 5102-5105, (2000).

Sheng, Y., C. Lawrence, B. Briscoe, and C. Thornton. Numerical studies of uniaxial powder compaction process by 3D DEM. *Engineering Computations* **21**, 304-317, (2004).

Shi, D. and J.J. McCarthy. Numerical simulation of liquid transfer between particles. *Powder Technology* **184**, 64-75, (2008).

Sorace, C.M., M.Y. Louge, M.D. Crozier, and V.H.C. Law. High apparent adhesion energy in the breakdown of normal restitution for binary impacts of small spheres at low speed. *Mechanics Research Communications* **36**, 364-368, (2009).

Stokes, G. On the theory of internal friction of fluids in motion, etc. *Cambridge Trans* **8**, 287-305, (1845).

Talu, I., G.I. Tardos, and M.I. Khan. Computer simulation of wet granulation. *Powder Technology* **110**, 59-75, (2000).

Tegzes, P., T. Vicsek, and P. Schiffer. Development of correlations in the dynamics of wet granular avalanches. *Physical Review E* **67**, 51303, (2003).

Thornton, C. Coefficient of restitution for collinear collisions of elastic-perfectly plastic spheres. *Journal of Applied Mechanics* **64**, 383, (1997).

Thornton, C. and Z. Ning. A theoretical model for the stick/bounce behaviour of adhesive, elastic-plastic spheres. *Powder Technology* **99**, 154-162, (1998).

Tomas, J. Fundamentals of cohesive powder consolidation and flow. *Granular Matter* **6**, 75-86, (2004).

Tsuji, Y., T. Tanaka, and T. Ishida. Lagrangian numerical simulation of plug flow of cohesionless particles in a horizontal pipe. *Powder Technology* **71**, 239-250, (1992).

Valverde, J.M., A. Ramos, A. Castellanos, and P. Keith Watson. The tensile strength of cohesive powders and its relationship to consolidation, free volume and cohesivity. *Powder Technology* **97**, 237-245, (1998).

Vu-Quoc, L. and X. Zhang. An elastoplastic contact forceñdisplacement model in the normal direction: displacementñdriven version. *Proceedings of the Royal Society of London. Series A: Mathematical, Physical and Engineering Sciences* **455**, 4013, (1999).

Walton, O.R. and R.L. Braun. Viscosity, granular-temperature, and stress calculations for shearing assemblies of inelastic, frictional disks. *Journal of Rheology* **30**, 949-980, (1986).

Weber, M.W., D.K. Hoffman, and C.M. Hrenya. Discrete-particle simulations of cohesive granular flow using a square-well potential. *Granular Matter* **6**, 239-254, (2004).

Weber, M.W. and C.M. Hrenya. Square-well model for cohesion in fluidized beds. *Chemical Engineering Science* **61**, 4511-4527, (2006).

Weber, M.W. and C.M. Hrenya. Computational study of pressure-drop hysteresis in fluidized beds. *Powder Technology* **177**, 170-184, (2007).

Willett, C.D., M.J. Adams, S.A. Johnson, and J.P.K. Seville. Capillary bridges between two spherical bodies. *Langmuir* **16**, 9396-9405, (2000).

Wills, B., *Mineral Processing Technology* 1979, Pergamon Press, lnc: New York City.

Wu, C., L. Li, and C. Thornton. Rebound behaviour of spheres for plastic impacts. *International journal of impact engineering* **28**, 929-946, (2003).

X. Liu, L. and J. D. Litster. Population balance modelling of granulation with a physically based coalescence kernel. *Chemical Engineering Science* **57**, 2183-2191, (2002).

Xu, Q., A.V. Orpe, and A. Kudrolli. Lubrication effects on the flow of wet granular materials. *Physical Review E* **76**, 31302, (2007).

Yang, F.L. and M.L. Hunt. Dynamics of particle-particle collisions in a viscous liquid. *Physics of Fluids* **18**, 121506, (2006).

Zhang, R. and J. Li. Simulation on mechanical behavior of cohesive soil by Distinct Element Method. *Journal of terramechanics* **43**, 303-316, (2006).